TECHNISCHE UNIVERSITÄT
MÜNCHEN

Critical Magnetic Fluctuations in Localized and Itinerant Magnets Studied by Neutron Scattering

Dipl. Phys. Univ. Daniel Lamago Kaffo

Vollständiger Abdruck der von der Fakultät für Physik der Technischen Universität München zur Erlangung des akademischen Grades eines **Doktor der Naturwissenschaften (Dr. rer. nat.)**

genehmigten Dissertation.

Vorsitzender:	Univ.-Prof. Dr. Manfred Kleber
Prüfer der Dissertation:	1. Univ.-Prof. Dr. Peter Böni 2. Univ.-Prof. Dr. Winfried Petry

Die Dissertation wurde am 04.04.2006 an der Technischen Universität München eingereicht und durch die Fakultät für Physik am 25.04.2006 angenommen.

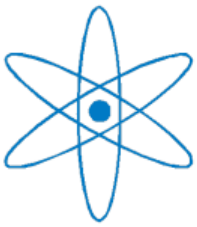

Dedicated to

Laurick Moriel, Shirel Hodiya and Hélène.

Abstract

Critical magnetic fluctuations in localized and itinerant magnets have been studied by means of bulk methods and small angle scattering of polarized neutrons. The effect of three and four-spin correlations corresponding to the dynamical and spontaneous chirality, respectively, on the critical behavior is discussed.

Results of spin fluctuations in the critical temperature range of the Heisenberg ferromagnet EuS are presented. We used the inclined magnetic field geometry in SANS experiment to induce the chirality in EuS and thus determine the three-spin correlation function. Two contributions to the critical scattering were studied close to $T_C = 16.5\,\mathrm{K}$. The polarization dependent symmetric contribution originates from the pair correlation function and asymmetric contribution that is caused by the three-spin correlation function and depends on the polarization. We proved that the critical spin fluctuations are strongly affected by the magnetic field as the temperature goes to T_C. The correlation length ξ is suppressed according to the scaling law $\xi = a_0(gB\mu_B/T_C)^{1/z}$. We determined the dynamical critical exponent $z = 2.1 \pm 0.1$. Due to the effect of dipolar interactions the value of z deviates from the value predicted by the theory $z = 2.5$. However our results are in good agreement with those obtained in previous studies by means of triple axis spectroscopy. Therefore the inclined geometry in SANS is an efficient and an alternative method to the conventional triple-axis spectrometer for the determination of critical exponents.

The chiral fluctuations in the itinerant weak magnet MnSi were studied by AC, DC magnetization, specific heat and by magnetic small angle neutron scattering. Due the lack of a centre of symmetry the magnetic moments are arranged along a left-handed spiral as a result of the Dzyaloshinskii-Moriya interaction. We demonstrated that the incommensurate magnetic peaks evolve with increasing temperature into diffuse scattering that is mainly concentrated in rings around the nuclear Bragg peaks. The ring of the critical scattering was found to be anisotropic so that the critical spin fluctuations obey the scaling hypothesis in the easy magnetization direction namely the $\langle \pm 1, \pm 1, \pm 1 \rangle$. The scattering is fully polarized for $\vec{q} \parallel \vec{P}_0$ and depolarized for $\vec{q} \perp \vec{P}_0$ proving the chiral nature of the spin fluctuations and the single handedness of the magnetic spiral. We have determined the critical exponents $\beta_c = 0.44(1)$ and $\nu_c = 0.64(3)$ that are in agreement with values predicted for a chiral universality class.

In the presence of a magnetic field we studied the wave-vector and spin reorientation phase transitions at low temperatures. We studied the magnetic behavior of MnSi in the so-called A-phase, that is located close to T_c in low fields region. The specific heat data shows a tiny anomaly at the border of the A-phase characteristic of a well defined phase transition. We observed a ring of scattering intensity in the A-phase. These results indicate that magnetic structure in the A-phase cannot be interpreted in terms of an abrupt change of orientation of a simple helical modulation.

Contents

Chapter 1

Motivation and Goal of this Investigation

In all things of nature there is something of the marvelous.
Aristotle

Magnetic materials can be classified into localized and itinerant electron models. The localized spin model is one of the models for understanding the magnetism of matter. In this model, electrons which carry the magnetic moment localize at atomic positions and the magnetic structure is determined by the interactions between the localized magnetic moments. This is established to be the case in magnetic insulator like EuS and in the majority of rare-earth metals. The Heisenberg type inter-atomic interaction JS_iS_j is used in this model also known as the Heisenberg model.
If the electrons that carry the magnetic moment are free to move in the crystal as it is the case in transition metals, the magnetic properties are thought to be determined by the band structure whithin the Stoner theory. This model is called the itinerant electron or band model. In the case of itinerant weak ferromagnetism, the Stoner model does not explain the fact that the susceptibility follows the Curie-Weiss theory above the Curie temperature. The theory of Moriya et al. [1] explains satisfactorily the spin fluctuations in itinerant weak ferromagnetic materials (MnSi, $ZrZn_2$, Ni_3Al, Sc_3In are typical examples) at finite temperatures including the temperature dependence of the susceptibility.
With our enhanced understanding of the fundamental theory of magnetism these materials now form what is probably the most important testing ground of the theory of phase transitions that is considered as one of the challenges of modern physics.
The physical properties of a magnetic material are related to the time and spatial spin correlation function $G(r,t)$, which is the Fourier transform of the dynamical susceptibility $\chi(q,\omega)$, where q and ω represent the wave vector and energy of the magnetic fluctuations, respectively. For the characterization of magnetically ordered compounds three physical parameters are necessary namely the ordering temperature, the magnetic moment and the spin correlation length.
Traditionally the pair correlation function is used to described the critical behavior. However in magnetic materials three and four spin correlations are present due to the spin chirality.
In extremely simple terms, chirality means “handedness”, that is the existence of left/right

opposition. The human hand is just one of the many examples of chirality in nature. Chirality has been recognized to play an important role not only in living systems (organic molecules, proteins) but also in magnetism.

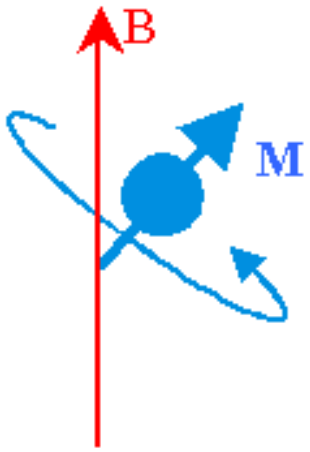

Figure 1.1: Electron in the presence of a magnetic field. Its spin starts to rotate in a certain direction.

An electron in a magnetic field $\vec{B}$ will start to rotate in a certain direction as illustrated in Fig. 1.1.
The quantum mechanical amplitude obtains a complex factor with its phase determined by the vector potential $\vec{A}$ corresponding to $\vec{B} = \nabla \times \vec{A}$. In magnetic materials, the analogous complex factor may occur when an electron moves along non coplanar spin configurations and the effective magnetic field is represented by the spin chirality, namely the solid angle subtended by the spins. Chirality in magnetic material arises spontaneously from spin interactions or is induced by an external magnetic field. Recently Braun et al. reported on the emergence of quantum soliton chirality in the Ising quantum antiferromagnet $CsCoBr_3$ [2]. They first applied a magnetic field to remove degeneracy of the chiral states and used polarized neutrons to distinguish different chirality.

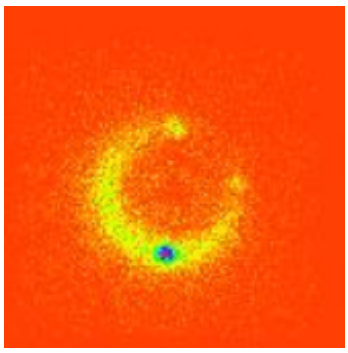

Figure 1.2: Spontaneous spin chirality has been observed in MnSi. The helicity is found to be left-handed. The scattering pattern is obtained above the critical temperature on a SANS diffractometer.

In this thesis we investigate the spin fluctuations close to the critical temperature in localized and itinerant magnets. In order to study the effect of chirality on the critical behavior we choose a typical Heisenberg magnet EuS where we induced the chirality by applying an external magnetic field. Another magnetic material we use is the itinerant electron system MnSi with an intrinsic chirality as depicted in Fig. 1.2.

The thesis is organized as follows: Chapter 2 is intended to give a short review of the basic concepts of critical phenomena and magnetic phase transitions. Chapter 3 deals with a general presentation of the experimental techniques used for these investigations. Particular emphasis is given to the method of "inclined geometry" used to study the induced chirality. In Chapter 4 we present the critical spin fluctuations in the localized magnet EuS. We discuss the effect of two- and three-spin correlation (induced chirality) on the critical behavior of the system. The results are compared with previous studies on triple axis spectroscopy. Chapter 5 describes the critical fluctuations due to the four-spin correlation (spontaneous chirality) in the itinerant weak ferromagnet MnSi. Chapter 6 presents results of the effect of magnetic field on the spiral structure at low temperatures and in the vicinity of the critical temperature. Conclusions and outlooks are given in Chapter 7.
The meaning of the symbols and abbreviations which are often used in the text is described in the Appendix A.

Chapter 2

Magnetic Phase Transitions and Critical Fluctuations

Not only is the universe stranger than we imagine, it is stranger than we can imagine
Sir Arthur Eddington

2.1 Introduction

Phase transitions play an essential role in everyday life. In a given system a phase transition can take place involving a non-zero amount of heat (latent heat) that is released while the substance is cooled through an infinitesimally small temperature interval around the transition temperature. This type of phase transitions is usually called first-order transitions. Phase transitions that do not involve latent heat are called continuous transitions or second-order phase transitions. They are particularly interesting since typical length and time scales of fluctuations diverge when approaching the critical point. These divergences and the resulting singularities of the order parameters are characteristic of the critical behavior.
In this chapter we will focus on phase transitions in magnetic systems and briefly introduce the basic concepts of critical fluctuations. We refer to the text book of Stanley [3] for a detailed description.

Andrews discovered in 1862 a very special point in the phase diagram of carbon dioxide. At a temperature about 31°C and a pressure of 73 at, the properties of the liquid and vapor phases became indistinguishable. In the neighborhood of this point carbon dioxide strongly scattered light. Andrews called this point the critical point and the strong light scattering the critical opalescence. Later, Pierre Curie (1895) noticed that ferromagnetic iron also shows such a critical point which is called today the Curie point. It is located at zero magnetic field and a temperature of about 770° C, the highest temperature for which a permanent magnetization can exist at zero field. Due to the direction of the magnetization different phases that are indistinguishable appear at this temperature. This phenomenon, that has been classified under “thermal equilibrium phase transitions”can be very well described qualitatively by the Landau theory of phase transitions [4] and are

well understood. The discovery of new interesting transitions in chiral magnetic systems has attracted great scientific interest to this field. In this thesis we investigate equilibrium phase transitions occuring in magnetic systems with intrinsic or induced chiral symmetry.

2.2 Description of Critical Phenomena

For the description of critical phenomena and phase transitions, one can make use of the intrinsic properties of the system such as internal energy U that is described by $U = F - TS$, the free energy F defined as $F = k_B T \ln Z$, the entropy S, the magnetization M defined by

$$M = -\left(\frac{\partial F}{\partial B}\right)_T, \tag{2.1}$$

and the specific heat C defined as

$$C = -T\left(\frac{\partial^2 F}{\partial T^2}\right)_B, \tag{2.2}$$

where T is the temperature, and B the external magnetic field.
According to Landau and Lifshitz [4], we can distinguish between two types of phase transitions denoted first-order and second-order, or discontinuous and continuous, respectively. Usually a continuous phase transition is characterized by an order parameter, a concept introduced by Landau. An order parameter is a thermodynamic quantity that is zero in the disordered phase and non-zero and unique in the ordered phase. The choice of an order parameter is related to a particular phase transition. In the case of a magnetic transition the order parameter is the magnetization. If a singularity appears in the order parameter at a well define critical point, it will have an effect on an entire region around the critical point: a so called critical region. The size of this critical region depends on the materials, but is usually below and above the critical temperature or pressure [3] that the response functions are signifcantly affected. Therefore it is not required that the system is exactly at its critical point in order that the system exhibits remarkable behaviour. It is for this reason that critical phenomena are particularly interesting.
In case the system approaches the critical point, the spatial correlations of the order parameter fluctuations become long ranged. For magnetic systems the correlation length ξ is defined as the distance over which the magnetic moments perceive each other. Close to the critical point the correlation length diverges as $\xi \propto \tau^{-\nu}$ where ν is the critical exponent due to the correlation length and the variable $\tau = (T - T_c)/T_c$ is the reduced temperature.

Critical Fluctuations

We consider fluctuations in the order parameter M. These fluctuations are given by $M - \langle M \rangle$ and they describe the deviation of M from its average at a point r in the material. Furthermore they are tied to the similar fluctuations at the neighboring position r'. The

mathematical description of the magnetic fluctuations is given by the correlation function defined by

$$G(r, r') = \langle [M(r) - \langle M(r) \rangle][M(r') - \langle M(r') \rangle] \tag{2.3}$$

As the temperature approaches T_c, the fluctuations become increasingly important and they strongly depend on the spatial dimensionality of the system.

2.2.1 Critical Exponents and Universality Class

Near the critical point the behavior of a system can be represented by power laws of the deviations of thermodynamic variables from their values at the critical point, hereby defining the critical exponents. The critical behavior of a system at a particular phase transition is completely described by a set of critical exponents. In continuous phase transitions, the equilibrium variables behave in terms of the reduced temperature τ as

$$\begin{aligned} C &= C_0|\tau|^{\alpha}, \text{for } B = 0 && (2.4)\\ M(T) &= M_0|\tau|^{\beta}, \tau \to 0, \text{for } B = 0 && (2.5)\\ \chi(T) &= \chi_0|\tau|^{-\gamma}, \tau \to 0, \text{for } B = 0 && (2.6)\\ \xi(T) &= |\tau|^{-\nu} && (2.7)\\ B &\propto |M|^{\delta}, B \to 0, \tau = 0 && (2.8)\\ & && (2.9) \end{aligned}$$

where α, β, γ, ν, δ, and η are the static critical exponents. The typical time scale for a decay of the fluctuations is the correlation time τ_c which diverges by approaching the critical point via the relation $\tau_c \propto \xi^z$, where z is the dynamical critical exponent.
One of the particular features of a second order phase transition is their universality: All critical exponents are the same for entire classes of phase transitions which may occur in very different physical systems. Theses classes are called universality classes and are determined only by the dimension of the order parameter n, the spatial dimensionality of the system d and the range of the interaction. For a model system belonging to the same universality class, the corresponding critical exponents of a phase transition can be calculated by renormalisation group theory. The mechanism behind universality is the divergence of the correlation length.The values of the most commonly used critical exponents from different model systems are listed in Tab. 2.1.

Scaling Hypothesis

The critical exponents are related via scaling laws and the correlation function as well as the temperature range of the fluctuations scale with the correlation length of the system. The critical exponent are connected by the scaling relations

$$\begin{aligned} 2 - \alpha &= 2\beta + \gamma && (2.10)\\ 2 - \alpha &= \beta(\delta + 1) && (2.11) \end{aligned}$$

Parameter	Physical quantity	Ising	X-Y	Heisenberg
D	spin-dimensionality	1	2	3
d	space dimensionality	3	3	3
γ	correlation length	1.2378	1.316	1.388
ν	susceptibility	0.6312	0.669	0.707
α	specific heat	0.106	-0.01	-0.121
β	magnetization	0.326	0.345	0.367
δ	critical isotherm	4.78	4.81	4.78
η	Fischer exponent	0.039	0.03	0.037

Table 2.1: Critical exponents for various universality classes with short range interactions as taken from Refs. [5, 6].

The exponents of the correlation length and the correlation function are connected by the hyperscaling relations

$$2 - \alpha = d\nu \tag{2.12}$$

$$\gamma = (2 - \eta)\nu \tag{2.13}$$

The dynamical critical exponent z is completely independent from all others since statics and dynamics are decoupled in classical statistics. In the case of isotropic Heisenberg ferromagnets, dynamic scaling states that the critical frequency of the spin fluctuations behaves as

$$\omega(q, \xi) = q^z \Omega(q\xi) \tag{2.14}$$

where the dynamic critical exponent is $z = \frac{d+2-\eta}{2}$. Here d is the spatial dimension of the system. $\Omega(q, \xi)$ is a dynamical scaling function that follows $\Omega(q, \xi) \rightarrow A$ as T_c approaches. A is a constant. The stiffness constant $D \sim \xi^{(2-d+\eta)/2}$ vanishes at the critical temperature, a phenomenon known as renormalisation of the spin waves. Therefore hydrodynamic and dynamical scaling as shown in Fig. 2.1 allow one to determine the behavior of the system near T_C [7]. The impact of the correlation length in the spin correlation function has been demonstrated in the well-known review article by Halperin and Hohenberg (1977) [8]. As illustrated in Fig. 2.1, in the (q, κ)-plane, three regions can be distinguished, in which the spin correlation function has different asymptotic behaviors. The shaded region (a), where $\kappa/q \gg 1$ and $T < T_C$, corresponds to the situation where the wavelength of the spin fluctuations is much larger than the correlation length. This region is called hydrodynamic, since the dynamics of the system can be described by macroscopic equation of motion for spin densities. The region (c) is also related to the long-wavelength or hydrodynmic regime, but in the paramagnetic phase. The region (b) is the critical regime where phenomena occur on a small scale ($\kappa/q \ll 1$) when compared to the correlation length and the hydrodynamic description of the system is not applicable anymore. The spin correlation function is assumed to merge at the lines $\kappa = q$. This region is accessible by neutron scattering.
In the case of the Heisenberg ferromagnet, the Hamiltonian is rotation invariant and a spontaneous symmetry breaking appears in the ordered phase since the magnetization

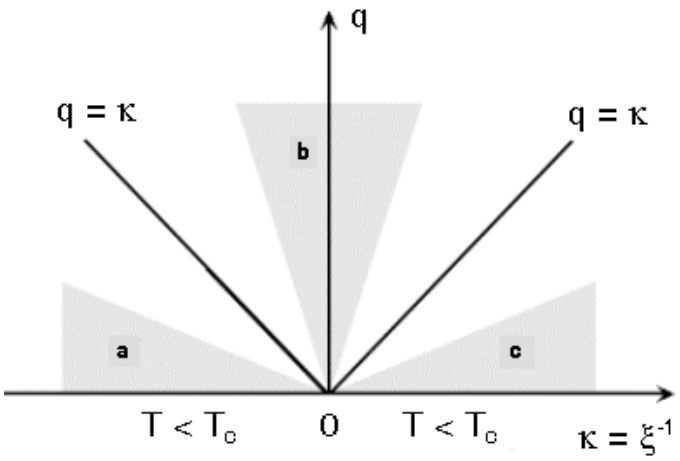

Figure 2.1: Graph from Halperin and Hohenberg showing the macroscopic domain of wave vector q and correlation length ξ. In the shaded regions the correlation functions have different characteristic behaviors.(a) Low temperatures hydrodynamic region: $q\xi \ll 1, T > T_C$ (b) the critical region: $q\xi \gg 1, T \sim T_C$ (c) the high temperature hydrodynamic region: $q\xi \ll 1, T < T_C$.

points in a preferred direction. This effect is responsible for the divergence of the transverse and longitudinal susceptibility below T_C. Please note that in the mean field approximation the longitudinal susceptibility does not diverge below T_C.

2.2.2 Chiral Critical Exponents

The predictions of Kawamura [9] on the existence of new universality classes for magnetic systems with chiral symmetry motivated several theoretical and experimental investigations of critical phenomena in helical magnets. In spite of some experimental validation of the hypothesis of new chiral universality classes, Kawamuras predictions are still subject of controversy. Azaria et al. [10] suggest that the lack of universality of experimental results from Ho, Dy and Tb can be understood as the consequence of a tricritical mean-field behavior for the Heisenberg-like spin-order. In any case, the chirality influences the critical behavior by modifying the conventional critical exponents α, β, γ and ν. New critical exponents β_c, γ_c and ν_c originate from the chirality, the chiral susceptibility and the chiral correlation length, respectively. Most of the recent experimental studies on stacked-triangular antiferromagnets $CsMnBr_3$ [11], $RbMnBr_3$ [12] and rare-earth helimagnets Ho, Dy [13] appear to support the theoretical predictions of Kawamura. The values of chiral critical exponents as predicted theoretically are summarized in Table 2.2

	β_c	γ_c	ν_c	Φ_c
X-Y stacked	0.45 ± 0.02	0.77 ± 0.05	0.55 ± 0.02	1.22 ± 0.06
Heisenberg	0.55 ± 0.04	0.72 ± 0.08	0.60 ± 0.03	1.27 ± 0.1

Table 2.2: Critical exponents for chiral universality classes as taken according to Ref. [14]

.

Comparing the value of the chiral exponents with those of the conventional universality classes, the exponent α and β_c in the chiral case is clearly larger than the standard values, while γ_c and ν_c are smaller. The difference $\beta_c - 2\beta = 0.137$ has been found experimentally [15]. The obtained chirality exponents also satisfy the scaling relations as predicted by the renormalization group analysis

$$\alpha_c + 2\beta_c + \gamma_c = 2 \tag{2.15}$$

This observation, as well as the finding that the chirality ordering occurs simultaneously with the spin ordering supports the scenario suggested by the renormalization group theory, namely, the chirality ordering in $d = 3$-dimensional chiral systems is parisitic to the spin ordering and is controlled by a new chiral crossover exponent $\Phi_c = \beta_c + \gamma_c$ whose value can be estimated as $\Phi_c = 1.22 \pm 0.06$ [14].
Chiral critical exponents in in 3d-antiferromagnet $CsMnBr_3$ have been determined experimentally by Plakhty [11], who find $\beta_c = 0.42$, $\gamma_c = 0.84$ and $\Phi_c = 1.28$ in good agreement with theoretical predictions.

2.3 Critical Spin Fluctuations in Magnetic Systems

Magnetism in solids originates from the magnetic moment of the atoms of the system. The magnetic moment itself is caused by the spin and angular momenta of the electron. Two opposite concepts have been proposed to describe the magnetism: the localized and itinerant models. The former start with the electronic states localized in real space, while the latter start with states localized in reciprocal space [16].
In this section we briefly introduce some general aspects of the theory of spin fluctuations in localised and itinerant electron magnetism. We refer to the book of Moriya for detailed information [16].

2.3.1 Spin Fluctuations in Localized Magnetism

The idea of localized moments was introduced by Weiss. He argued that the individual magnetic moments interact between each other and therefore can align. He explained this interaction by a mean molecular field. Heisenberg attributed this field to the quantum mechanical exchange between neighboring atoms as schematically illustrated in Fig. 2.2. If $\vec{S}_i$ is the atomic spin operator at a given position, the Heisenberg model for magnetism is described by

$$H = \sum_{i,j} J_{ij} \vec{S}_i \vec{S}_j \tag{2.16}$$

where J_{ij} is the inter-atomic exchange interaction between the i^{th} and j^{th} spins. Within this model the Curie-Weiss law predicting a linear temperature dependence of the inverse magnetic susceptibility $\chi^{-1} \propto (T - T_c)$ is naturally explained. Moreover, systems with localized moments are expected to have a saturation magnetization M_S, which is an integer multiple of the Bohr magneton μ_B.
If dipolar forces between spins are taken into account, an additional interaction term can

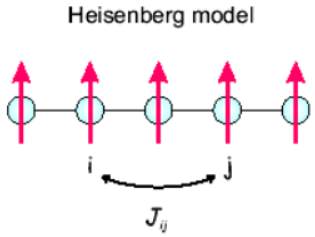

Figure 2.2: Heisenberg model of magnetism based on localized moments.

be introduced, which is purely of magnetic origin. Therefore the Heisenberg Hamiltonian is modified as

$$H_{dipolar} = -\sum_{i,j}\sum_{\alpha,\beta} U_{ij}^{\alpha\beta} S_i^{\alpha} S_j^{\beta} \tag{2.17}$$

here $U_{ij}^{\alpha\beta} = J_{ij}\delta^{\alpha\beta} + g(\delta^{\alpha\beta}/r_{ij}^3 - 3r_{ij}^{\alpha}r_{ij}^{\beta}/r_{ij}^5)$ where g is the strength of the dipolar interaction that are long range and anisotropic and r_{ij} is the distance between the i^{th} and j^{th} spins. The dipolar interaction leads to new critical behaviour.

Critical Behaviour

A theory to explain the critical behaviour of a spin system near the transition temperature T_c has been proposed by Kadonoff [17]. This theory claims that the long range correlation of spin fluctuations in the vicinity of T_c is responsible for any singularity in the order parameter, namely for the magnetic phase transition. This statement is related to the existence of a spin correlation length.
In the ordered phase of a single domain isotropic ferromagnet, the direction of the magnetization defines three natural directions connected with diagonal components of the susceptibility tensor. There is one component directed along M that is denoted $\chi_{\parallel}(q)$ and two components transverse to M, namely $\chi_{\perp 1,2}(q)$. In the case of an isotropic ferromagnet, the static susceptibilty below T_c is predicted within the mean field theory to vary as

$$\chi_{\parallel}(q) \propto 1/(q^2+\kappa^2) \tag{2.18}$$
$$\chi_{\perp 1,2}(q) \propto 1/q^2 \tag{2.19}$$

where q is the reduced scattering vector and κ the correlation length below T_c. In the paramagnetic phase the correlation length has the same temperature dependence as the one below T_c.
Close to T_c and at small wave-vectors q, the mean field approximation fails to describe the actual behaviour of the system since the fluctuations are neglected. Furthermore the static susceptibility $\chi(q)$ is connected with the spin correlation function as

$$\chi(q) \propto q^{\eta-2} f(\kappa/q) \tag{2.20}$$

where κ is the inverse correlation length, q is the wave vector and η the Fischer exponent that is the correction term to the mean field approximation. According to Ref.[18] its

value is $\eta = 0.042 \pm 0.014$ in the case of 3D ferromagnets. Eq. 2.20 shows that the spin correlation function at any temperature near T_c and wave-vector q is determined by the static properties at T_c via the scaling function $f(\kappa/q)$ that take an Ornstein-Zernicke form [7]

$$f(\kappa/q) = \frac{1}{1 + (\kappa/q)^2}. \tag{2.21}$$

Beyond mean field approximation, the spin dynamics of an isotropic ferromagnet can be described within the framework of mode coupling theory. In the hydrodynamic regime ($q/\kappa \gg 1$) the parallel susceptibility is modified as follows

$$\chi_{\parallel}(q) \propto 1/q\kappa \tag{2.22}$$

Therefore in the limit $q \rightarrow 0$ the longitudinal susceptibility is predicted to diverge at any temperature below T_c. So far the crossover between the hydrodynamic regime and the critical regime (see Fig. 2.1) can not be observed experimentally since the q/κ-range needed is rather difficult to achieve by means of neutron scattering.

2.3.2 Spin Fluctuations in Itinerant Magnetism

An alternative approach to understand the magnetism in metals is given by the itinerant model as proposed by Stoner [19]. One of the main reasons to propose a different model is that the saturation magnetization M_S is not an integer multiple of μ_B. In the Stoner model, magnetism in metals arises from a splitting between up- and down-spin bands and it is favored when the density of states is high at the Fermi level as shown schematically in Fig. 2.3.

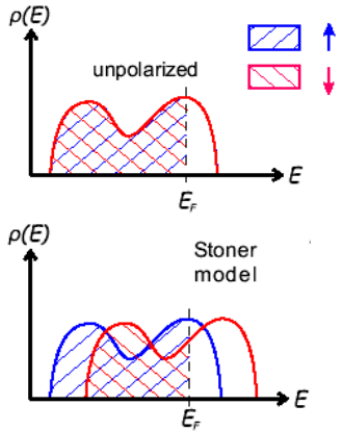

Figure 2.3: Stoner model of itinerant magnetism. The shaded region is occupied by electrons. If the magnetization increases, the kinetic energy of an electron system splits the energy bands for up- and down-spin electrons (lower panel) [16].

The magnetic susceptibility of the interacting system can be obtained by determining the total magnetization of the system and taking the derivative

$$\chi_{Stoner} = \frac{\partial M}{\partial H} = \frac{g^2\mu_B^2}{2}\rho(E_F)\frac{1}{1 - U\rho(E)} \tag{2.23}$$

where $\rho(E)$ is the electron density of states at the Fermi level and $g^2\mu_B^2\rho(E_F)/2$ is the Pauli paramagnetic susceptibility. The magnetic susceptibility of an interacting system

is enhanced by the Stoner factor $1/[1 - U\rho(E_F)]$ when compared with the free electron susceptibility. If $U\rho(E_F) > 1$ then the system becomes ferromagnet. However, in this form, the Stoner model fails to reproduce the measured T_c and the observed Curie-Weiss law above T_c. Indeed , the temperature dependence of the magnetization is expressed as

$$M(T) = M(0)\left(1 - (T/T_c)^2\right)^{1/2} \tag{2.24}$$

This expression fits the actual behavior of itinerant magnets only near $T = 0$. The effect of critical spin fluctuations and spin waves is expected to modify significantly the magnetic equation of state at finite temperatures.

Random Phase Approximation (RPA)

In a better approximation the dynamical spin susceptibility of itinerant systems is given by the Heisenberg equation of motion for spin densities that are solved within a random phase approximation. This theory predicts that in addition to the spin-flip excitations (Stoner excitations), collective spin excitation may exist at long wavelengths.

$$\chi_{RPA}(q,\omega) = \frac{\chi_{\Delta 0}(q,\omega)}{1 - I\chi_{\Delta 0}(q,\omega)} \tag{2.25}$$

with

$$\chi_{\Delta 0}(q,\omega) = \sum_{\kappa} \frac{f(E_{\kappa+q} + \Delta) - f(E_\kappa - \Delta)}{E_\kappa - E_{\kappa+q} - 2\Delta + \omega} \tag{2.26}$$

where 2Δ is the energy gap between the spin-up and spin-down electron band and $f(E)$ the Fermi-Dirac distribution function. $I = U/N$ is an effective interaction between the electrons. In this form, the RPA theory is a valuable contribution in understanding the itinerant magnetism. However, serious discrepancies between theoretical and experimental data still presist.

SCR Theory of Spin Fluctuations

The development of the self-consistent renormalization theory (SCR) [16] was mostly motivated by the results of magnetic susceptibilities in weakly ferromagnets as $ZrZn_2$ and Sc_3In, where the data showed a good agreement with the Curie-Weiss behavior. The local moment picture is clearly inadequate and the RPA theory cannot explain the Curie-Weiss law consistently. Moriya and Kawabata proposed the SCR theory, which takes into account the spin fluctuations and it requires that the susceptibility and the free energy of the system must be calculated at the same time, so that the static as well as long wavelength limit of the dynamic susceptibility agrees with that calculated from the renormalized free energy. For this purpose the dynamical susceptibility is modified as follows [16]

$$\chi(q,\omega) = \frac{\chi_0(q,\omega)}{1 - I\chi_0(q,\omega) + \lambda_{MI}(q,\omega)}. \tag{2.27}$$

Here $\lambda_{MI}(q,\omega)$ represents the mode-mode coupling of the spin fluctuations. $\lambda_{MI}(q,\omega)$ contributes to produce a $T^{3/2}$ dependence of the magnetization at low temperatures and

the Curie-Weiss law for $\chi(0,0)$ above the Curie temperature. In other words this term predicts long wavelength spin fluctuations in the itinerant electron system like in the Heisenberg system.
In weak itinerant ferromagnets like MnSi, only fluctuations with long wavelengths are important. $\chi_{M0}(q,\omega)$ and $\lambda(q,\omega)$ are expressed as [20]

$$\chi_0(q,\omega) = \chi_0(0,0)(1 - Aq^2 + ... + iB(\omega/q)) \quad (2.28)$$
$$\lambda_{MI} = \lambda(0,0) = \lambda_0 T. \quad (2.29)$$

Therefore Eq. 2.27 can be expressed as [20]

$$\chi(q,\omega) = \frac{c\omega q}{\Gamma_0^2 q^2[\kappa(T)^2 + q^2]^2 + \omega^2} \quad (2.30)$$

where $\kappa^2(T) = \kappa_0^2(T/T_c - 1)$, $\Gamma_0 = A/B$ and $\kappa_0^2 = \lambda_0 T_c / I_0 \chi_0 A$. This is equivalent to the double Lorentzian expression for paramagnetic spin fluctuations in an itinerant spin system [16]

$$\chi(q,\omega) = \frac{cq}{\kappa(T)^2 + q^2} \frac{\Gamma(q)\omega}{\Gamma(q)^2 + \omega^2} \quad (2.31)$$

if $\Gamma(q)$ is expressed as

$$\Gamma(q) = \frac{cq}{\chi(q)} = \Gamma_0 q(\kappa^2 + q^2). \quad (2.32)$$

The difference with the localised spin system appears in the expression for $\Gamma(q)$. In the localized spin system, $\Gamma = cq^2/\chi(q)$ is proportional to the square of the wave-vector q [16].

Moriya and Makoshi [21, 22] developed the SCR theory of helical spin structure. They showed that the helical structure is stable when the system has a small magnetic anisotropy and the spin ordering vector is small. Therefore the spin structure is predicted to be conical in an external magnetic field. The cone angle decreases with increasing field but the amplitude of the local spin density remains unchanged until the cone angle becomes zero at the critical field B_C, beyond which simple ferromagnetism arises. The magnetization increases for $B > B_C$ with increasing magnetic field as in weak ferromagnetic systems. The SCR theory successfully describes several properties of weak itinerant ferromagnets. These weak itinerant systems like for example MnSi are characterized by (i) a low Curie temperature (usually lower than $50\,\mathrm{K}$), (ii) they follow a Curie-Weiss law quite precisely in the temperature interval $T_c < T < 10T_c$ (iii) the magnetization inferred from the Curie-Weiss law is several times lower than the saturation magnetization.

2.4 Magnetic Reorientation Transitions

After the work of Nakinishi et al. [23] and Bak and Jensen [24] who show the importance of the crystal structure of itinerant systems like MnSi in stabilizing the helical spin-density-wave. Plumer and Walker [25] proposed a mean-field theory to explain the spin and wave-vector rotation induced by an external magnetic field in itinerant magnets.
Shown in Fig. 2.4 is a schematical representation of a typical helical spin density wave.

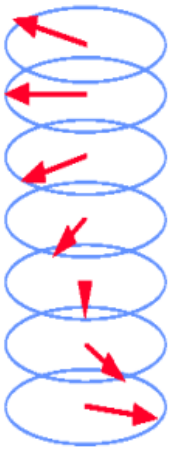

Figure 2.4: Schematic representation of an helical spin density wave that is described by Eq. 2.33.

By assuming that the external magnetic field is homogeneous, the spin density is defined as

$$s(r) = m + S\exp(i\vec{q}\cdot\vec{r}) + S^{\star}\exp(-i\vec{q}\cdot\vec{r}) \tag{2.33}$$

where m is the homogeneous contribution to the spin density which is induced by the external magnetic field. $\vec{q}$ is the wave vector. S is called the spin-density-wave polarization-vector. The free energy is assumed to be a function of S, m and $\vec{q}$. All terms of the orders S^2 m^2, qS^2, q^2S^2, m^2S^2, S^4 and m^4, which are invariant under the operations of the crystal symmetry group and the operation $S \rightarrow S^{\star}$ and $\vec{q} \rightarrow -\vec{q}$ are considered. The resulting free energy is simplified to [25]

$$\begin{aligned} F &= \frac{1}{2}A_0m^2 + A_qS^2 + B_0(m^2S^2 + S^4 + \frac{1}{4}m^4) \\ &\quad + B'm_{\perp}^2S^2 + (\frac{1}{2}\tilde{D}q^2S^2 + \frac{1}{2}ES^4)g - m_{\parallel}H\cos\theta - m_{\perp}H\sin\theta \qquad (2.34) \\ g &= 1 + \beta_1^4 + \beta_2^4 + \beta_3^4 \qquad (2.35) \end{aligned}$$

where all coefficients depend only on temperature. β_1, β_2 and β_3 are the direction cosines of q relative to the crystallographic axes, θ is the angle between q and the external field H; $m_{\parallel}$ and $m_{\perp}$ are the components of m parallel and perpendicular to q, respectively. D_m is the Dzyaloshinskii-Moriya term. For small q values the expansion coefficients A_0 and $A_q = A_0 + A_1q^2 + D_mq$ are expressed by $A_0 = a(T - T_0)$ and $A_q = a(T - T_q)$ with $T_0 \leq T_q$ because the details of the Dzyaloshinskii-Moriya interaction of the form $2D_m\vec{q}\cdot(S_x \times S_y)$ are hidden in A_q [25, 26]. A and $\tilde{D}$ are the anisotropy coefficients, that are considered to be much smaller than the corresponding coefficients to the isotropic terms therefore $E \ll B$ and $\tilde{D}q^2 \ll A_0 - A_q$.
In the absence of an external magnetic field, the free energy is minimized with $q \parallel \langle 111\rangle$ if the coefficient of g is positive. If $g < 0$, the spiral is stabilized with q along $\langle 100\rangle$. The chirality of the magnetic helix is controlled by the sign of the coefficient D_m of the Dzyaloshinskii-Moriya term.
In the presence of a finite applied magnetic field $\vec{H}$ the Zeeman coupling $-\vec{H}\cdot\vec{m}$ is included. Plumer and Walker [25] argue that a coupling between $\vec{q}$ and $\vec{H}$ exists through

the relation

$$-\vec{m}\cdot\vec{H}+B'm_{\perp}^{2}S^{2} \tag{2.36}$$

where the first term may be minimized by a configuration where $\vec{q}$ is parallel to $\vec{H}$, a situation, which is in agreement with experimental results [26]. The coefficient B' must be positive so that S will be forced to lie perpendicular to an applied magnetic field [25]. The term $B'm_{\perp}^{2}S^{2}$ tends to cause $\vec{q}$ to become parallel to the magnetic field direction (since $B'>0$). The competition between this term and the other anisotropy terms leads to the gradual rotation of the wave vector towards the field with increasing field. The theories developped for MnSi by Plumer and Walker [25] and Kataoka and Nakanishi [27] have both predicted that the rotation of a wave-vector $\vec{q}$ initially along the $\langle 001\rangle$ direction should be about the $\langle 1-10\rangle$ direction so that $\vec{q}$ is rotated towards the $\langle 111\rangle$ direction. Walker [28] suggest that there is not one, but two successive phase transitions as the magnetic field is reduced in magnitude. At the first transition, the wave-vector $\vec{q}$ initially along $\langle 001\rangle$, begins to rotate about $\langle 010\rangle$ or $\langle 100\rangle$; subsequently, a second transition takes place in which the $\vec{q}$ begins to rotate towards the $\langle 111\rangle$ direction when the magnetic field is reduced below a certain critical value.

Paramagnetic Fluctuations in Systems with DM Interaction

Maleyev [29] proposed a theoretical description of the paramagnetic fluctuations in systems without inversion symmetry based on the Bak-Jensen model [24], which takes into account the exchange interaction, the Dzyaloshinskii-Moriya (DM) interaction and the anisotropic exchange interaction. The bilinear part of the free energy density has been derived [29]

$$W(q)=\left(\frac{J}{2}(q^{2}+\kappa_{0}^{2})\delta_{\alpha\beta}+iD_{m}\epsilon_{\alpha\beta\gamma}q\right)S_{q}^{\alpha}S_{-q}^{\beta}+\frac{A_{m}}{2}(q_{x}^{2}|S_{q}^{x}|^{2}+q_{y}^{2}|S_{q}^{y}|^{2}+q_{z}^{2}|S_{q}^{z}|^{2}), \tag{2.37}$$

where the terms with the coefficients J, D_m and A_m correspond to the isotropic exchange interaction, the Dzyaloshinskii-Moriya interaction and the anisotropic exchange interaction, respectively. $\kappa_0^2=C_0(T-T_{c0})$ and T_{c0} are the non-renormalized square of the inverse correlation length and the transition temperature, respectively. According to Maleyev [29, 30], the Dzyaloshinskii-Moriya interaction and the anisotropic exchange interaction are of first and second order in the spin-orbit interaction. As a result we have $J>D_ma>A_m$, where a is the lattice constant [29]. In the exchange approximation for the magnetic susceptibility we have the well-known expression $\chi_{\alpha\beta}=\chi_0\delta_{\alpha\beta}$ and $\chi_0=T/[J(q^2+\kappa^2)]$ and using Eq. 2.37 for the susceptibility tensor we obtain

$$\chi_{\alpha\beta}(q)=\chi_{0}(q)\delta_{\alpha\beta}+\chi_{0}(q)K_{\alpha\mu}(q)\chi_{\mu\beta}(q), \tag{2.38}$$

where the tensor $K=K^A+K^S$. Its antisymmetric part $K_{\mu\beta}^A=-i(D_m/T)q\epsilon_{\gamma\mu\beta}$. For the symmetric part we have $K_{xx}^S=-(A_m/J)q_x^2$, $K_{yy}^S=-(A_m/J)q_y^2$, $K_{zz}^S=-(A_m/J)q_z^2$. The solution of Eq.2.38 has the form [29, 31]

$$\chi_{\alpha\beta}=\frac{\chi_{0}}{Det}\left(\delta_{\alpha\beta}-\frac{2ikq}{q^{2}+\kappa_{0}^{2}}\hat{q}\epsilon_{\gamma\alpha\beta}-\left(\frac{2kq}{q^{2}+\kappa_{0}^{2}}\right)^{2}\hat{q}_{\alpha}\hat{q}_{\beta}\right), \tag{2.39}$$

where $\hat{q} = \vec{q}/|\vec{q}|$, $k = |D_m|/J = 2\pi/d$ and d is the length of the spiral. Here, in the numerator small terms of the order $A_m q_{x,y,z}^2/[J(q^2+\kappa_0^2)]$ were omitted [29] and

$$Det = 1 - \left(\frac{2kq}{q^2+\kappa^2}\right)^2 - \frac{4k^2q^4}{(q^2+\kappa_0^2)^3}\frac{A_m}{J}(\hat{q}_x^4 + \hat{q}_y^4 + \hat{q}_z^4) \tag{2.40}$$

here we retain only one term proportional to the small ratio A_m/J as it has cubic symmetry that breaks the full rotational symmetry of the problem. It is responsible for the orientation of the helices with respect to the cubic axes. Using these equations we can write

$$\chi_{\alpha\beta} = \frac{T}{JZ}\left((q^2+\kappa_1^2+\kappa^2)\delta_{\alpha\beta} - 2ikq_\gamma\epsilon_{\gamma\alpha\beta} - \frac{(2qk)^2}{q^2+\kappa_1^2+\kappa^2}q_\alpha q_\beta\right) \tag{2.41}$$

$$Z = [(q+k)^2+\kappa^2]\left((q-k)^2+\kappa_1^2 - \frac{q^2k^2}{q^2+\kappa_1^2+\kappa^2}\frac{A_m}{J}(\hat{q}_x^4+\hat{q}_y^4+\hat{q}_z^4)\right) \tag{2.42}$$

where $\kappa_1^2 = \kappa_0^2 - \kappa^2 = C_0(T - T_{c1})$ and $T_{c1} = T_{c0} - \kappa^2/C_0$. As the ratio $|A_m|/J$ is very small the last term in the expression for Z is important only in the vicinity of T_c. As a result for $\kappa_1^2 > |A_m|/J$ critical fluctuations are maximal at $q = k$ and uniformly distributed on a ring. However very close to T_c, when $\kappa_1^2 \leq |A_m|/J$ the last term determines the form of the critical fluctuations.

The expression $\hat{q}^4 = \hat{q}_x^4 + \hat{q}_y^4 + \hat{q}_z^4$ is a cubic invariant. It has two extrema equal to 1 and $1/3$ for $\vec{q}$ along the edges and the diagonals of the cubic unit cell, respectively. As a result for $A_m > 0$ we have a transition to a state with the helix axes along the edges (for example in the case of FeGe [32]) and for $A_m < 0$ along the diagonals as it is the case for MnSi [33] and follwing expression is obtained

$$Z = [(q+k)^2+\kappa^2]\left((q-k)^2+\kappa^2 + \frac{k^2|A_m|}{2J}\left(\hat{q}^4 - \frac{1}{3}\right)\right), \tag{2.43}$$

where $\kappa^2 = \kappa_1^2 + k^2|A_m|/6J$. Here, in the first factor and in the last term we neglected a small difference between κ_1^2 and κ^2 and set $q = k$, respectively.

The Eqs. 2.37 to 2.43 are expected to give a qualitavely description of the paramagnetic spin fluctuations in itinerant systems and they will be used to analyse the experimental data from MnSi.

Chapter 3

Experimental Methods

Imagination is more important than knowledge.
Albert Einstein

3.1 Measurements of Bulk Properties

In the vicinity of the Curie temperature the magnetisation diverges. A suitable method is required. One must also impose more stringent requirements on the system for controlling the temperature. In this section we present briefly the principle of measurement of macroscopic magnetic properties relavant for the present work.

3.1.1 Magnetization

The DC and AC magnetization of a ferromagnetic sample may be measured in several ways. Here we mention three of them. These are the force method, the torque method and the induction technique, the latter being the most common in modern instruments like the Quantum Design Physical Property Measurement System [34] used for our investigations. A schematic view of experimental set-up used for AC and DC magnetic measurements on PPMS is shown in Fig. 3.1.
In DC magnetometry using induction technique, the sample moves either by vibration or by one-shot extraction relative to a set of pickup coils. A typical extraction speed for the PPMS is 100 cm/s. The magnetization is obtained by magnetising the sample with a constant magnetic field and measuring the voltage induced by the sample in the pick-up coils. The detected voltage is proportional to the magnetic flux through the coils. The magnetic moment $M(H)$ of the sample is obtained through a numerical integration of the voltage profile and then fitting the data to the known waveform of a dipole moving through the pick-up coils.
In AC magnetic measurements, a small AC drive magnetic field is superimposed on the DC field, causing a time-dependent moment in the sample. The field of the time-dependent moment induces a current in the pick-up coils making measurement without sample motion possible [34]. The AC field amplitude range available on the PPMS is 2 mOe to 15 Oe with a frequency range from 10 Hz to 10 kHz. The magnetometer cir-

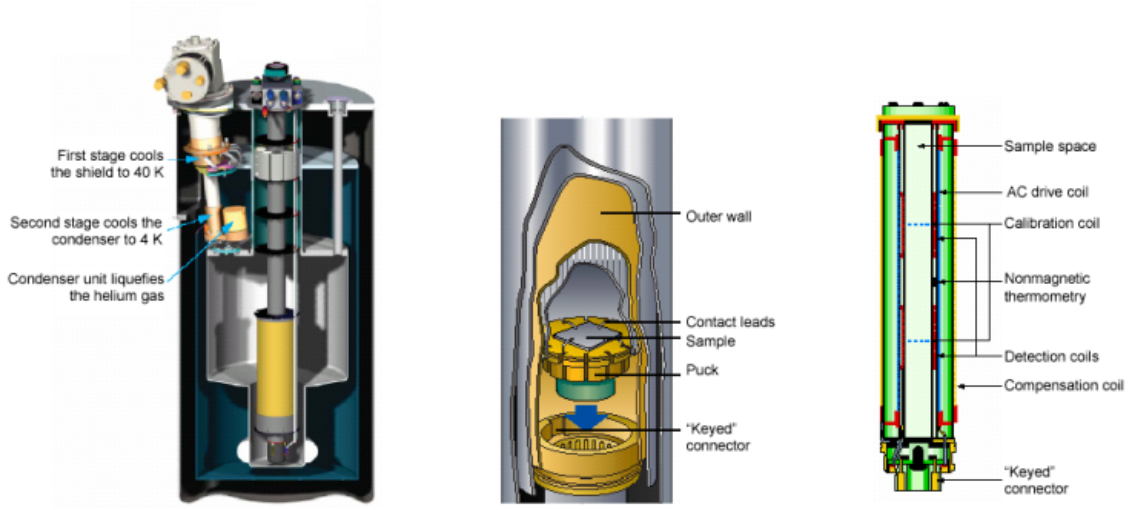

Figure 3.1: Schematic view of experimental set-up used for AC and DC magnetic measurements on PPMS. Left: Cut view of the dewar. Middle: Sample chamber. Right: Schematic of PPMS magnetic coil set [34].

cuitry is configured to detect only in a narrow frequency band corresponding to the frequency of the AC drive field. At very low frequencies AC magnetometry is most similar to DC magnetization. At higher frequencies, the AC moment of the sample is different from the DC magnetization curve due to dynamic effects in the sample. Therefore the AC susceptibility is also called dynamic susceptibility. The sample magnetization may lag behind the drive field, an effect that is detected by the detection circuitry. Thus, the AC magnetic susceptibility yields two quantities, the magnitude of the susceptibility, χ, and the phase shift, $\phi = \arctan(\chi''/\chi')$ via $\chi = \chi' + i\chi''$. Here χ' is an in-phase, or real part of the susceptibility and χ'' is an out-of-phase, or imaginary component of the susceptibility and gives indications of dissipative processes in the sample. AC magnetometry is very sensitive to small changes in the dynamic susceptibility and thus a powerful tool to explore the magnetic phase transitions.
The accuracy of both AC and DC magnetic measurements varies from 3.10^{-5} emu to 1.10^{-8} emu. The available temperature is $1.9\,\mathrm{K} < T < 400\,\mathrm{K}$ with an accuracy better than 0.05 K.

3.1.2 Specific Heat

The specific heat anomaly is a key signature of any phase transition. Indeed a careful examination of the specific heat anomaly in magnetic systems is expected to yield useful information regarding the mechanism of magnetic phase transitions. The PPMS uses a sensitive technique to measure the specific heat via the relaxation method developed by Hwang et al. [35]. The principle of this method is illustrated on Fig. 3.2. The heat capacity C is measured at constant pressure ($p < 10^{-4}$ Torr) at zero or applied magnetic field employing this method. It controls the heat added and removed from a sample while monitoring the resulting change in temperature as illustrate in Fig. 3.3. A heater connected to

the sapphire platform of the sample holder induces a constant heat pulse in the sample. The relaxation is then measured at the equilibrium temperature.

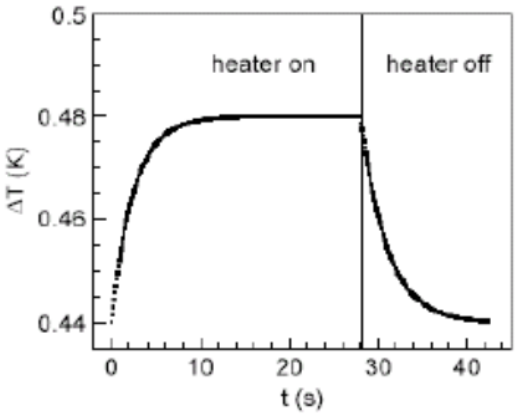

Figure 3.2: Illustration of the relaxation method for specific heat measurements. A heat pulse is applied on the sample and the time relaxation of the sample temperature is measured.

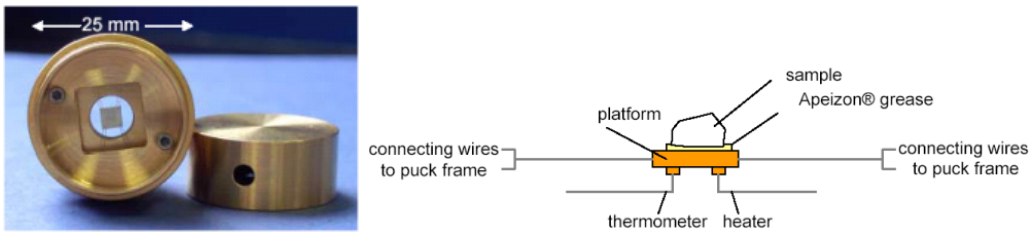

Figure 3.3: Heat capacity puck with sample platform and connecting wires are visible. A sapphire platform is hold by eight wires that are used to measure the time relaxation.

Fig. 3.3 shows the heat capacity puck used in the PPMS heat capacity option as used for this work. The vacuum grease Apiezon N from Quantum Design is used in the temperature range from $1.9 - 320\,\mathrm{K}$ and the silicon oil based Wakefield compound 120-2 is used for thermal coupling. Typical sample masses are in the range $1 - 200\,\mathrm{mg}$. Due to a Schottky anomaly of the wire material that changes in the signal, the sample holder wires connecting the outer frame and the sapphire platform must be calibrated in each magnetic field below $T = 20\,\mathrm{K}$. Thermal contact between the sample and the sample platform is provided by a thermal joint compound whose contribution to the sample specific heat has to be calibrated for each sample at each applied magnetic field.

3.2 Neutron Scattering

3.2.1 Introduction

The magnetic moment of neutrons make it a powerful tool for investigating physical properties of condensed matter. The interaction of the neutron spin with the electronic and nu-

clear spin of the system provides information about structural properties as well as lattice dynamics and magnetic fluctuations.
In this section we present an overview of the principle of magnetic neutron scattering and introduce some concepts and formula that are relevant for the present investigation. We refer to the text books of Squires, White and Lovesey [36, 37, 38] for detailed informations.

Magnetic neutron scattering plays a crucial role in the determination and comprehension of the microscopic properties of a large number of magnetic systems, from the fundamental nature and symmetry of magnetically ordered materials to elucidating the magnetic characteristics essential in applications.
Small angle neutron scattering is a technique to explore the magnetism over longer distances than conventional diffraction, and is ideal to study domain structures and other spatial variations of the magnetization density on length scales from $1 - 1000\,\mathrm{nm}$.
The general idea of a neutron scattering experiment is to place a sample in the beam of incident neutron of mass m_n, with a well-defined wave vector k_i and known incident flux and to measure the number of neutrons scattered in a solid angle $d\omega$ (as illustrated Fig. 3.4) with an energy between E_f and $E_f + dE_f$.
The non-polarized neutron scattering cross section is then given by

$$\left(\frac{d\sigma^2}{d\Omega dE_f}\right)_{\lambda_i \to \lambda_f} = \frac{k_f}{k_i}\left(\frac{m_n}{2\pi\hbar^2}\right)^2 \sum_{\lambda_i,\lambda_f,\sigma_i\sigma_f} p_{\lambda_i} |\langle k_f \sigma_f \lambda_f | \hat{V} | k_i \sigma_i \lambda_i \rangle|^2 \delta(\hbar\omega + E_{\lambda_i} - E_{\lambda_f)} \tag{3.1}$$

where σ and $\lambda_{i,f}$ are the spin state and quantum state of the sample respectively. p_{λ_i} is the probability that the sample is in the initial state $|\lambda_i\rangle$. $\hat{V}$ is the scattering potential that represents the scattering between the neutron and the sample. $\hbar\omega$ is the energy transfer which is defined via the conservation law of energy and momentum

$$\hbar\omega = \frac{\hbar^2}{2m}(k_i^2 - k_f^2) = E_i - E_f \tag{3.2}$$

$$\hbar\vec{Q} = \hbar(\vec{k}_i - \vec{k}_f) \tag{3.3}$$

where E_i and E_f are the initial and final energy of the neutron respectively. q represents the scattering vector.

Nuclear Scattering

The nuclear forces between the neutron and the nuclei are very short range when compared with the typical inter-atomic spacing. It is represented by the Fermi pseudo-potential

$$\hat{V}(r) = \sum_j \frac{2\pi\hbar^2}{m} b_j \delta(\vec{r} - \vec{r}_j) \tag{3.4}$$

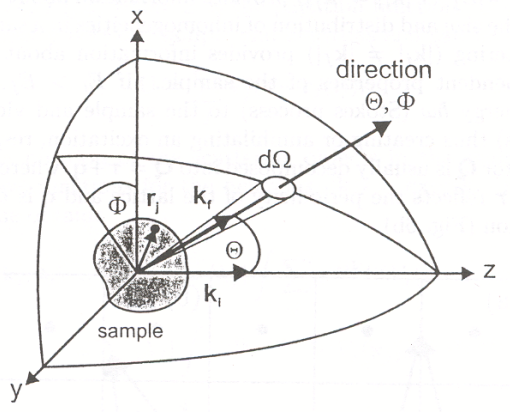

Figure 3.4: Geometry of a scattering experiment. An incident neutron with wavelength k_i is scattered into a solid angle $d\Omega$.

where b_j is the scattering length of a nucleus i located at position $\mathbf{r}_j$. This leads to the differential cross section

$$\left(\frac{d^2\sigma}{d\Omega dE_f}\right) = \left(\frac{d^2\sigma}{d\Omega dE_f}\right)_{coh} + \left(\frac{d^2\sigma}{d\Omega dE_f}\right)_{incoh} \tag{3.5}$$

$$= NS_{coh}(q,\omega)\frac{\sigma_{coh}}{4\pi}\frac{k_f}{k_i} + NS_{incoh}(q,\omega)\frac{\sigma_{incoh}}{4\pi}\frac{k_f}{k_i} \tag{3.6}$$

where S_{coh} represents the coherent scattering of elements that are correlated in space and time, whereas S_{incoh} gives only the space correlation of the same nuclei at different times. The coherent scattering gives rise to interference effects which provide information about the collective excitations of the material. In the case of SANS the incoherent contribution to the scattering process is negligeable due to the small angles. For our investigations the nuclear scattering is not relevant since we focus on the magnetic scattering.

3.2.2 Magnetic Scattering

Due to the spin of the neutron, there is a strong interaction between the magnetic moment of the neutron and the magnetic field $\vec{B}$ created by the unpaired electrons in the sample. The magnetic interaction operator between sample and neutrons is given by:

$$U_m = -\vec{\mu}\cdot\vec{B} = -\gamma\mu_N\vec{\sigma}\cdot\vec{B} \tag{3.7}$$

where $\gamma = -1.913$ is the gyro-magnetic ratio and $\mu_N = 5.051\times10^{-27}J/T$ is the nuclear magneton. Note that $\vec{\mu}$ is anti-parallel to $\vec{\sigma}$. An unpaired electron at $r = 0$ produces at the positions r_j a magnetic field that is given by:

$$\vec{B}_j = \Delta\times\{\frac{\mu_e\times\vec{r}_j}{|\vec{r}_j|^3}\} + \frac{(-e)}{c}\frac{\vec{v}_e\times\vec{r}_j}{|\vec{r}_j|^3}. \tag{3.8}$$

The first term ($\vec{\mu_e} = -2\mu_B\vec{S}$) describes the field due to the magnetic moment of the electron and the second term describes the magnetic field due to the orbital motion of the

electron. v_e is its velocity. The Fourier transformation of Eq. 3.8 gives the expression for the magnetic scattering length p of an electron

$$p = -\gamma r_0 \vec{\sigma} \cdot \left(\vec{q} \times (\vec{S} \times \vec{q}) + \frac{i}{\hbar |\vec{q}|} (\vec{P}_e \times \vec{q}) \right) = -\gamma r_0 \frac{g}{2} \vec{\sigma} \cdot \left(\vec{q} \times (\vec{S} \times \vec{q}) \right). \qquad (3.9)$$

where $r_0 = 0.2818 \cdot 10^{-12}$ cm is the classical radius of the electron withe the momentum $\vec{P}_e$.

Eq. 3.9 shows that only spin components perpendicular to the scattering vector $\vec{q}$ contribute to the magnetic scattering cross section. This provides an important selection rule for distinguishing between magnetic and nuclear scattering.

In order to obtain the cross section for magnetic scattering, we replace U_m in Eq. (3.7) by

$$U_m = \frac{2\pi\hbar^2}{m} \sum_j p_j F_j(q) \delta(\vec{r} - \vec{r}_j(t)) \qquad (3.10)$$

where p_j is the magnetic scattering length of an electron, $F_j(q)$ is the magnetic form factor of the atom j at the position r_j. $F_j(q)$ is given by the Fourier transform of the normalized spin density of the unpaired electrons, i.e. $F_j(q = 0) = 1$[8]. Because the atomic orbitals are extended in space, $F(q)$ is peaked near the forward direction, but not necessarily at $q = 0$.

The magnetic cross section for neutrons with the initial and final spin states σ_i and σ_f, respectively, becomes

$$\left(\frac{d\sigma}{d\Omega dE_f} \right)_{mag}^{\sigma_i \to \sigma_f} = \frac{k_f}{k_i} (\gamma r_0 \frac{g}{2} F(q))^2 \sum_{\alpha,\beta} (\delta_{\alpha\beta} - q_\alpha q_\beta) S^{\alpha\beta}(q, \omega), \qquad (3.11)$$

where $S^{\alpha\beta}(q, \omega)$ is the magnetic scattering function.

$$S^{\alpha\beta}(\vec{q}, \omega) = \frac{1}{2\pi\hbar} \int \sum_{ij} \langle S_{j\alpha}(0) S_{i\beta}(t) \rangle \langle e^{-i\vec{q}\cdot\vec{r}_j(0)} e^{i\vec{q}\cdot\vec{r}_i(t)\rangle} e^{-i\omega t} dt. \qquad (3.12)$$

Its correspond to the Fourier transform of the magnetic pair correlation function that gives the probability to find a magnetic moment at the position r_j at the time t. Therefore, the magnetic cross section depends on magnetic as well as on vibrational degrees of freedom.

Generalized Spin Susceptibility

The magnetic scattering function is also directly related to the imaginary part ($\Im$) of the wave-vector and frequency dependent susceptibility $\chi^{\alpha\beta}(\vec{q}, \omega)$ via the fluctuation-dissipation theorem by:

$$S^{\alpha\beta}(\vec{q}, \omega) = \frac{\hbar}{\pi} \frac{1}{1 - e^{-\hbar\omega/k_B T}} \Im \chi^{\alpha\beta}(q, \omega). \qquad (3.13)$$

This theorem implies that the magnetic moment of the neutron acts on the sample as a frequency and wave-vector dependent magnetic field $\vec{B}(\vec{q},\omega)$, monitoring the response of the sample:

$$M_\alpha(q,\omega) = \sum_\beta \chi^{\alpha\beta}(\vec{q},\omega)\vec{B}_\beta(\vec{q},\omega), \tag{3.14}$$

where $\chi^{\alpha\beta}(\vec{q},\omega)$ is the generalized susceptibility tensor. The fluctuation-dissipation theorem allows the direct comparison of $\chi^{\alpha\beta}$ as obtained by neutron scattering with bulk measurement of χ.
The magnetic scattering cross-section can therefore probe the magnetic response function of a system. Neutron scattering is a resonance technique and therefore the quantity measured is the response function $S(\vec{q},\omega)$ for modes of the system with scattering vector $\vec{q}$ and frequency ω. The fluctuation-dissipation theorem $S(\vec{q},\omega)$ is related to the fluctuations of the system in thermal equilibrium: this is exactly the properties of interest for the study of phase transitions. In the case multiple scattering is neglected, one obtains the Fourier-transformed pair correlation function $S_0^\alpha(0)S_R^\beta(t)$ between the components α and β of spins at position R and in time t.

Bragg Scattering

For a system with long-range magnetic order, the magnetic moments of the unpaired electrons align spontaneously. Such materials behave as if small magnetic moments were located at each atomic site with all the moments ordered in space. These moments give rise to Bragg diffraction of neutrons. The expression of the differential cross-section can be derived for magnetic Bragg scattering [37]

$$\left(\frac{d\sigma}{d\Omega}\right)_{Bragg} = N\frac{(2\pi)^3}{v_0}\sum_\tau(\delta(\vec{q}-\vec{\tau})|F_M(\vec{q})|^2 \tag{3.15}$$

where

$$|F_M(\vec{q})|^2 = \left(\gamma r_0 \frac{g}{2}\langle S\rangle f(\vec{q})\exp^{-W}\right)^2\left(1-(\vec{q}\cdot\vec{S})^2\right) \tag{3.16}$$

This expression shows that the magnetic Bragg peaks coincides with the nuclear Bragg peaks for ferromagnets. For a multi-domain sample the averaging process leads to $\langle 1-(\vec{q}\cdot\vec{S})^2\rangle = 2/3$.

In magnetic structures like incommensurate helical magnets, the magnetic Bragg peaks appear as satellites that are displaced from the nuclear Bragg peaks by the modulation wave-vector $\vec{k}$ that defines the periodicity of the arrangement of the moments, i.e. peaks appear at positions $\vec{q} = \vec{\tau} \pm \vec{k}$. The displacement of the satellite peaks from the nuclear peaks can be used to determine both the direction of the helical axis and the magnitude of the turn angle between successive helical planes.

The major difference between the nuclear and magnetic cross section is the vectorial dependence of the magnetic scattering on the relative orientation between $\vec{q}$ and the direction of the magnetic magnetic moments allowing often a distinction between the nuclear and magnetic scattering contributions without using polarization analysis.

Scattering from a Helical Structure

Blume [39] was the first to discuss the cross section for polarized neutrons scattering from a helical spin structure. We present here the essential part of the results from Ref. [39] as they are related to this work. The polarized neutron cross section of the helical magnetic structure is given by

$$\frac{d\sigma}{d\Omega} = \frac{1}{4} N \frac{(2\pi)^3}{v_0} \left(\frac{\gamma e^2}{m_e c^2} \right)^2 S_0^2 |F(\vec{k})|^2 [f_+(P)\delta(\vec{k}+\vec{q}-\vec{\tau}) + f_-(P)\delta(\vec{k}-\vec{q}-\vec{\tau})] \quad (3.17)$$

where $\vec{k}$ is the scattering vector, $\vec{\tau}$ is the reciprocal lattice vector which is zero (000) in the case of small angle scattering. $F(k)$ is the magnetic form factor and the factors $f_\pm(P)$ are written as

$$f_\pm(P) = 1 + (\hat{e_k} \cdot \hat{e_z})^2 \pm 2(\vec{P} \cdot \hat{e_k})(\hat{e_k} \cdot \hat{e_z}) \quad (3.18)$$

where $\hat{e_k}$ and $\hat{e_z}$ represent the unit vectors in the direction of $\vec{k}$ and $\vec{q}$ respectively, and $\vec{P}$ is the polarization vector of the neutrons. According to Eq. 2.33, the vector $\vec{q}$ is parallel to $\hat{e_z}$ in the case of the right-handed spiral, while $\vec{q}$ is antiparallel to $\hat{e_z}$ in the case of the left-handed spiral.
As a result from Eqs. 2.33 and 3.17, the helical structure scatters according to the handedness of the system either spin-up or spin-down neutrons under experimental conditions of $\hat{e_k} \parallel \hat{e_z}$ and $\vec{P} \parallel \pm\hat{e_k}$. In small angle polarized neutron scattering experiments the following selection rule gives the chirality of the magnetic structure: (1) if $\vec{P} \parallel -\vec{k}$ scattering from a right-handed spiral is allowed and $\vec{P} \parallel \vec{k}$ is forbidden. (2) if $\vec{P} \parallel \vec{k}$ scattering from a left-handed spiral is allowed while $\vec{P} \parallel -\vec{k}$ is forbidden.

Neutron Cross Section from Paramagnetic Fluctuations

In the approximations made in the calculations in Sec.2.4, the scattering of polarized neutrons from a magnetic helix above T_c is given by [31, 40]

$$\frac{d\sigma}{d\Omega} = [rF(k)]^2 \frac{T}{J[(q+k)^2+\kappa^2]} \frac{k^2+q^2+\kappa^2+2kqP_0}{(q-k)^2+\kappa^2+k^2U(\hat{q}_x^4+\hat{q}_y^4+\hat{q}_z^4-1/3)} \quad (3.19)$$

where $r = 5.410 \times 10^{-13}$ cm, $F(k)$ is the magnetic form factor of the unit cell, P_0 is the neutron polarization and we have taken into account for MnSi that D_m is negative ($k = |D_m|/J$ see Sec. 2.4), as the helix is the left-handed [33]. κ is the inverse correlation length of the spin fluctuations, and $\vec{q}$ is the scattering vector with the coordinates q_x, q_y and q_z. $U = |A_m|/2J$. The remarkable features of this expression are

(i) This function has a singularity at $q = \kappa$. For non-polarized neutrons ($P_0 = 0$) this singularity itself has no preference direction in $\vec{q}$ and therefore the scattering intensity $d\sigma/d\Omega$ forms the ring around $q = 0$ with the radius κ and the width of the ring is of order of κ.

(ii) For polarized neutrons ($P_0 \approx 1$), the scattering intensity depends on the mutual orientation of the vectors $\vec{q}$ and P_0. In case $\vec{P_0} \parallel \vec{q}$, the scattering is maximal and

is equal to $[rF(q)]^2(T/J)(1/\kappa^2)$ at $q = \kappa$. The singularity disappears and the scattering intensity is minimal. Thus for polarized neutrons the scattering looks as a half of the ring with maximal intensity at $\vec{P}_0 \parallel \vec{q}$.

It is convenient to determined the so-called polarization of the scattering as [41]

$$P_s = \frac{\sigma(P_0) - \sigma(-P_0)}{\sigma(P_0) + \sigma(-P_0)} = -\frac{2kqP_0 \cos\Phi}{q^2 + k^2 + \kappa^2}. \tag{3.20}$$

It should be noted that the last two features were mentioned by Brazovskii [42], who predicted for MnSi the first order transition if one neglects the anisotropic exchange interaction.

3.3 Magnetic Scattering by Small Angle Neutron Scattering

Small angle neutron scattering (SANS) is known as a suitable technique for studying density- and concentration fluctuations on a length scale between $0.5\,\text{nm}$ and $300\,\text{nm}$ which corresponds to typical sizes of micro-structural features in nanoscaled materials [43]. In addition magnetic fluctuations in domain like structures can be monitored by SANS.
The concept and experimental set-up for SANS is very simple and schematically shown in Fig. 3.5.

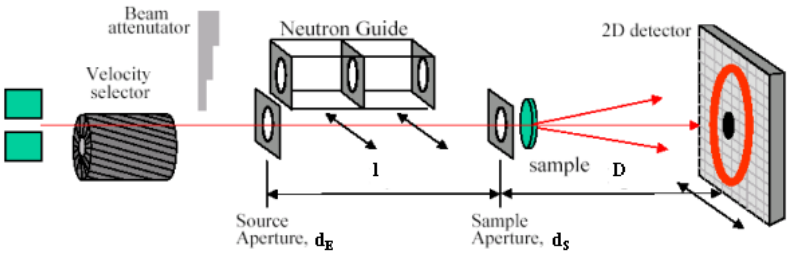

Figure 3.5: Basic schematic of a traditional SANS instrument.

From the white neutron beam produced by a reactor a small band of wavelengths $\Delta\lambda$ is selected, collimated and directed to the sample. The scattered neutrons are counted by a position sensitive detector whereas the transmitted beam is absorbed in a beam stop. The Fourier transform of the intensity distribution $I(q)$ as function of the scattering vector q gives access to the correlation function in real space i.e to size, composition and magnetization of the sample. Small angle neutron scattering is a special regime of small q-values between $10^{-2}\,\text{nm}^{-1}$ and $5\,\text{nm}^{-1}$ which allows to investigate fluctuations on a length scale $d \propto 2\pi/q$ ranging from $1\,\text{nm}$ to $500\,\text{nm}$.
Elastic scattering of neutrons with wavelength λ leads to a momentum transfer Q according to

$$Q = \frac{4\pi}{\lambda}\sin\theta \tag{3.21}$$

where 2θ is the scattering angle.

3.3.1 Conventional Approach to Critical Exponents

Conventionally critical magnetic scattering is explored by a triple axis spectrometer. However in this thesis we present results of magnetic SANS experiments as an alternative "poor-man" method to study the critical spin fluctuations.
As shown in Fig. 3.6 the triple axis instrument is composed of three main parts. First Axis: The incoming neutrons with a wave-vector $|\vec{k_i}| = 2\pi/\lambda_i$ are selected out of the white neutron beam according to Bragg's law ($2d \cdot \sin\theta = n \cdot \lambda_i$) via reflection from a monochromator crystal (e.g. pyrolytic graphite or copper).
Second Axis: The selected neutron is scattered from the sample into a solid angle $d\Omega$.
Third Axis: The scattered neutrons with a wave-vector $\vec{k_f}$ are analyzed via Bragg-reflection from an analyzer. Finally the neutrons are counted by a detector. In most cases a ^{3}He detector is used.

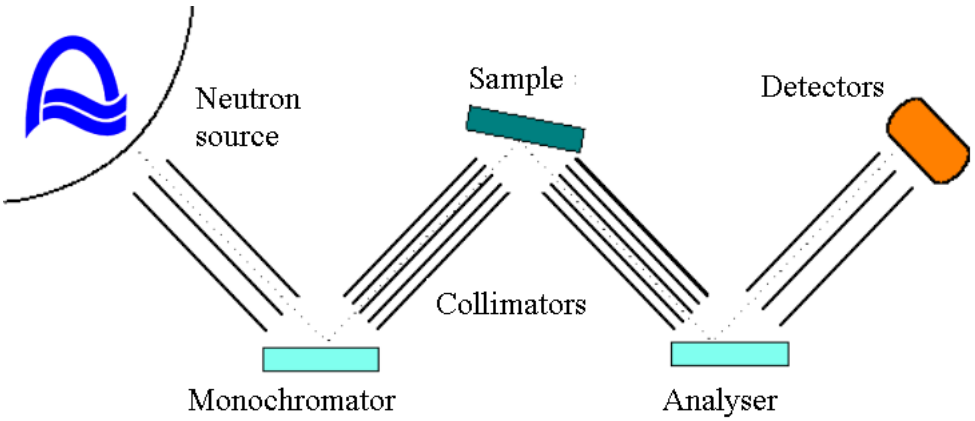

Figure 3.6: Schematic view of a three-axis spectrometer. The three axis consist of (i) monochromator (ii) sample and (iii) analyzer.

The particular advantage of the triple axis spectrometer is that it can performe scans in energy at a chosen fixed momentum transfer Q (constant-Q method) or scans in wave vector at chosen fixed energy transfer E (constant-E method) or even scans in which both Q and E vary in a predetermined manner. Thus precise information can be obtained on the details of the scattering function $S(Q,\omega)$. The scattering geometry in triple axis experiment in the reciprocal space is shown in Fig. 3.7
The main disadvantage of the triple axis spectrometer is also a result of this selectivity in measurement. Only one position in (Q,E)-space is explored at a time and since the solid angle subtended is relatively small. The final detected signal is therefore often low and long measurement times are required. On the other hand, due to the collimators used to define the neutron flight paths and the possibility of shielding efficiently the detector, the background count rate is also low. In Sec. 3.3.2 an alternative method is presented and improved for investigation of magnetic fluctuations around the transition temperature of magnetic systems.

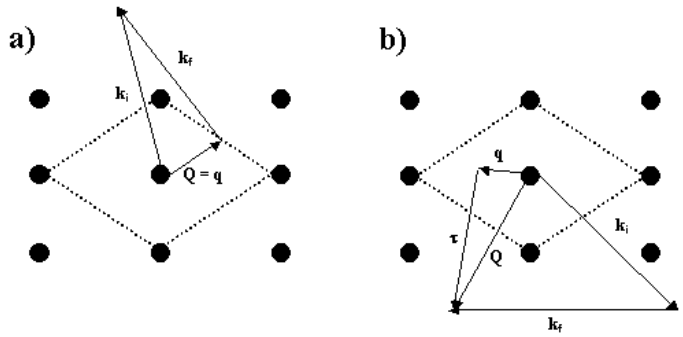

Figure 3.7: (a) Scheme of an elastic scattering process (Bragg scattering) $|\vec{k}_i| = |\vec{k}_f|$. (b) For inelastic scattering $|\vec{k}_i| \neq |\vec{k}_f|$. The scattering vector $\vec{Q}$ is decomposed into a reciprocal lattice vector $\vec{\tau}$ and the wave-vector $\vec{q}$ of the excitation that is analyzed. The dashed boxes mark the boundaries of the first Brillouin zone and the black circles the sites of the reciprocal lattice.

3.3.2 The Inclined Geometry in Small Angle Neutron Scattering

By means of small-angle neutron scattering with polarized neutrons one can extract valuable informations about the magnetic fluctuations. Apart from the well-known triple-axis spectrometer some other method has been applied which does not require energy transfer analysis. In the so called inclined geometry, the applied magnetic field at the sample position is inclined relative to the primary beam by the angle $\phi \neq \pi/2$ [44].

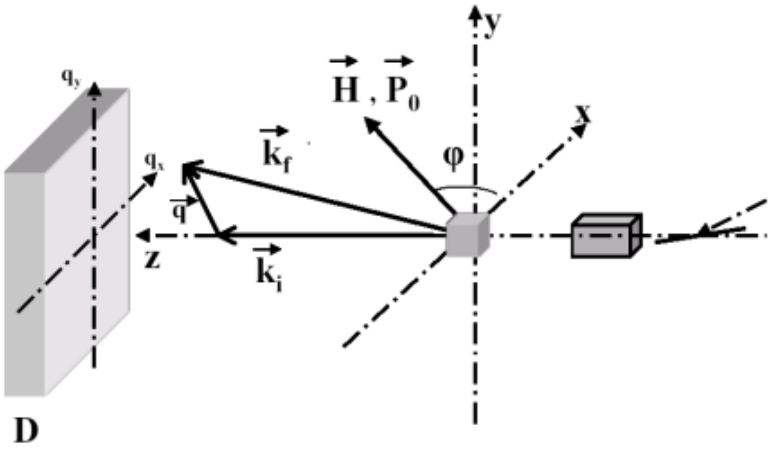

Figure 3.8: Basic schematic of SANS in the so called inclined geometry.

In magnetic systems nontrivial high-order spin correlations can persist. Particularly there are three or four-spin (in the presence of the Dzyaloshinskii-Moriya interaction) chiral fluctuations which should be strongly enhanced in the critical region near the second order phase transition [29, 45]. Details on the theoretical study of this method were presented in [46]. Here we present an overview of this method.

As shown in Sec. 3.2.2, the magnetic scattering is determined by the pair correlation function that is directly related to the imaginary part of the wavelength dependent sus-

ceptibility $\chi(\vec{q},\omega)$. In zero magnetic field $\chi(\vec{q},\omega)$ the neutron scattering intensity does not depend on the neutron polarization. In a magnetic field $\vec{B}$, the tensor $\chi(\vec{q},\omega)$ attains antisymmetric parts. If $\vec{B}$ is along the z direction we have $\langle S_x S_y\rangle \neq \langle S_y S_x\rangle$ and the cross section depends on the initial polarization of incident neutrons P_0. In small field $\vec{B}$, the antisymmetric part is proportional to $\vec{B}$ and is determined by the three spin ($\langle[S_x \times S_y]S_z\rangle$) correlation function. This chiral part of the neutron scattering gives rise to three-spin interaction. Indeed the transverse component of the spin in ferromagnets saturated in z direction, are always related to the excitations.

For small angle scattering the chiral cross section has the following form [41]:

$$\sigma_{chiral}(\vec{q},\omega) = (\frac{2r^2 P_0 T}{\pi\omega})(\vec{q}\cdot\vec{B})^2 \Im C(\vec{q},\omega), \tag{3.22}$$

In this expression we have taken into account that both the dynamical chirality $C(\vec{q},\omega)$ and the polarization P_0 are directed along the field $\vec{B}$.
In small angle neutron scattering experiment elastic components of magnetization perpendicular to the incident wave vector k_i are visible in the detector: $q_\perp = k_i(\theta_x + \theta_y)$, where θ_x and θ_y are the scattering angles in the x and y-direction, respectively. Inelastic contributions to the scattering process cannot be detected: $q_\| = k_i\omega/2E$. Thus, no energy analysis is performed in a conventional SANS experiment but integration over the energy is automatically performed. Therefore in theory Eq. 3.22 has to be integrated over all energies of the scattered neutrons. Recalling that $\Im C(q,\omega)$ is an even function of ω, the integrated chiral cross section becomes zero if there is no ω-odd term in the factor $(\vec{q}\cdot\vec{B})^2$ of Eq. 3.22. Such an ω-odd term appears if $\vec{B}$ is inclined with respect to the incident beam at an angle ϕ as shown in Fig 3.8. Then, for the inclined field, we have

$$(\vec{q}\cdot\vec{B})^2 = \frac{(2E\theta)^2\cos^2\phi + \omega^2\sin^2\phi + 2E\theta\omega\sin 2\phi}{(2E\theta)^2+\omega^2} \tag{3.23}$$

Obviously, only the third part is ω odd. Hence, the ω-integrated chiral cross section is given by

$$\sigma_{chiral}(\theta) = \frac{2}{\pi} r^2 P_0 T \sin 2\phi \int_{-\infty}^{+\infty} \frac{2E\theta \Im C(q,\omega)}{(2E\theta)^2+\omega^2} d\omega. \tag{3.24}$$

This integral can be evaluated in the critical paramagnetic region $T > T_C$. According to scaling theory all physical parameters have a scaling dimensionality determining the general form of the corresponding correlation function. For example the pair correlation function has the form [29]

$$G(q) = \frac{1}{(\kappa a)^{2-\eta}} f(\frac{q}{\kappa}) \approx \frac{1}{a^2(q^2+\kappa^2)}, \tag{3.25}$$

where κ is the inverse correlation length of the critical fluctuations defined as $\kappa = \tau^\nu/a$. Here, $\tau = |T - T_c|/T_c$ is a reduced temperature. $\nu \approx 2/3$ is the critical exponent of the correlation length and a is a length scale of order of the lattice spacing. The Ornstein-Zernicke relation on the right-hand side of Eq. 3.25 is valid for $\eta \ll 1$. This is the case for the three dimensional spin systems. Therefore, we will neglect η below.

In a magnetic field, we have to compare the energy of the magnetic field $g\mu_B B$ with the energy of the critical fluctuations $k_B T_c(\kappa a)^{5/2}$ in order to determine the condition for the weak-field $h \ll 1$ and strong field regime $h \gg 1$, respectively, where $h = g\mu_B B/k_B T_C(\kappa a)^{5/2}$ is a dimensionless number.

In a weak field the chiral scattering is proportional to $\vec{B}$. Therefore the dimensionality is determined by the product $hg(q)$ and following expression is obtaines in the case of ferromagnets [47]

$$\Im C(\vec{q},\omega) = \frac{g\mu_B B}{k_B T_c(\kappa a)^{9/2}} f[\frac{q}{\kappa}, \frac{\omega}{\Omega(q)}], \tag{3.26}$$

where $\Omega(q) = k_B T_c(qa)^{5/2}$ is the characteristic energy of the critical fluctuations with scattering vector $\vec{q}$.

The dynamical chirality or induced chirality is a three spin correlation function and it may be considered as a result of the scattering of critical fluctuation on the uniform magnetic field [29]. From this point of view it is clear that $C(q)$ is a function of two momenta, namely the momentum of the fluctuation q and the momentum of the field $q_B = 0$. The principle of critical factorization was formulated by Polyakov [48, 49, 50] and is known as Polyakov-Kadanov-Wilson operator algebra. It states that in any multi-spin correlation function, the dependence on the largest momentum q ($q \gg \kappa$) appears as a factor $(q/\kappa)^{-5+1/\nu}\Phi[\omega/\Omega(q)]$. In our case, putting $\nu = 2/3$ we obtain

$$\Im C(q,\omega) = \frac{g\mu_B B}{T_C(qa)^{7/2}(\kappa a)} \Phi[\frac{\omega}{\Omega(q)}]. \tag{3.27}$$

In this expression we have $q = k_i[\theta^2 + (\omega/2E)^2]^{1/2}$. The dependence of q on ω may be neglected in the quasi-elastic approximation, if the residence time of the neutron in a region of the size of the order of $1/q$ is much smaller than the characteristic lifetime of the fluctuation of the same size $\hbar/\Omega(q)$. The corresponding condition can be expressed as

$$q \ll q_{in} = \frac{(2E/k_B T_C \kappa a)^{2/3}}{a}. \tag{3.28}$$

Hence we can replace q by $k_i\theta$ and neglect ω in the denominator of Eq 3.24. Therefore, the chiral cross section becomes

$$\sigma_{chiral}(\theta) = \frac{2}{\pi} r^2 P_0 \sin 2\phi \frac{g\mu_B B}{2E(\kappa a)\theta^2} \frac{1}{\kappa a} \mathrm{sgn}\theta. \tag{3.29}$$

Often, it is convenient to normalize Eq. 3.29 by the symmetric cross section $\sigma(\theta) = (2/3)r^2 G(Q)$ and one obtains

$$\sigma = \frac{\sigma_{chiral}(\theta)}{\sigma(\theta)} = A P_0 \sin 2\phi \frac{g\mu_B}{B\kappa} \mathrm{sgn}(\theta). \tag{3.30}$$

Here A is a constant of the order of unity. We will use Eq. 3.30 for analyzing our experimental results from the isotropic ferromagnet EuS.

3.4 Instrumental Aspects

The Available q-range of the Instruments

The momentum transfer $Q = 4\pi/\lambda \sin\theta$, where 2θ is the scattering angle and λ the neutron wavelength at a given point on the detector is given by

$$Q(r) = \frac{4\pi}{\lambda} \sin\left(\frac{1}{2}\arctan(r/D)\right) \tag{3.31}$$

where r is the radial distance of the point on the detector from the beam axis and D the sample-to-detector distance. Since the wavelength range at sample position is $3\text{Å} \leq \lambda \leq 20\,\text{Å}$ for SANS-2, the calculated range of momentum is $0.01\,\text{nm}^{-1} \leq Q \leq 3\,\text{nm}^{-1}$.

Instrumental Resolution

In this work a very simple approximations for the experimental resolution has been used and is briefly described below. We assume a Gaussian distribution for each component as generally done for calculations in spectrometer resolution [43]. Fig. 3.9 display a schematical view of the beam geometry and the set-up used to calculated the instrumental resolution.

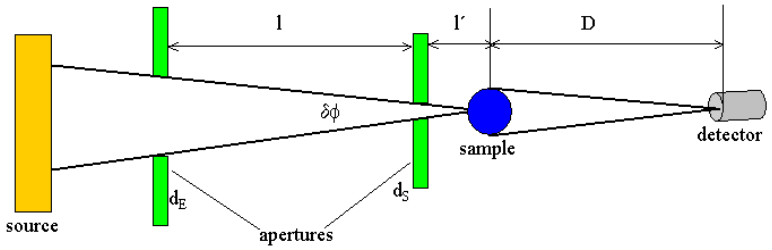

Figure 3.9: Simplified view of beam geometry for a typical SANS experiment with pin-hole apertures. The instrumental resolution is determined by the configuration of the apertures.

The radial and longitudinal resolution has two contributions. One from the angular collimation of the neutron beam and one from the wavelength spread of the neutrons. The azimuthal resolution is only affected by the collimation. The total resolution is then determined by a superposition of angular divergence contribution due to the size of the entrance slit d_E, the sample slit d_s and their distance l, the contribution from the wavelength spread $\Delta\lambda$ and of detector resolution. An approximation for the total FWHM called $[\Delta(2\theta)]_{tot}$ is written as

$$[\Delta(2\theta)]_{tot} \approx \left([\Delta(2\theta)]^2_{\lambda} + [\Delta(2\theta)]^2_{colli} + [\Delta(2\theta)]^2_{det}\right)^{1/2} \tag{3.32}$$

where $[\Delta(2\theta)]_{\lambda} = 2\theta \cdot (\Delta\lambda/\lambda)$ is the contribution to the resolution due to the wavelength distribution. The collimation resolution is $[\Delta(2\theta)]_{colli} = \frac{1}{l}(d_e^2 + d_s^2)^{1/2}$.
The scattered neutrons are counted by the 2-dimensional position sensitive detector (PSD) into $0.7 \times 0.7\,\text{cm}^2$ pixels which correspond to the spatial resolution of the detector given as $[\Delta(2\theta)]_{det} = d_{eff}/D$ with $d_{eff} = 2D\tan(\Delta(2\theta)/2)/\cos^2(2\theta)$. This resolution is

better than the size of the Bragg peak produced by the collimation and therefore can be neglected in the calculations of the in plan resolution [43].

The q-resolution in the three directions is now given as follow

$$\Delta q_{rad} = \left(\frac{2\pi}{\lambda}[\Delta(2\theta)]_{\lambda}\right)^2 + \left(\frac{2\pi}{\lambda}[\Delta(2\theta)]_{colli}\right)^2 \quad (3.33)$$

$$\Delta q_{azim} = \left(\frac{2\pi}{\lambda}[\Delta(2\theta)]_{colli}\right)^2 \quad (3.34)$$

$$\Delta q_{long} = (q[\Delta(2\theta)]_{\lambda})^2 + (q[\Delta(2\theta)]_{colli})^2 . \quad (3.35)$$

These equations were used to calculated the instrument resolution of the SANS-2 instrument as well as of the instrument MIRA.
For SANS-2 experiments we achieve a configuration given in all directions a q-resolution $\Delta q/q = 12\%$. This is a required value to resolve the magnetic helix expected at $q = 0.035\,\text{Å}^{-1}$ and to detect the wave vector rotation occuring in MnSi.
The q resolution for the instrument MIRA was different in radial, longitudinal and azimuthal directions due to the different beam divergence in these directions resulting from the apertures and the rectangular shape of the neutron guide. The instrument was configured in such a way that a radial resolution of $\Delta q/q = 11\%$, a longitudinal resolution of $\Delta q/q = 27\%$ and an azimuthal resolution of $\Delta q/q = 10\%$ could be achieved.

3.4.1 The SANS-2 Diffractometer at FRG-1 Reactor of the GKSS

The measurement of microscopic properties have been carried out partially on the SANS-2 instrument of the GKSS Forschungszentrum in Geesthacht.
This instrument is designed to be used for scattering experiments with polarized neutrons. The principle layout is illustrated schematically in Fig. 3.10.
SANS-2 is installed at a cold neutron guide, which is curved to filter out epithermal and higher energy neutrons. It uses in its basic configuration a mechanical velocity selector for monochromatisation. The standard wavelength spread is $\Delta\lambda/\lambda = 10\%$ (FWHM); by tilting the selector relative to the neutron beam direction this value can be decreased to 8% or increased up to 20.6%. A straight pin-hole collimation is used to tail the primary beam. Behind the sample, in the secondary flight path, a two dimensional sensitive detector is used to register the neutrons scattered around the primary beam. The detector is placed into a vacuum chamber to reduced the background. The detector can be moved up to $20\,\text{m}$ behind the sample position. In this concept the covered q-range is a linear function of the selected average neutron wavelength and sample-detector distance. Further the resolution is a linear function of the wavelength spread, the collimation angle and the size of the detection elements. These simple relations fulfill the condition of a straight-forward choice of the appropriate instrument configuration.

Sample Environment

SANS-2 is equiped with a flexible sample environment. The experiment was carried out with a conventional electromagnet of a maximal horizontal field of $800\,\text{mT}$. A cryostat

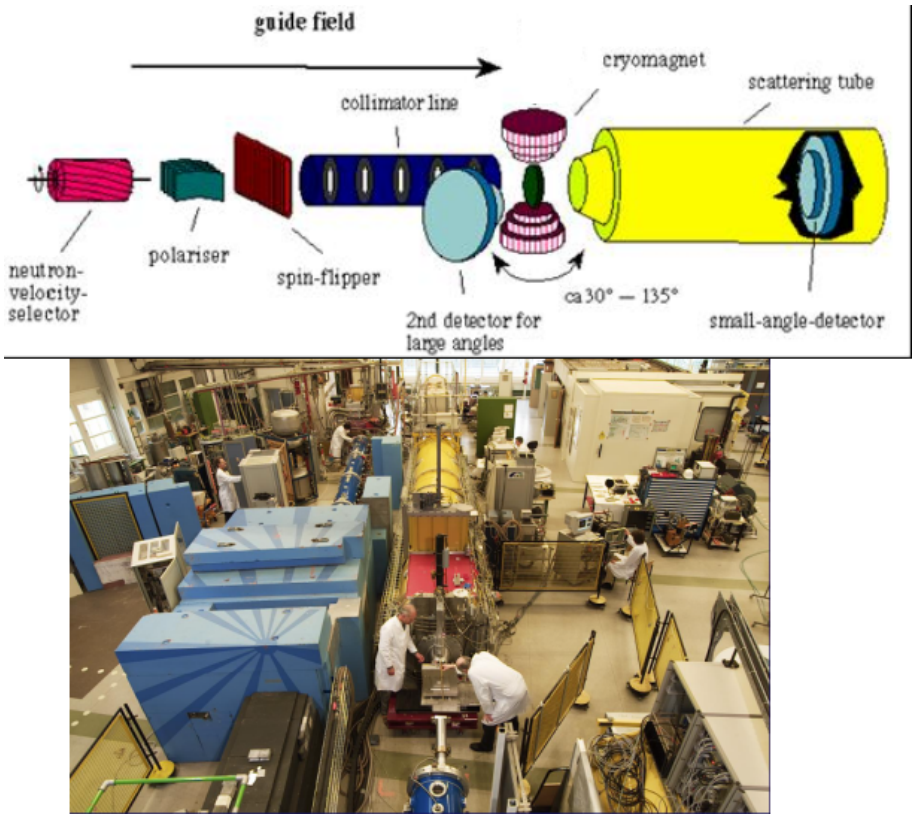

Figure 3.10: Basic schematic view and picture of small-angle neutron scattering instrument SANS-2 at FRG-1 (GKSS) Geesthacht. The electromagnet is mounted in such a way that the applied magnetic field was horizontal.

offers the possibility to drive the temperature down to $8\,\mathrm{K}$. The sample was mounted in vacuum and insulation shields, in order to reduce the small angle background, that otherwise arise from passing the neutron beam through isolation shilds made of aluminum.
The flux of polarized neutrons at the sample position is 2^7 n.cm^{-2}.s^{-1} for a wavelength of $0.58\,\mathrm{nm}$. A goniometer for sample alignment was not available. It was difficult to adjust the single crystal in a proper way. Therefore we performed further experiements at the new neutron facility in Munich on the instrument MIRA.

3.4.2 The Double Axis Diffractometer MIRA at FRM-2

Fig. 3.11 shows a basic schematic of the instrument MIRA. It is a versatile instrument for very cold neutrons (VCN) with wavelength of $8\,\text{Å}$ and above. It is situated at the cold neutron guide NL6b in the neutron guide hall of the FRM-II.
The instrument consists of a $6\,\mathrm{m}$-curved ($R = 84\,\mathrm{m}$) ^{58}Ni neutron guide with a cross section of $1\,\mathrm{cm} \times 12\,\mathrm{cm}$ resulting in a limiting wavelength for the guide of about $8\,\text{Å}$. The upper and lower face are coated with supermirrors $m = 2$.
At the end of the guide the monochromator mechanics is situated inside a round shielding. Currently an $m = 4.3$ multilayer monochromator allows to choose a wavelength between $8\,\text{Å}$ and $30\,\text{Å}$. After monochromatisation the neutrons enter a vacuum tube and

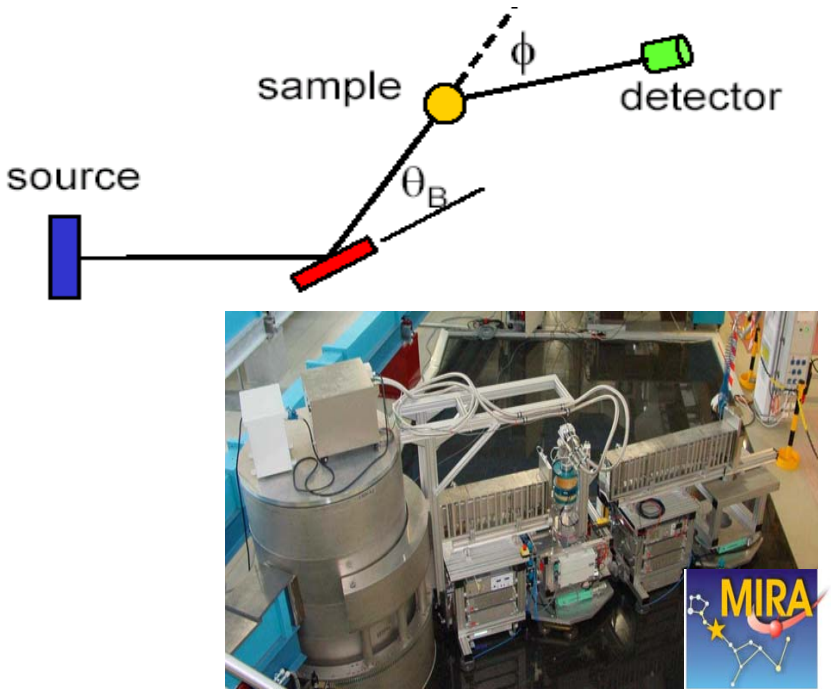

Figure 3.11: Basic schematic view and picture of the instrument MIRA at FRM-2.

are scattered on the sample. The reflection geometry used is vertical, thus the sample table performs a 2θ scan. Furthermore it is equipped with a full goniometer for sample orientation. The scattered neutrons are counted using a 2-dimensional position sensitive detector. The detector is put inside a shielding chamber that is not evacuated as in the SANS-2 instrument. Therefore the background is expected to be larger than on the SANS-2. A slit system of 4 apertures before and behind the monochromator and the sample position is used to choose a particular q-resolution. All moving parts, the detectors and in a later stage also the polarizers are fully automated in order to control the experiment by a computer. The whole instrument has a 60 Gauss guide field of permanent magnets for polarized neutrons. Multilayer polarizers are used for polarizing and analyzing the neutron spins with respect to the magnetic guide field. More details on the instrument parameters of MIRA are available in [51].

Chapter 4

Induced Magnetic Chirality in EuS

Natur is just enough, but men and women must comprehend and accept her suggestions.
Antoinette Brown Blackwell

4.1 Introduction

EuS belongs to the most intensively investigated ferromagnets. Its simple fcc structure and weak anisotropy permit description of its magnetism within the isotropic Heisenberg model. Therefore it is interesting to study the behaviour of a typical Heisenberg system such as EuS for three reasons. (1) It is possible to induce the magnetic chirality be applying a magnetic field. Two and three-spin correlations can be studied in the critical temperature region. (2) There are competing exchange interactions $J_1 > 0$ and $J_2 < 0$. The ratio of J_1/J_2, which is of particular interest for understanding the magnetic phase diagram of spin glass system like $Eu_xSr_{1-x}S$ is found to be $J_1/J_2 = -2.2 \pm 0.1$ which is, in fact, close to the value -2 used in most theoretical works [52]. (3) The magnitude of the exchange interactions is comparable to the dipolar interactions. They are expected to influence the spin fluctuations of the system.
Traditionally magnetic fluctuations are studied by triple axis spectroscopy. In this thesis we use small angle neutron scattering to investigate the magnetic critical fluctuations of the localized ferromagnet EuS. We study the effect of the induced chirality also called dynamical chirality on the critical spin fluctuations in EuS using the pair correlation and the three-spin correlation function. Both functions can be measured with small-angle scattering of polarized neutrons in the inclined experimental geometry of the magnetic field. Both contributions are studied as a function of temperature and magnetic field. Firstly, we studied the critical scaling behavior of the pair correlation function. The temperature dependence of the correlation length in zero field obeys the scaling law $\xi \sim \tau^{\nu}$, where $\nu = 0.68 \pm 0.02$ in agreement with previous studies [45]. From experiments in a magnetic field at $q < q_d = 0.23\,\text{Å}$ and T close to $T_C = 16.5\,\text{K}$ we obtained the dynamic critical exponent $z = 2.1 \pm 0.1$, which is in agreement with the theoretically predicted value $z = 2$. The results of our study of the pair correlation function are in good agreement with those obtained previously [53, 49, 50]. On this basis the scattering intensity due to

the three spin correlation (induced chirality) is studied. It is shown that in the limit of small fields the scattering increases with increasing external magnetic field, showing the scaling temperature behavior proportional to $\tau^{-\nu}$ with $\nu = 0.64 \pm 0.04$. These results are close to those reported in the Ref. [54].
The importance of studying the high-order correlation functions should be pointed out because in many cases the physical properties of a system are defined by interaction of numerous neighboring particles. As a consequence, not only the pair correlation functions but also many-point(three, four spins) correlation functions play fundamental roles in the description of statistical properties of such systems and are important for condensed matter research [49]. Numerous studies on this subject involved different theoretical considerations and computer simulations [50]. Comparison of our results with previous studies allow us to improve the method of SANS with inclined geometry by determining the critical exponents of EuS.

4.1.1 Crystal Structure and Magnetic Properties of EuS

EuS crystallizes in the fcc structure as shown in Fig. 4.1.1, the lattice parameter being $a = 5.95\,\text{Å}$ and the moments order below the Curie temperature $T_C = 16.5\,\text{K}$.

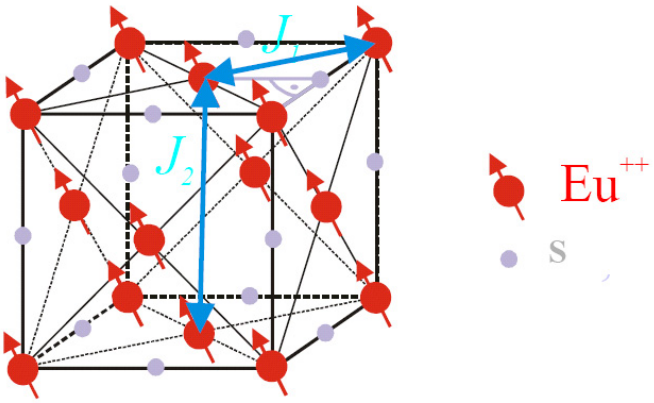

Figure 4.1: fcc crystal structure of EuS with a lattice constant $a = 5.973\,\text{Å}$. The large moment of Eu^{++} ions of $7\mu_B$ leads to strong dipolar interactions [55].

The magnetism is due to the well localized $4f$ electrons of the Eu^{2+}-ions. The easy axis of magnetization is the $\langle 111 \rangle$ crystallographic direction. The divalent europium forms an ${}^8S_{7/2}$ ground state with a stable moment of $7\mu_B$ (spin $S = 7/2$), as can be seen from spin-density measurements [56]. In EuS, because of the relatively weak exchange interaction and the low Curie temperature $T_c = 16.5\,\text{K}$, the dipolar interactions in the vicinity of the critical temperature have to be taken into account.

4.1.2 Previous Studies on EuS

The importance of the influence of the dipolar anisotropic interactions on the critical spin fluctuations of EuS has been demonstrated for the $q = 0$ susceptibility [57, 58] and by

neutron scattering [59, 53]. Along with theoretical work [60, 7] based on the mode coupling approach, these results led to an almost complete description of the important effect of the inevitable long-range dipolar interactions on the spin dynamics. The dynamic susceptibility of EuS has been investigates below T_C by Görlitz et al. [61]. They found that for internal magnetic fields larger than the anisotropy fields $H_A(T)$ of the compound, the static susceptibilites exhibit a $1/\sqrt{H}$-divergence which reveals quantitatively the dominance of dipolar-anisotropic spin-wave fluctuations, which is larger than the exchange interaction. This result shows the importance of the dipolar anisotropic fluctuations below T_C.

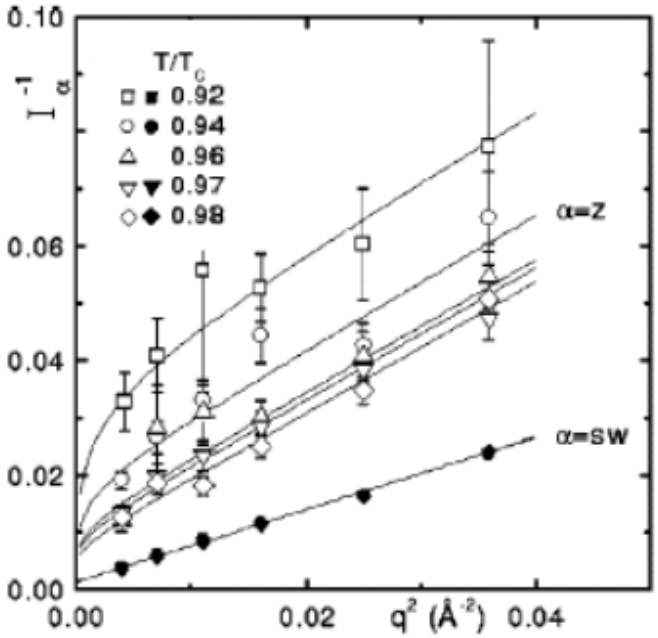

Figure 4.2: q^2 dependence of the inverse of the integrated intensities of the spin-wave and longitudinal spin fluctuations. Data are well described by the inverse static suscestibilities $\chi_{sw}^{-1} \sim [q^2+\kappa_g^2]$ ($\kappa_g = 0.04\,\text{Å}^{-1}$) and $\chi_z^{-1}(q \to 0) \sim [q^2 + \kappa^2]$. The susceptibility diverges as $1/q$ is at rather small q [55].

Above T_C the dipolar fields prevent the susceptibility of the long-wavelength longitudinal fluctuations from criticality. On the basis of theoretical and experimental studies it is known that the paramagnetic susceptibility is given by [62, 63]

$$\chi_p^i(q,T) = \frac{q_d^2}{\kappa^2(T) + q^2 + \delta_{i,L} q_d^2,} \tag{4.1}$$

where κ is the inverse correlation length for $T > T_C$. Eq. 4.1 defines a region of dipolar anisotropic behavior around the critical temperature($\kappa^2(T) + q^2 \leq q_d^2$) and shows that the longitudinal fluctuations ($i = L$) do not diverge. In contrast, the transverse fluctuations ($i = T$) diverge and are responsible for the phase transition at T_C. As a measure of the strength of the dipolar interactions one can define a dipolar wave number q_d that can be inferred from the inverse correlation length $\kappa(T)$ and the homogeneous internal susceptibility above T_C via the relation $q_d^2 = \chi(q = 0, T)\kappa^2$. There is a good agreement of

theoretical predictions and experimental value of the dipolar wave vector $q_d = 0.23\,\text{Å}^{-1}$. The theoretical prediction that magnetic fluctuations are still present at high temperature far above T_C is confirmed by experiments [64]. This is surprising since one would expect the lifetime of the spin fluctuations to be zero and the spin correlation to vanish.
In the dipolar critical regime, where the inverse correlation length and q are smaller than the dipolar wave number q_d, Böni et al. [55] show that the static susceptibility of the spin waves displays the Goldstone divergence while the longitudinal spin fluctuations follow the Ornstein-Zernicke expression giving a possible indication of a thermal mass renormalization at the smallest q values. They observed in agreement with predictions of the renormalization group theory [65] indications the $1/q$ divergence of the longitudinal susceptibility as illustrate in Fig. 4.2.
Under the assumption that the isotropic exchange interaction dominates the ordering process, the parameters defining the static properties of EuS in the critical temperature range agree well with the theoretical critical exponents presented on Tab. 2.1. The dynamic properties for systems with an isotropic exchange interaction are well interpreted in terms of the dynamic scaling hypothesis [66, 67].
The complication arises when the relativistic interactions, such as dipolar forces or anisotropic exchange interactions are considered. The dipolar forces should gain importance in the critical regime (see Fig. 2.1), where the inverse correlation length and the wave-vector are small compared to the dipolar wave number q_d. The effects of dipolar forces on the spin dynamics of Heisenberg ferromagnet have been taken fully into account in Ref. [47, 7]. An excellent agreement of the theory [60, 7] with experiments was obtained for the critical slowing down of the line width $\Gamma(q)$ observed for $q \to 0$ and $T \to T_C$ on the transverse fluctuations in Fe [68] and on the transverse and longitudinal fluctuations in EuS [53]. One important result of these studies is the crossover from $\Gamma(q > q_d) \sim q^{2.5}$ in the exchange-dominated regime to $\Gamma(q \ll q_d) \sim q^2$ in the dipolar regime.

4.2 Experimental Details

The isotopically enriched sample ^{153}EuS was assembled from approximately 100 small EuS crystals on a machined aluminum substrate. The $[100]$ axes of all crystals were aligned in one direction to within a precision of $0.75°$[55] as illustrated in Fig. 4.3.
The average size of a single crystal is $1 - 2\,\text{mm}^2$ and the square of the whole sample is $600\,\text{mm}^2$. Fig.4.4 shows a picture of the sample holder and the sample used for these studies.
The small angle polarized neutron scattering (SAPNS) experiments were performed using the SANS-2 instrument of the research reactor FRG-1 at the GKSS-Forschungszentrum in Geesthacht (Germany). The schematic outline of the experiment is given in Fig. 3.8. All measurement were conducted using polarized neutrons ($P_0 = 0.95$) of fixed wavelength $\lambda = 5.8\,\text{Å}(\Delta\lambda/\lambda = 0.1)$ with an angular divergence of $10\,\text{mrad}$. The scattered neutrons were counted in a q range 0.30 to $2.5\,\text{nm}^{-1}$. The scattering was measured in a temperature range $14\,\text{K} < T < 50\,\text{K}$, i.e, from below to far above T_C. The external magnetic field $1\,\text{mT} < B < 200\,\text{mT}$ was applied at an angle of $\phi = 45°$ with respect to the incident beam k_i (inclined geometry). The adiabatic condition for the transmission of polarized neutrons

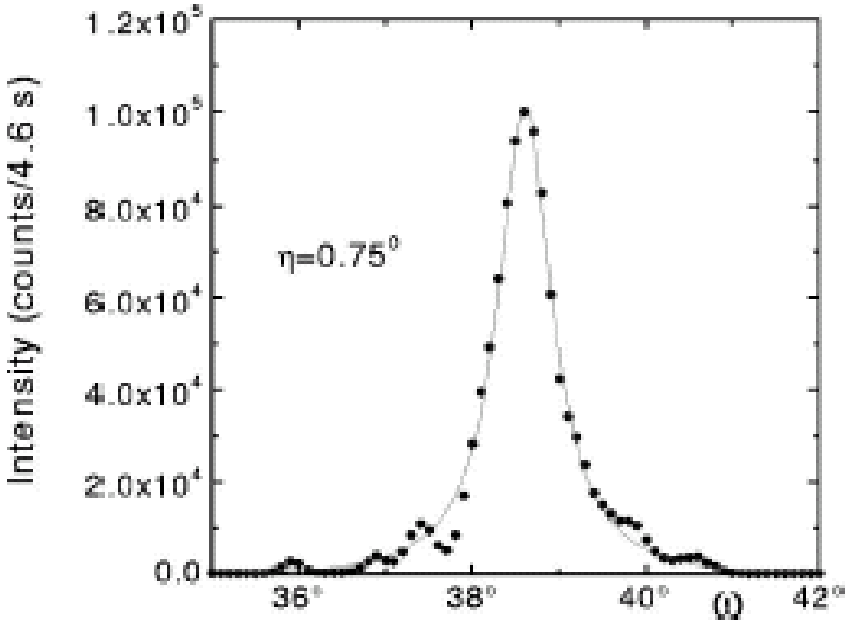

Figure 4.3: Rocking curve of the τ_{200} Bragg peak of the isotopically enriched sample. The overall mosaic is $\eta = 0.75^\circ \pm 0.02^\circ$.

was sufficiently satisfied to obey the relation $P_0 \parallel B$. Two scattering intensities $I^{\uparrow}(q)$ and $I^{\downarrow}(q)$ were measured for the incident neutron beam polarized along ($\uparrow$) and opposite ($\downarrow$) to the magnetic field.

The method of the inclined geometry allows to distinguish two contributions to the magnetic scattering: the symmetric polarization-independent (SPI) scattering and the asymmetric polarization-dependent (APD) scattering. First we separated the magnetic critical scattering from the nuclear contribution. Following the standard procedure we determined the pure magnetic scattering $I_m(q_\perp, T)$ by subtracting from the measured intensity the nonmagnetic background as measured at $T \gg T_C$

$$I_m(q_\perp, T) = I(q_\perp, T) - I(q_\perp, 50K). \tag{4.2}$$

Where $q_\perp$ is a projection of q onto the detector plane. In the following we will omit the subscript "$\perp$".

To separate the SPI term from the APD one, we take the sum of the measured intensities $I_\sum(q) = I_m(P_0, q) + I_m(-P_0, q)$ and average it over 2π for each $|\vec{q}| = \sqrt{q_x^2 + q_y^2}$. As a consequence, the asymmetric part is averaged out and only the SPI part survives. It is related to the pair correlation function. The polarization dependent part of the scattering $\Delta I(P_0, q) = I(P_0, q) - I(-P_0, q)$ is asymmetric. The asymmetry is directly related to the direction of the magnetic field $\vec{B}$. In the particular case of $\vec{B}$ being in the (xz) plane (see Fig. 3.8), the asymmetry is most pronounced along the x component of the momentum transfer q_x due to the selection rules. Thus the asymmetric contribution was extracted by taking the difference of the measured intensities $I(\pm P_0, \pm q_x)$

$$\Delta I(q) = \frac{1}{4}[I(P_0, q_x) - I(-P_0, q_x)] + \frac{1}{4}[I(-P_0, -q_x) - I(P_0, -q_x)]. \tag{4.3}$$

Figure 4.4: Picture showing the EuS sample and the sample holder used for SAPNS experiments.

For the analysis of the data, the SPI and the APD contributions were attributed to the pair correlation function and the induced chirality (three spin correlation) respectively.

4.3 Results of Experiments

The maps of scattering intensity at zero field for $T = 14\,\mathrm{K}$ for $T = 16.55\,\mathrm{K}$ and for $T = 60\,\mathrm{K}$ are shown on Fig. 4.5. The magnetic scattering is distributed on distances above $q = 0.3\,\mathrm{nm}^{-1}$ from the direct beam ($q = 0$). The intensity due to magnetic scattering increases as T_C approaches and is maximal at T_C. As the temperature increases the scattering intensitity is reduced considerably for $T = 60\,\mathrm{K}$ and is dissolved to the background at temperatures above $T = 60\,\mathrm{K}$. Data have been recorded for the polarization along (upper panel) and opposite (lower panel) to the incoming beam.
Fig. 4.6 displayed the q dependence of the pure magnetic intensity I_m at T_C. Clearly seen is the $1/q^2$ dependence (solid line) of the intensity at $B = 1.4\,\mathrm{mT}$.

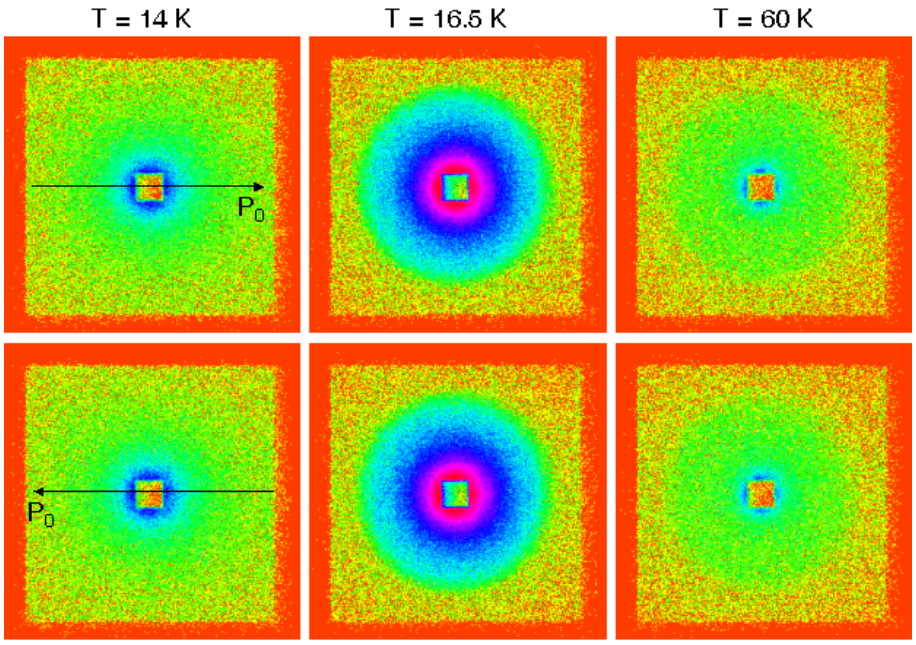

Figure 4.5: Maps of SANS intensity at $1.4\,\mathrm{mT}$ (guide field) and at temperatures $T = 14\,\mathrm{K}$, $T = 16.55\,\mathrm{K}$ and $T = 60\,\mathrm{K}$. Data have been recorded for the polarization along (upper panel) and opposite (lower panel) to the incomming beam.

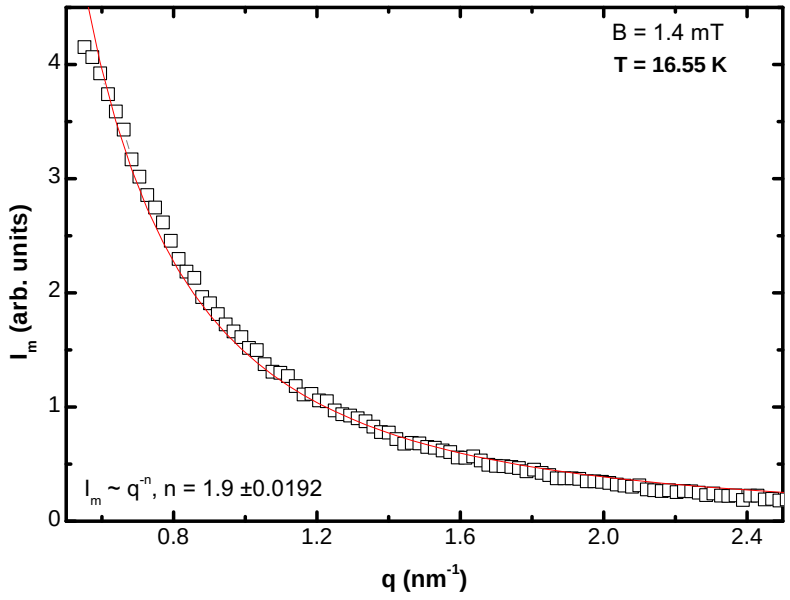

Figure 4.6: Pure magnetic scattering intensity as function of the scattering vector $\vec{q}$ for $T < T_C$ at zero magnetic field. The first two data points were neglected during the fitting procedure.

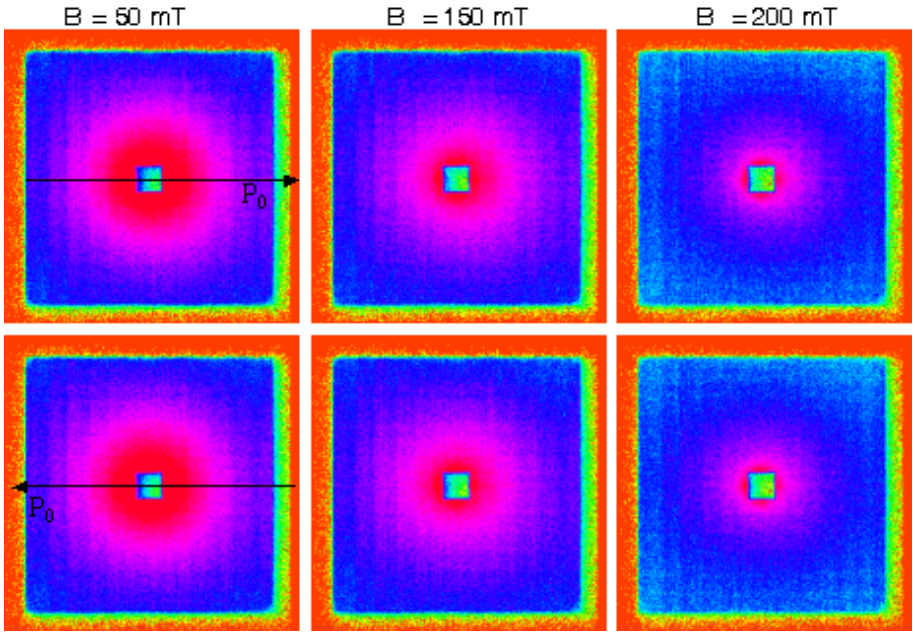

Figure 4.7: Maps of SANS intensity at $T = 16.55\,\mathrm{K}$ for different magnetic fields $B = 50\,\mathrm{mT}$, $B = 150\,\mathrm{mT}$ and $B = 200\,\mathrm{mT}$. Data have been recorded for the polarization along (upper panel) and opposite (lower panel) to the incomming beam.

The spectrum of SANS intensity as function of applied magnetic field at $T = 16.55\,\mathrm{K}$ is presented in Fig. 4.7 for $B = 50\,\mathrm{mT}, B = 150\,\mathrm{mT}$ and $B = 200\,\mathrm{mT}$. Data have been recorded for the polarization along (upper panel) and opposite (lower panel) to the incomming beam. The intensity decreases with increasing magnetic field and dissappears above $B = 200\,\mathrm{mT}$. At higher magnetic fields the intensity is decreased considerably at $B = 200\,\mathrm{mT}$ the maximal available field.
Fig.4.8 shows the temperature dependence of the magnetic intensity for two different momentum transfers. It is clearly seen that the intensity has a pronounced maximum at $T \sim T_C$. It is more pronounced for small q (for example $q = 0.5\,\mathrm{nm}^{-1}$) than for large q (for example $q = 1.5\,\mathrm{nm}^{-1}$).
This behavior demonstrates the appearance of critical fluctuations and an increase of the correlation length as T approaches T_C from low and high temperatures. The q dependence of the intensity I_m is treated in a standard way using the Ornstein-Zernicke expression

$$I_m(q) = \frac{Z_m}{q^2 + \kappa^2}, \tag{4.4}$$

where $\kappa = \xi^{-1}$ is the inverse correlation length. The parameters Z_m and κ have been obtained from the least-squares fit to the data using Eq. 4.4.
The temperature dependence of Z_m and κ are shown in Figs. 4.9 and 4.10 for $B = 1.4\,\mathrm{mT}$ and $B = 50.6\,\mathrm{mT}$ respectively. Z_m does not depend on the magnetic field in the whole temperature range except close to T_C.

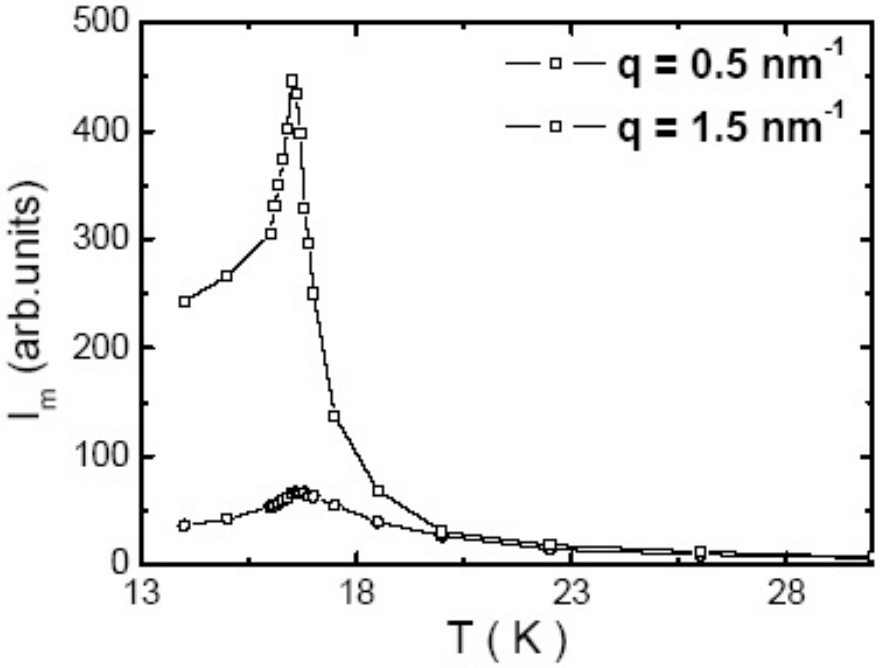

Figure 4.8: Temperature dependence of magnetic scattering intensity at a residual magnetic field $B = 1.4\,\mathrm{mT}$ at $q = 0.5\,\mathrm{nm}^{-1}$ and $q = 1.5\,\mathrm{nm}^{-1}$.

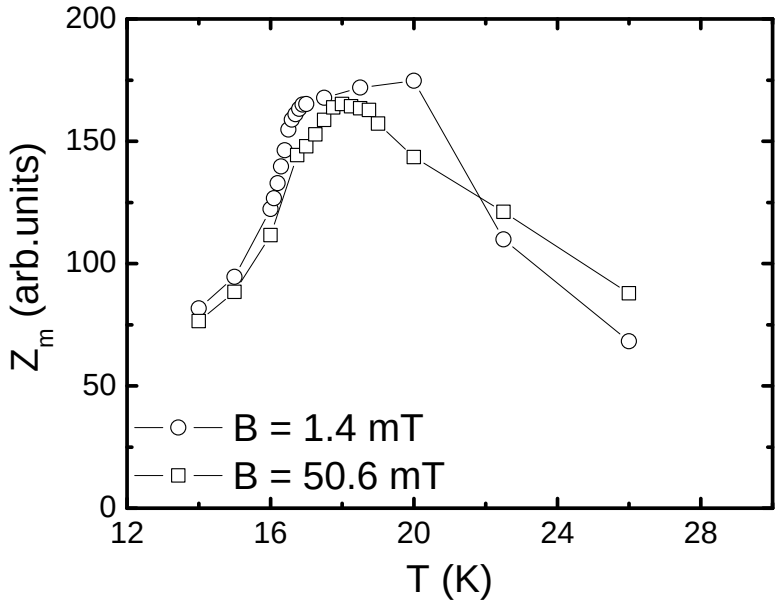

Figure 4.9: Temperature dependence of the parameter Z_m for two magnetic fields $B = 1.4\,\mathrm{mT}$ and $50.6\,\mathrm{mT}$. Solid lines serve only as a guide to the eye.

$Z_m = \chi(0)\kappa^2$ is expected to be constant at all temperatures as reported in numerous studies ($q \geq 1\,\mathrm{nm}^{-1}$) with triple axis spectroscopy [69, 53]. Our SANS data show a rather surprising temperature dependence of the amplitude of spin fluctuations Z_m.
The parameter Z_m exhibits a smooth growth when T approaches T_C from the high temperature side. Then Z_m becomes almost constant in the critical regime at $T_C < T < T_C(1+\tau)$ with $\tau < 0.1$. Z_m decreases sharply as soon as the temperature crosses the critical temperature $T_C = 16.5\,\mathrm{K}$. First we guess that a possible explanation of the temperature bahaviour of Z_m may be related to the fact that the linewidth Γ of spin fluctuations increases with increasing temperature and therefore for a SANS experiment where the integration over the energy is performed, we did not integrated over all spin fluctuations. This is not true since for EuS the linewidth of the spin fluctuations is $\Gamma(T = T_C) = A_{EuS}q^{2.5} = 0.006\,\mathrm{meV}$ (where $A_{EuS} = 2.1\,\mathrm{meV\ \AA}^{2.5}$ [53]) for $q = 0.5\,\mathrm{nm}^{-1}$ is significantly smaller than the energy of the incomming neutrons $E_i = 2.27\,\mathrm{meV}$. It should be noticed that our measurement was performed in the dipolar regime for $0.5\,\mathrm{nm}^{-}1 \leq q \leq 2.5\,\mathrm{nm}^{-1}$ while results of triple axis spectroscopy in [69, 53] are in the range $1\,\mathrm{nm}^{-}1 \leq q \leq 3.5\,\mathrm{nm}^{-1}$. Therefore we conclude that the amplitude of the spin fluctuations Z_m may be strongly affected by the dipolar interactions. As displayed in Fig. 4.10, the cor-

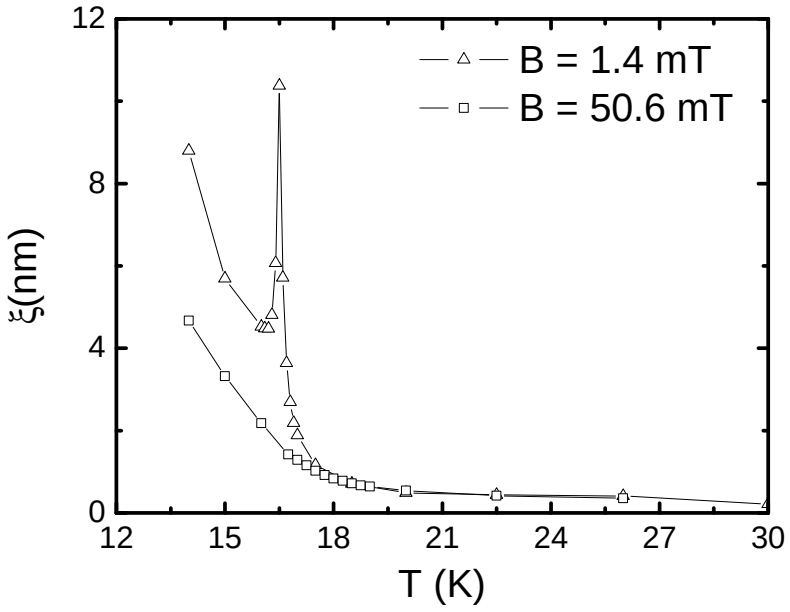

Figure 4.10: Temperature dependence of the correlation length for two magnetic fields $B = 1.4\,\mathrm{mT}$ and $50.6\,\mathrm{mT}$. Solid lines serve only as a guide to the eye. Our data agree with previous studies of critical properties of EuS [69].

relation length ξ shows a sharp maximum as the temperature approaches T_C. Below T_C, the correlation length decreases first as the contribution of the longitudinal fluctuations decreases with decreasing temperature and increases again due to the domain formation. When the magnetic field is applied, the maximum at T_c vanishes and the transition is

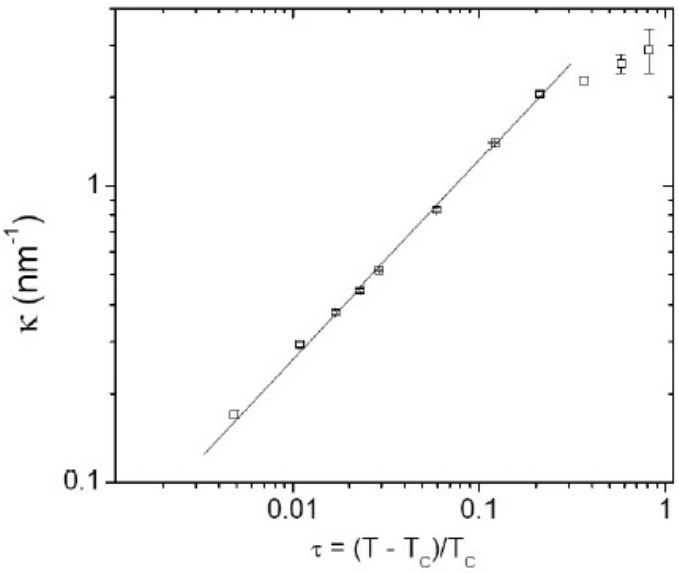

Figure 4.11: Inverse correlation length κ as function of the reduced temperature $\tau = (T - T_C)/T_C$ on a log-log scale at $B = 1.4\,\text{mT}$. Solid line is a fit to data using the expression $\kappa = (a)^{-1}\tau^{\nu}$.

smeared out. The temperature dependence of the inverse correlation length κ is shown in Fig. 4.11 on a log-log scale. κ obeys the scaling law $\kappa = (a)^{-1}\tau^{\nu}$ where τ is the reduced temperature in a range of $0.005 < \tau < 0.2$, with the constant $a = 0.17 \pm 0.01\,\text{nm}$ and the critical exponent $\nu = 0.67 \pm 0.02$. The obtained parameters are close to those obtained in Ref. [49], where they were found to be $a = 0.19\,\text{nm}$ and $\nu = 0.70 \pm 0.02$. There is clear crossover at $\tau = 0.2$ ($T \approx 20\,\text{K}$) to the non critical regime.

4.4 Discussions of Results

4.4.1 Pair Correlation Function

Effect of Magnetic Field on the Correlation Length

As seen in Fig. 4.10, the magnetic field affects the correlation length ξ in the close vicinity of T_C. Fig. 4.12 shows the magnetic field dependence of the correlation length at $T = 16.55\,\text{K}$. The value of ξ depends strongly on the field for $T = T_C$, while it has a weak dependence at $T \sim 17\,\text{K}$ and almost no dependence at $T > 17\,\text{K}$ as shown in Fig. 4.13 (Right panel). These results agree very well with previous studies [69]. As was noted above, the parameter Z_m has little or no change with magnetic field. The effect of magnetic field on the correlation length of the critical fluctuations can be understood in terms of the balance between the energy of the magnetic field $gB\mu_B$ and that of the critical fluctuations $\kappa_B T_C(\kappa a_0)^z$ with $\kappa = \xi^{-1}$. Here the dynamic critical exponent is $z = 2$ in the dipolar dominated regime for $q < q_d$ and $z = 2.5$ in the exchange dominated regime for $q > q_d$ [60, 7]. For $gB\mu_B \gg \kappa_B T_C[a_0\kappa_0]^z$, the correlation length is renormalized as a

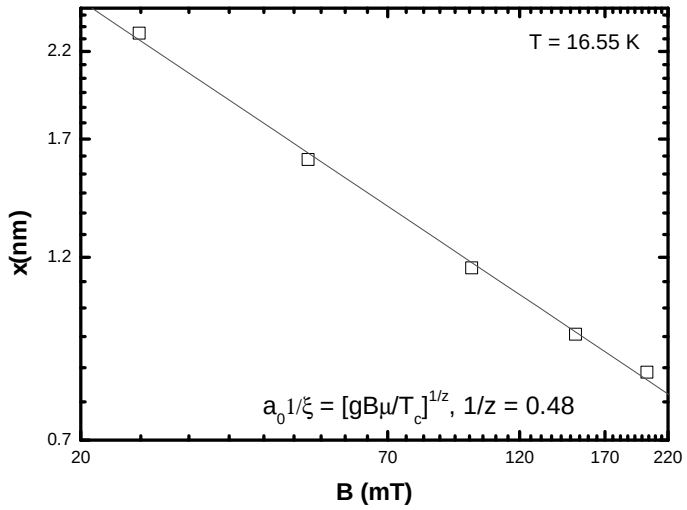

Figure 4.12: Inverse correlation length $\kappa = \xi^{-1}$ as function of the magnetic field as measured at $T \approx T_C = 16.5\,\mathrm{K}$. Solid line is a fit to the data with Eq. 4.5 giving a value of $z = 2.08$ for the dynamical critical exponent.

function of the magnetic field:

$$a_0\kappa_B = \left(\frac{gB\mu_B}{T_C}\right)^{1/z}. \tag{4.5}$$

The observed behavior of κ at $T \approx T_C$ is a result of the crossover to the strong field regime. We fitted the data using Eq. 4.5 and get a value for the parameter $1/z = 0.48 \pm 0.02$, which is close to theoretical value in the dipolar regime where $1/z = 0.5$. The observed renormalization of κ_B indicates that for $q \leq \kappa_B$ the energy of the critical fluctuations $\Omega = \kappa_B T_C(\kappa_0 a_0)^z$ is determined by the field B. For $q \geq \kappa_B$ the energy is equal to $\Omega_c = \kappa_B T_C(qa_0)^z$ and the magnetic field can be considered to be a weak perturbation. Shown in Fig. 4.13 is the field dependence of the correlation length at $T = 17\,\mathrm{K}$, $T = 18\,\mathrm{K}$ and $T = 19\,\mathrm{K}$ on a log-log scale. The solid line is a fit to the data using Eq. 4.5. We get the value $1/z = 0.267$ which is much smaller than the universal dynamic critical exponent. Then we conclude that for temperatures above T_C Eq. 4.5 does not described the correlation length of the spin fluctuations in the presence of an external magnetic field.

4.4.2 Three-Spin Correlation Function

Fig. 4.14 shows typical asymmetric scattering data $\Delta I(q)$ at the magnetic field $B = 50\,\mathrm{mT}$ for $T = 16.55\,\mathrm{K}$.

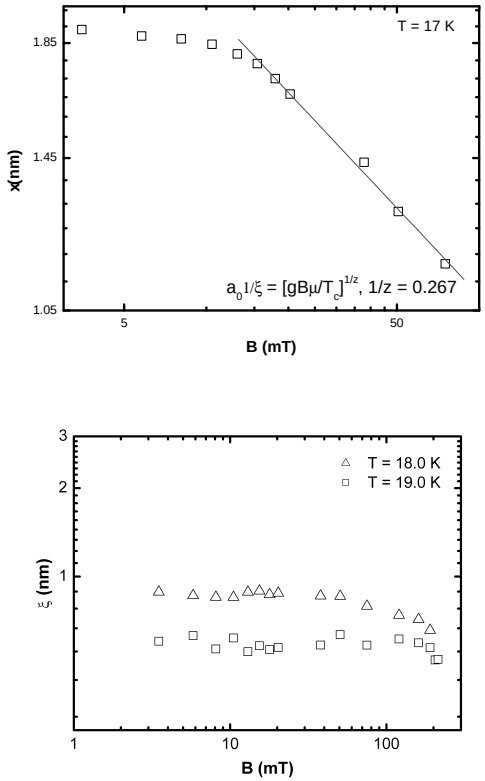

Figure 4.13: Correlation length $\xi = \kappa^{-1}$ as function of the magnetic field as measured at $T = 17\,\mathrm{K}$. Data have been fitted with Eq. 4.5 (solid line). At temperatures $T = 18\,\mathrm{K}$ and $T = 19\,\mathrm{K}$ the correlation length shows no dependence on the applied magnetic field.

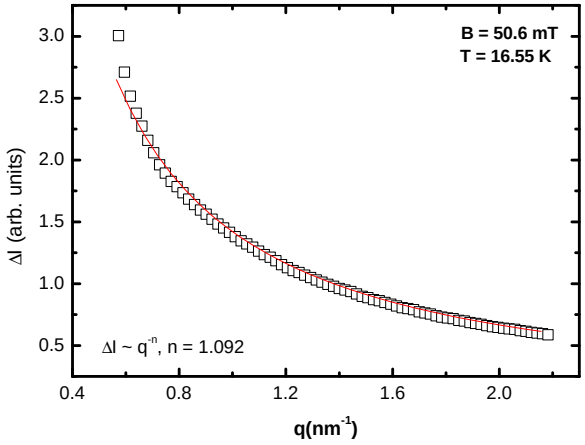

Figure 4.14: q dependence of the asymmetric part of the SAPNS difference intensity ΔI in magnetic fields $B = 50\,\mathrm{mT}$ at $T = 16.55\,\mathrm{K}$. Data have been fitted with $\Delta I \propto q^n$ (solid line) and we get $n = 1.09$.

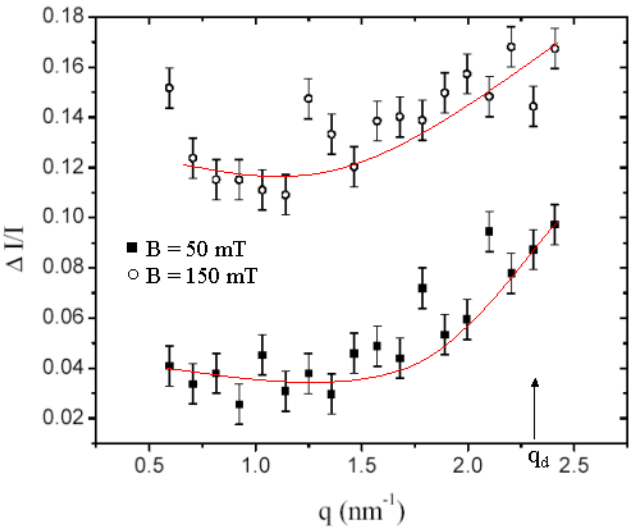

Figure 4.15: Normalized values of $\Delta I/I_{\sum}$ in magnetic fields $B = 50\,\mathrm{mT}$ and $B = 150\,\mathrm{mT}$. The value of the dipolar wave number $q_d = 2.3\,\mathrm{nm}^{-1}$ is marked by an arrow. The solid lines serve only as a guide to the eye.

The analytical expression for $\Delta I(q)$ given by Eq. 4.3 is known in a rough approximation and is valid within the range $\kappa < k_i\theta < q_{in}$,where the inelastic characteristic momentum q_{in} in Eq. 3.28 is of the order of $10\,\mathrm{mm}^{-1}$ for EuS. Our data follow closely $1/q$ however the theory presented in [41] predicts a $1/q^2$. The reason of this discrepency is not known. The remarkable features of this APD scattering contribution are the following:

(1) It appears only when the inclination angle ϕ between the magnetic field $\mathbf{B}$ and the incident beam direction k_i is not equal to 0 or $\pi/2$. Its appearance in this inclined geometry implies the dynamical nature of the scattering.

(2) $\Delta I(q)$ changes sign when the scattering vector q changes sign indicating a single handedness.

(3) It increases with the applied magnetic field $\vec{B}$.

(4) It vanishes for non-polarized neutrons ($P_0 = 0$).

All these features clearly identify this scattering to arise from the three spin correlations. It is sometimes convenient to normalize the asymmetric scattering by the symmetric magnetic scattering $\sigma = \Delta I(q)/I_{\sum}(q)$ as shown in Sec.3.3.2. σ is presented in Fig. 4.15 as a function of q. These data demonstrate that it is constant at small q and in low fields and has a tendency to increase at large q. Therefore, the q dependences of $\Delta I(q)$ and $I_{\sum}(q)$ are equivalent at small q while they are different at large q. The last feature may be connected with the dipolar interactions of the spin system at $q = q_d \approx 2.2\,\mathrm{nm}^{-1}$. The restricted q range of measurements does not allow us, however, to make more definite conclusions on the q dependence of the asymmetric scattering.
Due to the very low intensities obtained for ΔI as function of the temperature and magnetic field we have averaged $\Delta I(q)$ over q ranges within the limits (i) $0.50 < q < 1\,\mathrm{nm}^{-1}$;

(ii) $1 < q < 1.5\,\mathrm{nm}^{-1}$; and (iii) $1.5 < q < 2.3\,\mathrm{nm}^{-1}$. Fig. 4.16 displays the averaged values versus B for $T = 16.55\,\mathrm{K}$. For all q values, $\langle \Delta I \rangle$ increases with increasing field and saturates above $B \sim 150\,\mathrm{mT}$. The increase of $\langle \Delta I \rangle$ is clearly related to the range of B where $q > \kappa_B$ (i.e to the weak field regime) and it saturates as soon as $\kappa_B \sim q$. This observation demonstrates the validity of the weak field approximation for the concept described above.

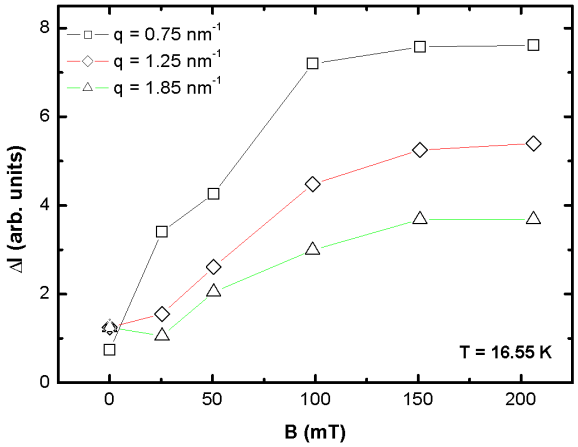

Figure 4.16: Magnetic field dependence of $\langle \Delta I \rangle$ for three different q values $q = 0.75\,\mathrm{nm}^{-1}$, $q = 1.25\,\mathrm{nm}^{-1}$, and $q = 1.85\,\mathrm{nm}^{-1}$ at $T = 16.55\,\mathrm{K}$. Solid lines serve only as a guide to the eye.

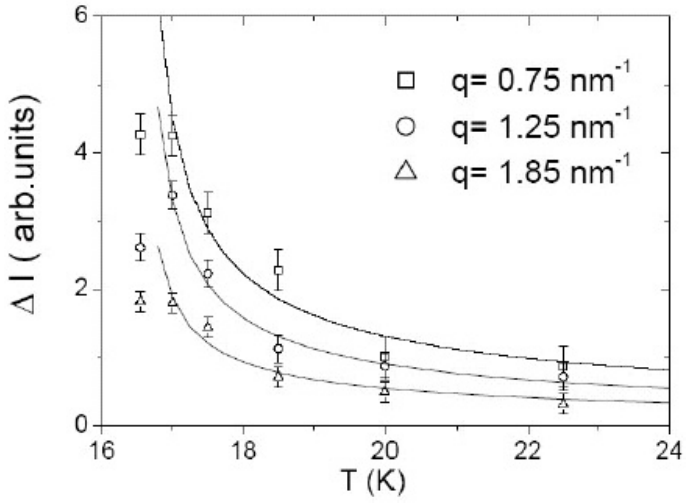

Figure 4.17: Temperature dependence of $\langle \Delta I \rangle$ for three different q values $q = 0.75\,\mathrm{nm}^{-1}$, $q = 1.25\,\mathrm{nm}^{-1}$, and $q = 1.85\,\mathrm{nm}^{-1}$ in a field of $B = 50\,\mathrm{mT}$. Solid lines are fits to data using $\langle \Delta I \rangle = A\tau^{-\nu}$ where A is a constant.

The temperature dependence of $\langle \Delta I \rangle$ is shown in Fig. 4.17 for $B = 50\,\mathrm{mT}$. The theory predicts that the value $\langle \Delta I \rangle$ depends on the temperature as τ^{ν}. The parameters obtained

by fitting the experimental data (solid lines) are $\nu = 0.62(0.05)$ for $q = 1.85\,\mathrm{nm}^{-1}$; $\nu = 0.65(0.03)$ for $q = 1.25\,\mathrm{nm}^{-1}$; and $\nu = 0.64(0.04)$ for $q = 0.75\,\mathrm{nm}^{-1}$. The points at $T = T_C$ do not follow the scaling law $\tau^{-\nu}$. This may be related to the crossover to the strong field regime and/or to the demagnetization effects. According to the Eq. 3.22, the observed increase of the intensity ΔI is proportional to $\tau^{-\nu} = \xi$ at $q > \kappa$. It is interesting to note that the intensity attributed to the pair correlation function $I_{\sum} \sim 1/(a\kappa)^2 = \tau^{-2\nu} = \xi^2$ for $q \ll \kappa$. The factor of 2 difference between the exponents for the symmetric and antisymmetric scattering clearly proves the completely different origin of the observed scattering contributions. On the other hand, the exponents ν determined by means of the static measurements of ξ and the dynamic measurements(using the induced chirality) are in excellent agreement with each other, demonstrating the internal consistency of the theory and the experiment.

4.5 Summary

The ferromagnetic to paramagnetic phase transition in EuS has been investigated by means of small angle scattering of polarized neutrons using the inclined geometry of the applied field B with respect to the incident neutron wave vector k_i. This geometry of the experiment offers an alternative method to the conventional triple axis spectrometry to study magnetic critical fluctuations. The proposed method allows to distinguish between the two contribution to the scattering: (i) the pair correlation contribution which is symmetric and depends on the polarization and (ii) the contribution due to the three spin correlation function which is asymmetric and polarization independent.

The behavior of the pair correlation function of both contributions to the critical scattering has been studied as a function of temperature and magnetic field. The pair correlation function was deduced with its amplitude and the correlation length $\xi(T, B)$. At zero field the correlation length obeys the scaling law $\xi = a_0\tau^{-\nu}$ with $a_0 = 0.17 \pm 0.01$ and $\nu = 0.707 \pm 0.02$. The magnetic field strongly influences the critical fluctuations near T_c, so that the correlation length is suppressed by the field as $\xi(B) = a_0(g\mu_B B/T_C)^{1/z}$ with the dynamic critical exponent $z = 2.1 \pm 0.1$, which is close to the theoretically predicted value $z = 2$ for the dipolar regime $\kappa < q_d$.
The scattering contribution due to the induced chirality (APD) was unambiguously identified as arising from the three spin correlation function. The specific features of the scattering may be summarized as follows:

(i) It is asymmetric and depends on the polarization.

(ii) It appears only in the inclined geometry and implies the dynamical and chiral nature of the fluctuations.

The analytical expression for this scattering is known within the weak field approximation and for the limited q range $\kappa < q < q_{in}$. The theory predicts that the scaling behaviors of the scattering cross section is proportional to $\tau^{-\nu}$ with $\nu = 0.66$ [41]. The values of the critical exponents obtained experimentally for different q values in the range $\kappa < q < q_{in}$ are $\nu = 0.62 \pm 0.05$, $\nu = 0.65 \pm 0.03$, and $\nu = 0.64 \pm 0.04$. These results are in

good agreement with the theoretical predictions. Magnetic critical scattering has been performed on pure ion [54]. Their results agree with our data. Moreover, to the best of our knowledge, the SANS with the inclined geometry is an efficient method to study the three-spin correlation functions by inducing the chirality in magnetic systems. It is an alternative method to the traditional triple axis spectroscopy in the determination of critical exponents.

Chapter 5

Critical Magnetic Scattering from the Itinerant Magnet MnSi

Ni la contradiction n' est marque de faussete ni l' incontradiction n' est marque de verite.
Pascal

5.1 Introduction

Incommensurate ordering and chirality in strongly correlated magnetic materials have recently received much attention. In this regard non-centrosymmetric cubic MnSi plays a particular role because it is one of the very few systems with very peculiar properties:

(i) MnSi shows an itinerant ferromagnetic behaviour on length-scales of a few lattice constants [70].

(ii) The crystal structure lacks an inversion symmetry and weak spin-orbit interactions assume a Dzyaloshinskii-Moriya (DM) form $D_m \cdot (\vec{S}_1 \times \vec{S}_2)$ which destabilizes the uniform ferromagnetic order and introduces at ambient pressure a well-understood long-wavelength helical modulation [24, 23]. The sign of the Dzyaloshinskii term D_m yields the left- or right handed rotation of the neighboring spins along the pitch of the helix.

(iii) Well above T_c chiral magnetic fluctuations have been obeserved. Here the magnetic anisotropies are lost and the maximum of magnetic scattering is located on spheres around the nuclear Bragg peaks [27, 71].

(iv) The magnetic ground state appears to switch abruptly from a weakly spin-polarised Fermi-Liquid to an extended non-Fermi liquid (NFL) phase at a pressure of 14.6 kbar [72].

(v) Neutron scattering shows that large moments survive far into the NFL-phase, where the scattering intensity observed everywhere on the surface of a small sphere suggests partial order analogous to liquid crystals [73].

In this part of the thesis we studied the critical spin fluctuations in the weak itinerant magnet MnSi. We determine the critical exponents and compare these with values predicted for 3D Heisenberg ferromagnets. Furthermore we investigated the reorientational processes of the helical modulation at ambient pressure and zero magnetic field. We combine small-angle neutron scattering with AC susceptibility, DC magnetization and specific heat data. This provides unexpected behaviour of the helical modulation.

5.2 Review of Previous Findings on MnSi

Crystal Structure

MnSi crystallizes in the B20 structure and the cubic space group $P2_13$ with a lattice constant $a = 4.558\,\text{Å}$ lacking a center of symmetry [23]. There has been no clear interpretation in terms of chemical bonding of why MnSi prefers the B20 structure. The cubic structure of MnSi is shown in Fig. 5.1. There are four Mn atoms and four Si atoms in the unit cell. The positions of Mn and Si atoms in a unit cell are given by $(u, u, u), (1/2 + u, 1/2 - u, -u), (-u, 1/2 + u, 1/2 - u)$ and $(1/2 - u, -u, 1/2 + u)$. The corresponding values for the internal atom-position parameters are $u_{Mn} = 0.137$ and $u_{Si} = 0.845$. This structural information is important because the symmetry of the crystal structure and the type of magnetic order are connected [74]. The local coordination of Mn consists of a Si neighbor at $2.11\,\text{Å}$ (lying along $\langle 111 \rangle$ direction and three neighbors at $2.35\,\text{Å}$ and another three neighbors at $2.69\,\text{Å}$. The point symmetry at the Mn and Si sites is C_3. Taking into account time-reversal symmetry with the twelve space group operations, the irreducible Brillouin zone is $1/24$ of the full zone. Note that the Mn-Mn distance is almost the same as that in γ manganese metals where $d_{Mn-Mn} = 2.725\,\text{Å}$ [75].

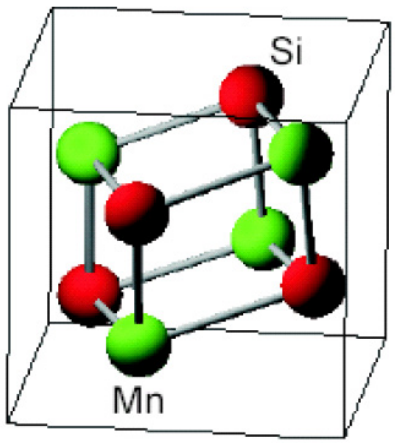

Figure 5.1: Crystal structure of the cubic itinerant magnet MnSi [76].

B-T Phase Diagram

Shown in Fig. 5.2 is the magnetic phase diagram of MnSi as obtained from results of the susceptibility [77] and neutron scattering data [75]. Data show good agreement between the two methods. The cubic inter-metallic compound MnSi becomes magnetically ordered below $T_c = 29\,\mathrm{K}$. It was established by Ishikawa et al. [70] that the magnetic oder in the absence of a field has a long range modulation with repeat distance up to $\lambda = 2\pi/q = 180\,\text{Å}$. The spin arrangement corresponds to a helical structure that has been attributed to the lack of inversion symmetry in its B20 structure, which brings the Dzyaloshinskii-Moriya interaction into play [24]. In the ordered phase, spin-orbit interactions lock the direction of the spiral to $\langle 111 \rangle$ axis therefore the magnetic spiral propagates along the $\langle 111 \rangle$ direction of the crystal with a vector $k_0 = (2\pi/a)(\xi, \xi, \xi)$ where $\xi = 0.017$. Thus locally, along the direction of propagation, the spin structure looks very similar to a ferromagnet. Within each plane the spins are ferromagnetically aligned, but the spins in neighboring planes are turned by an angle, determined by the ratio D_m/J, where D_m is the Dzyaloshinskii term and J the exchange parameter. Typical sizes of magnetic domains in the ordered phase are 10^4 Å [32].
A magnetic field of $0.6\,\mathrm{T}$ is sufficient to transform the system to an induced ferromagnetic state [75]. In a magnetic field greater than $0.6\,\mathrm{T}$, the crystal is saturated with a spontaneous magnetic moment $\mu_s \approx 0.4\mu_B$ per manganese atom which is substantially smaller than the effective moment of $\mu_{eff} = 2.2\mu_B$/Mn evaluated from the Curie-Weiss relation in the paramagnetic state [16]. The magnetic field and pressure dependences of the magnetization are strong and the anomaly in the specific heat at the critical temperature is much smaller than expected from a Heisenberg ferromagnet. These properties indicate that MnSi is a weak itinerant magnet [16].

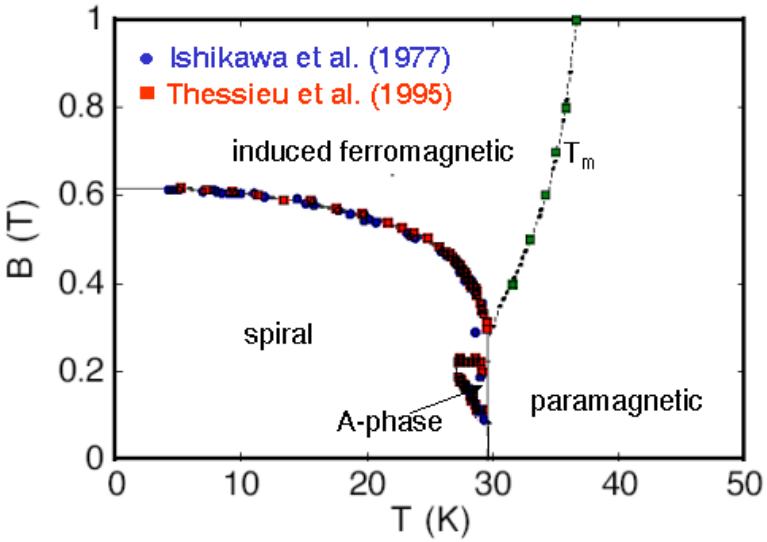

Figure 5.2: Magnetic phase diagram of MnSi resulting from bulk measurements in [77] and neutron scattering data in [75]. Data show good agreement between the two methods. A small pocket, the so-called A-phase is observed below T_c. A broad peak appears in the susceptibility at T_m above the critical temperature.

AC susceptibility measurements in [77] as well as magnetization and magneto resistance measurements in [78] reveal anomalous peaks close to T_c in magnetic field between 0.1 and $0.22\,\mathrm{T}$ suggesting the existence of a new phase close to T_c, a pocket in the low field region of magnetic phase diagram near T_c and is called the A-phase. While the A-phase was at first interpreted in terms of a paramagnetic state [79], it was eventually found that the A-phase also yields a modulated magnetic structure for which the wave-vector $\vec{q}$ assumes a direction perpendicular to the magnetic field that was applied along the $\langle 100 \rangle$ direction of the crystal [32, 26]. The nature of the A-phase is still subject of discussions. In this work, we have revisited the question of the nature of the A-phase of MnSi in a comprehensive study combining small angle neutron scattering with measurements of the AC susceptibility, DC magnetization and specific heat.
In magnetic fields above $0.3\,\mathrm{T}$ a broad peak appears in the susceptibility at T_m above the critical temperature [77]. T_m has being interpreted as the temperature at which the properties of an itinerant magnet change from those of an essentially non-polarized state at $T > T_m$ to those of an induced ferromagnetic state at $T < T_m$.

P-T Phase Diagram of MnSi

Fig. 5.3 shows the temperature versus pressure diagram of MnSi as reported in Ref. [73]. The temperature drops with pressure until magnetic order disappears at the critical pressure $p_c = 14.6\,\mathrm{kbar}$ [73, 80, 77]. In the pressure range up to $5.2\,\mathrm{kbar}$, Bloch et al.

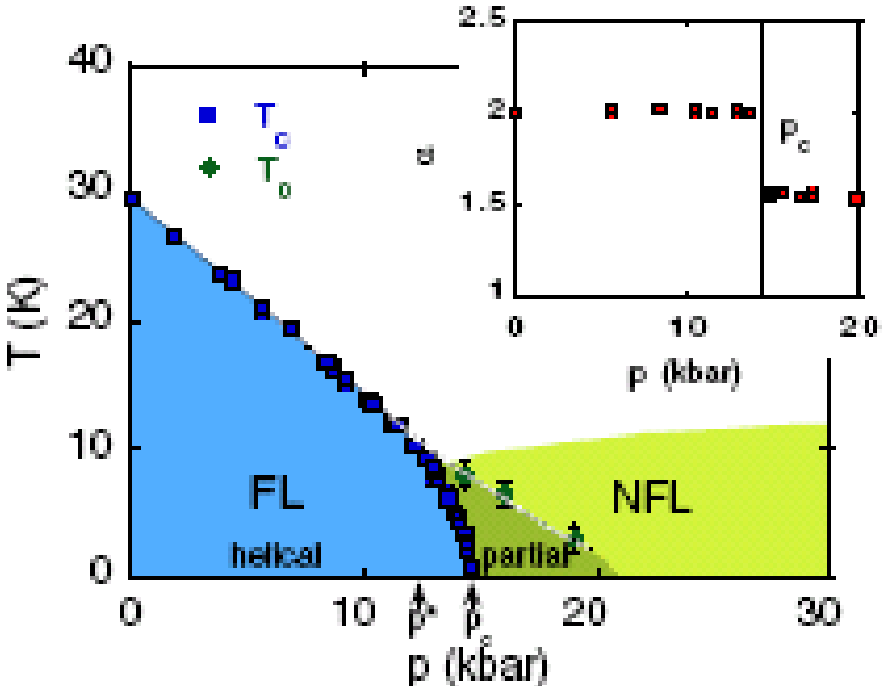

Figure 5.3: Non-Fermi-Liquid behaviour of MnSi under applied pressure as taken from [81]. The exponent α describing the electrical resistivity changes abruptly from the value of a Fermi-liquid ($\alpha \approx 2$) to a non-Fermi liquid ($\alpha \approx 3/2$) when pressures larger than p_c are applied. The non-Fermi liquid phase extends at least up to $2p_c$ [76].

[82] observed a decrease of ordering temperature upon increasing pressure at the rate

$d \log T_c/dp = -3.9 \times 10^{-2}\,\text{kbar}^{-1}$. Recently Pfleiderer et al. [80, 83, 73] succeeded to suppress the magnetically ordered phase by a pressure of $14.6\,\text{kbar}$ and a quantum phase transition (QPT) is reached. Below $p^* \approx 12\,\text{kbar}$ the phase transition is of second order, while above p^* it is weakly first order. Close to the QPT the temperature dependent part of the electrical resistivity shows deviations from the Fermi liquid behavior with $\Delta\rho = AT^{3/2}$ over a wide temperature range [72]. Later it was found that the magnetic system in the range of $p_c < p < 22\,\text{kbar}$ at temperatures below $T_0 \approx 8\,\text{K}$ is partially ordered with the preferential direction along $\langle 110 \rangle$. This findings support the existence of novel metallic phases with partial ordering of the conduction electrons as proposed for the high temperature superconductors [84] and heavy-fermion compounds [85]. Up to now the origin of the partial order and of the non-Fermi liquid behaviour is unclear.
One of the interesting question to study is whether the partial order observed under pressure and the chiral fluctuations above T_c at ambient pressure are connected.

5.3 Experimental Details

For the characterization of critical phenomena, high-quality samples preferably single crystal are needed to avoid smearing of T_c. Two different high quality single crystal of MnSi denoted as sample-A and sample-J are used for our investigations. Detailed informations on the samples used for SANS measurements are summarized in Tab. 5.1.
Both samples have to be mounted on a sample holder with a skew of 24° (vertical direction) and tilted in the horizontal direction to 18° in order to have the $\langle 111 \rangle$ and the $\langle 11\bar{1} \rangle$ in the scattering plane since the crystal grow with these inclinations.
(i) Sample-A has been used for our preliminary SANS measurements. It is a disk with $20\,\text{mm}$ diameter and $2\,\text{mm}$ thickness cut from a single crystal of MnSi grown at Ames Laboratory. Sample-A has three different grains and the crystallographic mosaicity of the sample (for each grain) was measured on the neutron spectrometer "Reflex" at the Forschungszentrum Jülich (Germany). The average value of the FWHM over all measured reflections is 0.22°. All the SANS measurements on sample-A were performed on the same crystal grain.

DC and AC magnetization measurements were also carried out on the sample-A with

	origin	shape	size	mosaic	RRR
sample-A	Ames Lab.	disc	$20\,\text{mm} \times 2\,\text{mm}$	0.22°	-
sample-J	Japan (Tohoku)	disc	$20\,\text{mm} \times 2\,\text{mm}$	0.21°	70-100

Table 5.1: Characteristics of the samples of MnSi used for SANS measurements.

approximate dimensions $3 \times 1 \times 1\,\text{mm}^3$ and a mass of $16.6\,\text{mg}$. For specific heat measurements sample-A of approximate size $1.5 \times 1.5 \times 1.5\,\text{mm}^3$ and a mass of $10.07\,\text{mg}$ was used.
(ii) The second single crystal denoted sample-J was grown by the Bridgman method from high purity starting materials. The sample has a residual resistivity ratio in the range 70

to 100 that indicates the high quality of the sample. Sample-J has a single grain in contrast to sample-A. The structural mosaic of the sample is 0.21° as shown in Fig. 5.4 was determined with the X-ray diffractometer "D500" at the Physics Department E21 (TU-München).

Measurements of AC susceptibility was performed on sample-J weighing 23.74 mg with

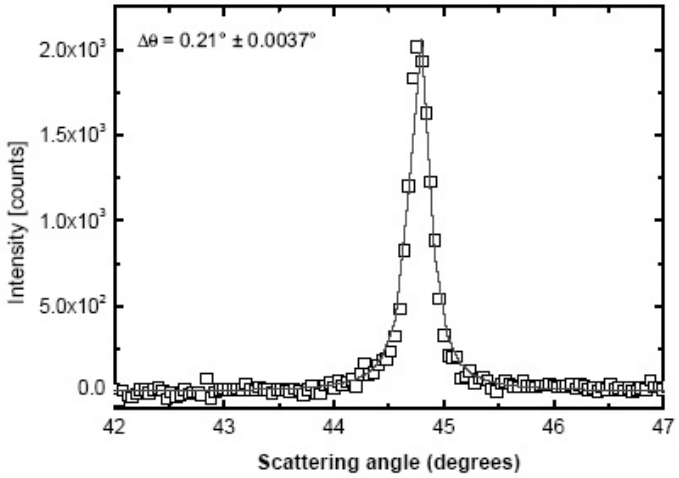

Figure 5.4: Crystal mosaic of the single crystal MnSi as measured by the X-ray diffractometer D500 at the Physics Department E21. Data have been fitted with a Gaussian to get the value of the crystal mosaic of 0.21°.

the size of approximately $3 \times 1 \times 1\,\text{mm}^3$. Sample-J used for the specific heat measurements has approximate dimensions $1.5 \times 1.5 \times 1.5\,\text{mm}^3$ and weighing 17.9 mg.

Small-angle polarized neutron scattering (SAPNS) experiments during this thesis were performed on both samples at the SANS-2 instrument of the FRG-1 neutron source in Geesthacht (Germany). The incomming neutron beam has an initial polarization of $P_0 = 0.95$ with a selected wavelength $\lambda = 0.58\,\text{nm}$ which is above the spacing $a = 0.4558\,\text{nm}$ of MnSi, so that only magnetic scattering and no nuclear Bragg scattering can be observed. The wavelength spread and the beam divergence were $\Delta\lambda/\lambda = 0.1$ and 2.5 mrad, respectively. The scattered neutrons were detected with a position sensitive detector with 128×128 pixels and a spatial resolution of $4.4\,\text{nm}$. A q-range from 6×10^{-2} to $1\,\text{nm}^{-1}$ was explored. The incident beam was directed along $\langle 1 - 10\rangle$, so that the vectors parallel to $\langle 111\rangle$ and $\langle 11 - 1\rangle$ were in the scattering plane and perpendicular to the beam as shown schematically in Fig. 5.5. The magnetic guide field of $1\,\text{mT}$ was in this plane along $\langle 11 - 2\rangle$ i.e. perpendicular to $\langle 111\rangle$. The temperature was measured with an accuracy that was better than $0.05\,\text{K}$ using a Lakeshore temperature controller. In all bulk measurements temperatures were measure by conventional resistance sensors at an accuracy better than 1%.

Further SANS-experiments were carried out on sample-J at the diffractometer MIRA at the new neutron source FRM-II in Munich. The sample with a diameter of $14\,\text{mm}$ was illuminated by a neutron beam with a wavelength $\lambda = 9.8\,\text{Å}$. An aperture with $10\,\text{mm}$ width and $14\,\text{mm}$ height was place $1.87\,\text{m}$ before the sample. The data were recorded by means of an area detector with 1024×1024 pixels and a horizontal and vertical resolution

of 1 mm and 2 mm, respectively, that was placed 1.4 m from the sample.

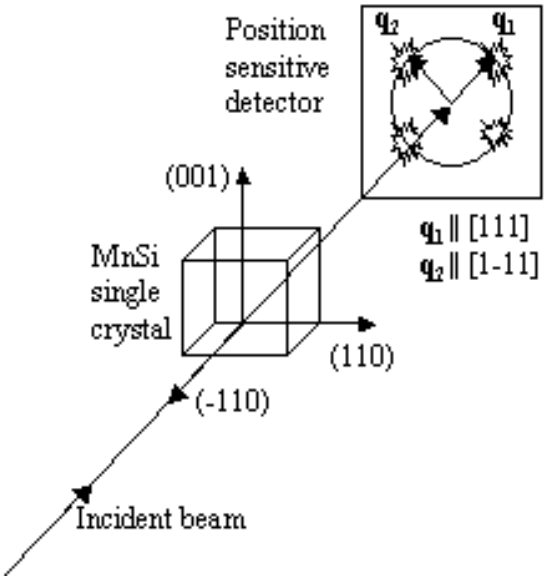

Figure 5.5: Schematic view of the scattering geometry used in the small angle scattering measurements on MnSi. The positions of the magnetic peaks are observed around (000) in the (-110) plane. The circle surrounding the center of the detector illustrates the ring of constant $|q|$ which appears in the critical scattering above T_c.

To perform data reduction on SANS data we used the software tools SANDRA (SANs Data Reduction and Analysis) [86] and GRASP (Graphical Reduction and Analysis SANS Program) [87] developped at the GKSS and at the ILL, respectively.

5.4 Results of Experiments

5.4.1 Bulk Measurements on MnSi

We study separately AC susceptibility, specific heat of MnSi at zero magnetic field in the temperature range of 2 to 300 K.

AC Susceptibility

Shown in in the left panels of Figs. 5.6 and 5.7 are the temperature dependence at zero field of the AC susceptibility of sample-A and sample-J of MnSi, respectively. The susceptibility increases with decreasing temperatures and shows a sharp peak indicating a phase transition at $T = 29$ K for sample-A and at $T = 29.7$ K for sample-J.

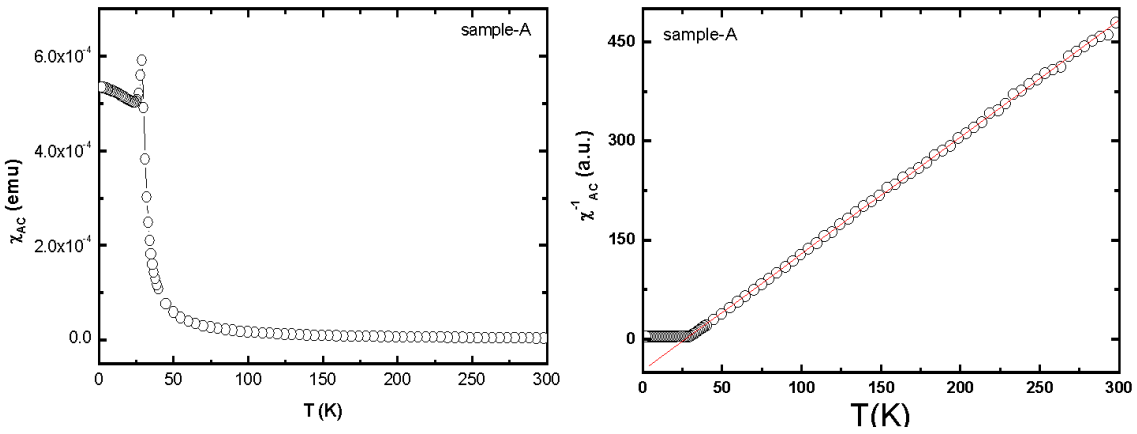

Figure 5.6: Zero field AC and inverse susceptibility of MnSi single crystal as function of temperature of sample-A. Transition temperature occurs at $T = 29\,\mathrm{K}$. The inverse susceptibility shows the Curie-Weiss behaviour above T_c with $\chi_{AC} \propto C/(T - T_c)$ where $C^{-1} = 1.77$ is the Curie constant evaluated from linear fit of the data above T_c (solid line).

Figs. 5.6 and 5.7 shows the inverse susceptibility of MnSi of sample-A and sample-J, respectively, as function of temperature at zero magnetic field. The AC susceptibility shows above T_c a typical Curie-Weiss behaviour where χ_{AC} follows $C/(T - T_c)$. From the linear fit of the data for $T > T_c$ we obtained the Curie constant (the Cuire constant is indicative of the number of magnetic spins per atom) $C^{-1} = 1.77 \pm 0.12$ corresponding to $\mu_{eff} = 2.53\,\mu_B$/Mn and $C^{-1} = 1.89 \pm 0.1$ corresponding to $\mu_{eff} = 2.45\,\mu_B$/Mn for sample-A and sample-J, respectively. These values of the effective moment μ_{eff} are similar within the experimental errors. Therefore a same magnetic behavior is expected for both samples. Below T_c, the susceptibility for both samples is saturated and the imaginary part is finite as expected for magnetically ordered phase in which magnetic domains are formed. Our results are in agreement with previous studies [77, 88].

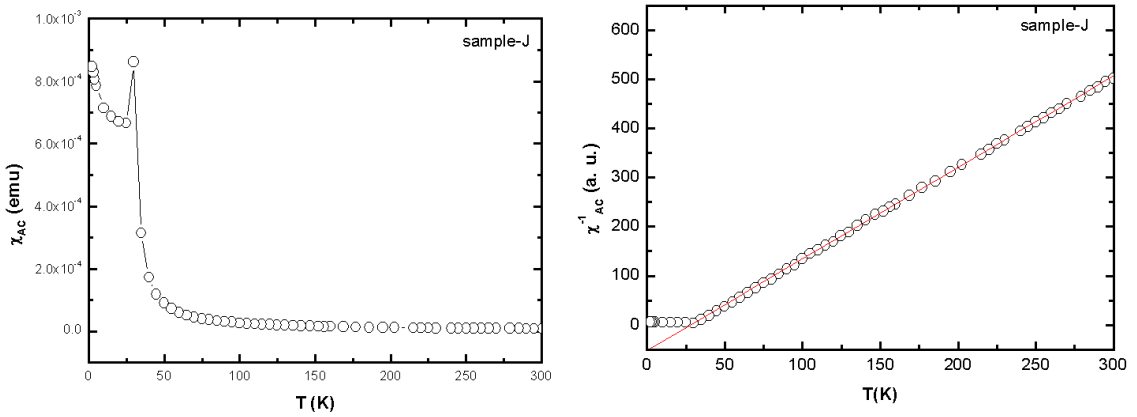

Figure 5.7: Zero field AC and inverse susceptibility of MnSi single crystal as function of temperature of sample-A. Transition temperature occurs at $T = 29.7\,\mathrm{K}$. The inverse susceptibility shows the Curie-Weiss behaviour above T_c with $\chi_{AC} \propto C/(T - T_c)$ where $C^{-1} = 1.89$ is the Curie constant evaluated from linear fit of the data above T_c (solid line).

Magnetic Specific Heat

The temperature dependence of the magnetic contribution to the specific heat C of both samples at zero magnetic field is depicted in Fig. 5.8. C is dominated by a pronounced peak at $T = 28.51\,\mathrm{K}$ for sample-A and at $T = 29\,\mathrm{K}$ for sample-J. With increasing temperature a broad shoulder appears at $T \sim 28.80\,\mathrm{K}$ (sample-A) and $T \sim 29.6\,\mathrm{K}$ (sample-J). These values are quite similar within the experimental errors with the temperature values of the AC susceptibility peaks. Interesting is that the peaks of the susceptibility and the specific heat measurements occur unexpectedly not at the same temperature. Traditionally the maximum value of the specific heat is taken as the phase transition from the paramagnetic state in to the helical phase.
With increasing temperature the specific heat data shows an inflexion point at $T = 30.8\,\mathrm{K}$ for the sample-J and another kink appears at $T = 29.9\,\mathrm{K}$ for sample-A. Notice that for both samples these values are approximately one degree above the sharp peak of the specific heat. These results are not consistent with a typical critical behaviour [3] therefore it is not possible to estimate any critical exponents from the bulk measurements.

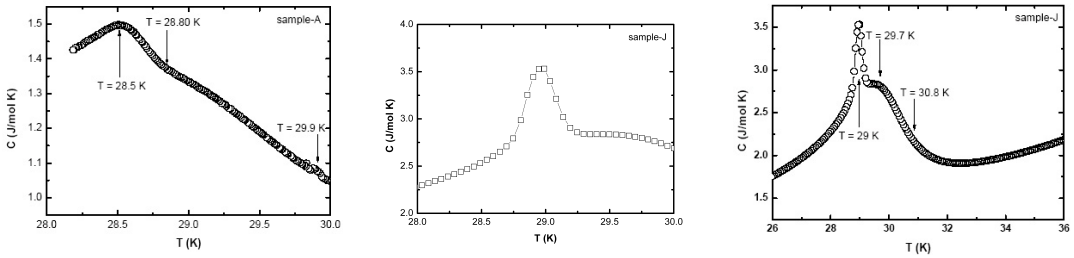

Figure 5.8: Temperature dependence of the magnetic specific heat at zero magnetic field of sample-A (Left panel) and sample-J (Right panel). A sharp peak at T_c and a broader shoulder above T_c are dominant features.

5.4.2 Magnetic Neutron Scattering from MnSi

Maps of the small angle polarized neutron scattering (SAPNS) intensities from sample-A at $T = 10\,\mathrm{K}$ at and above T_c for two neutron polarization P_0 along and opposite the guide field are shown in Fig. 5.9.
Below T_c four magnetic Bragg peaks are seen at $k = 0.39$ nm^{-1}. The observed Bragg peaks are reflections from the domains oriented along $\langle 111 \rangle$ and $\langle 11\bar{1} \rangle$. This is possible due to the large magnetic mosaic, as in the ideal case the Bragg condition would be only fulfilled for one reflection. In our geometry it is the $(11\bar{1})$ peak. The peaks at $k = (111)$ and $k = (\bar{1}\bar{1}\bar{1})$ are polarization-independent, as k is perpendicular to $P_0 \parallel \pm\langle 11-2 \rangle$. Reflections with $k = (11\bar{1})$ and $k = (\bar{1}\bar{1}1)$ depend on P_i as expected for helices with vectors along $\vec{q}$. Approaching T_c, the intensity of the Bragg peaks decreases and slowly smear out until they form a ring (half-moons shaped) around the position of the direct beam. These half moons are induced by the strong critical fluctuations in the orientation of the wave vector of the helix leading to diffuse scattering on a ring around the Bragg peaks. Above T_c, only diffuse scattering (half moons) is visible. The intensity of the ring

is maximal at a radius $q \simeq k$. There are weak spots on these half moons corresponding to former Bragg peaks.

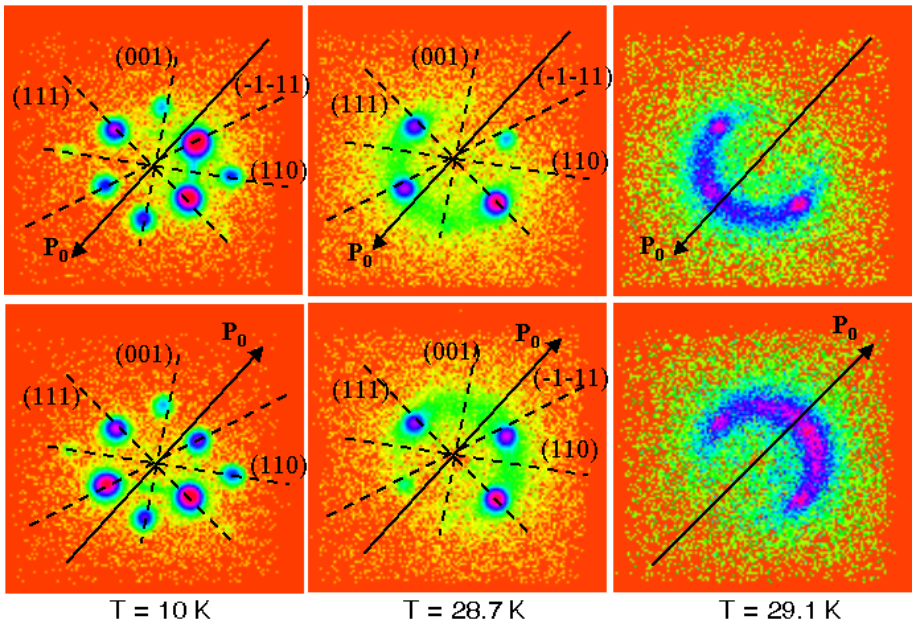

Figure 5.9: (Color online) Maps of the SAPNS intensities from sample-A at zero applied magnetic field for the polarization P_0 parallel to a $\langle 11-2 \rangle$ direction along the guide field (upper panel) and opposite to it (lower panel) at $T = 10\,\mathrm{K}$, $T = 28.7\,\mathrm{K}$ and $T = 29.1\,\mathrm{K}$.

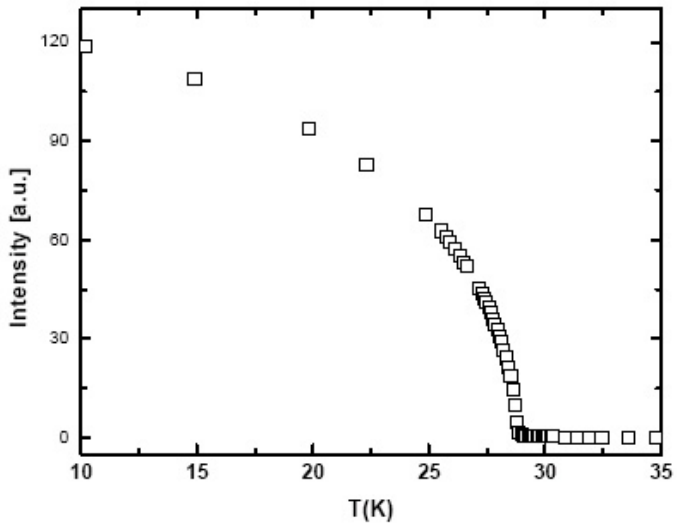

Figure 5.10: Intensity of the Bragg peak as function of temperature at zero field from sample-A.

The temperature dependence of the Bragg peaks shown in Fig. 5.10 clearly demonstrates that the intensity is reduced with increasing temperatures. The sharp peaks present at low temperatures disappear in the vicinity of $T_c = 28.8\,\mathrm{K}$, so that the scattering looks

like critical scattering from a ferromagnet. The temperature value $T_c = 28.8\,\mathrm{K}$ where the peak disappears is taken as the critical temperature. Fig. 5.11 displays the q scans along the easy direction ($\langle 111 \rangle$) across the ring at temperatures above T_c. Up to $T = 30\,\mathrm{K}$ the ring is observed then becomes unobservable with further increasing of the temperature.

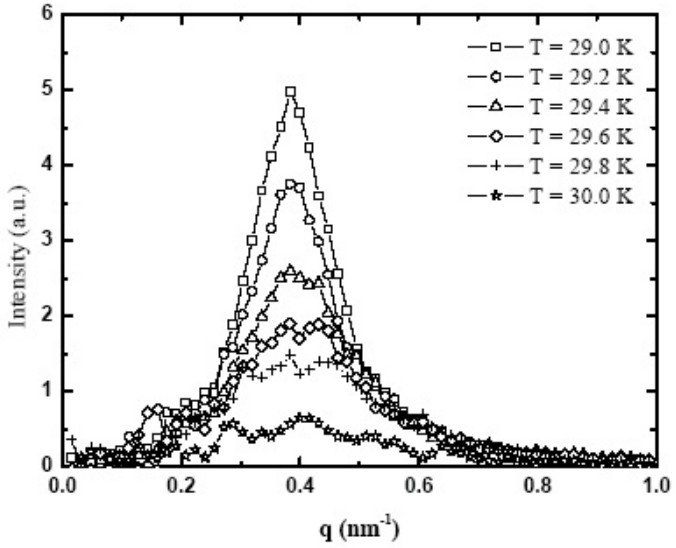

Figure 5.11: q-scans along the easy direction ($\langle 111 \rangle$) across the ring for different temperatures. Solid lines are guide to the eye. Results obtained from sample-A.

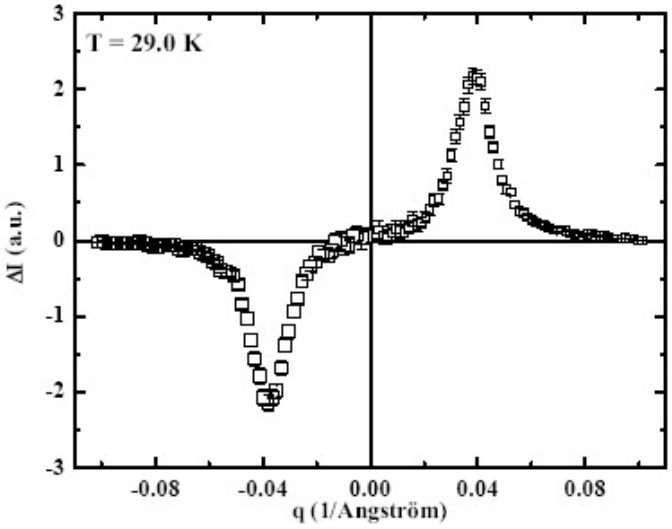

Figure 5.12: The difference of the small-angle scattering intensity (sample-A) for the two polarization directions of MnSi close to T_c is fully antisymmetric.

To elimnate the background we extract from the data the difference spectra of the two polarization directions. Therefore, the effect of background scattering is eliminated and

only the full anti-symmetric part of the magnetic cross section is considered as shown in Fig. 5.12.

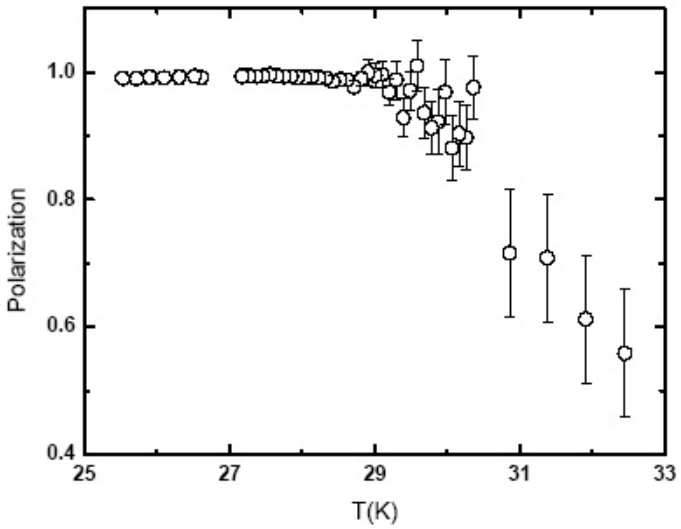

Figure 5.13: Temperature dependence of the polarization P_s that is parametrised according to Eq. 3.20 for a finite polarisation of the neutrons. A decrease of the polarization is noticed above T_c and it is constant for Bragg reflections at $T < T_c$.

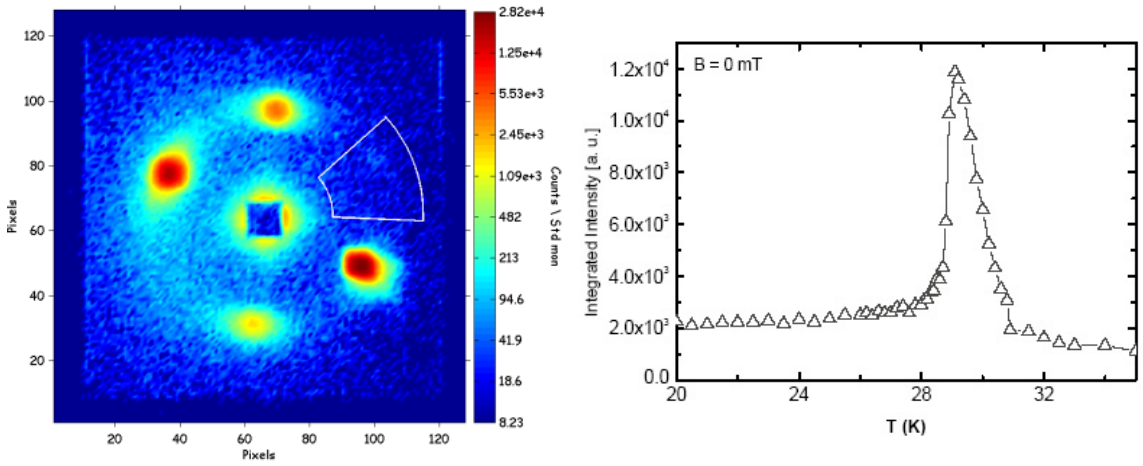

Figure 5.14: The region of integration of the ring of intensity is marked by the white line (Left panel). Integrated intensity of the ring versus temperature at zero magnetic field as obtained from sample-J (Right panel). The intensity in the ring is maximal at $T = 29.6\,\mathrm{K}$ and vanishes above $T \sim 30.85\,\mathrm{K}$. The solid line is to guide the eye.

The temperature dependence of the polarization P_s as determined by Eq. 3.20 is shown in Fig. 5.13. A decrease of the polarization is noticed above T_c and it is constant at $T < T_c$ in good agreement with the theory [40].
Shown in Fig. 5.14 (Right panel) is the temperature dependence of the ring (diffuse scattering) of intensity from sample-J as integrated whithin the marked region (white line)

on Fig. 5.14 (Left panel). The ring starts at $T \approx 29.1\,\mathrm{K}$, reaches a maximal value at $T = 29.8\,\mathrm{K}$ and then disappears completely into the background above $T \sim 30.85\,\mathrm{K}$. This value coincides with the inflexion point observed in the specific heat data of sample-J.

5.5 Discussions of Results

5.5.1 Critical Spin Fluctuations in MnSi

We presented in Sec. 3.2.2 a theoretical description of the critical fluctuations in the mean-field approximation that correctly tackles the symmetry of the problem but cannot describe the temperature dependence of the relevant quantities. If one neglects the anisotropic exchange interaction the theory predicts a first order transition [42]. However, apparently, our SANS data are consistent with a second order phase transition. Therefore we estimate the corresponding critical exponents. We tried to improve Eq. 3.19 by replacing the mean-field expression for κ^2 by $\kappa^2 = C_1\tau^{2\nu}$, where $\tau = (T - T_c)/T_c$ and ν is the exponent for the correlation length for q along $\langle 111\rangle$ (easy direction). The corresponding result is shown in Fig. 5.15 with $\nu = 0.62(1)$.

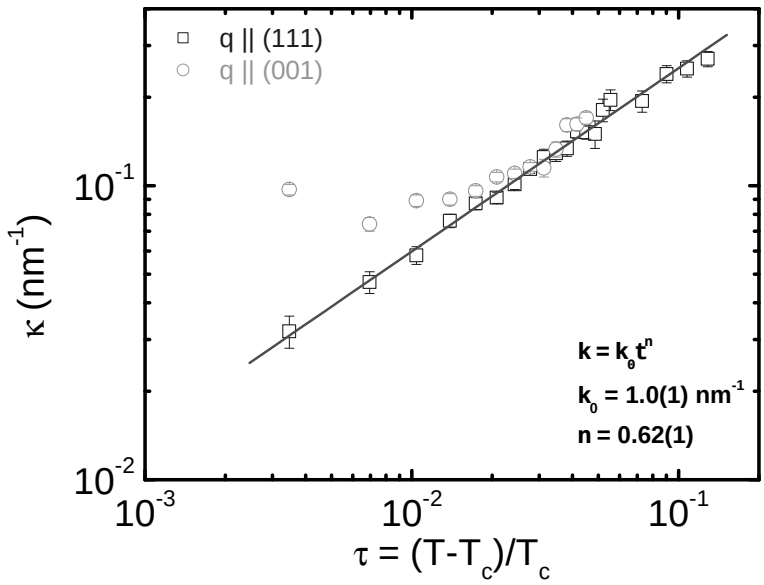

Figure 5.15: Temperature dependence of the inverse correlation length for $q \parallel \langle 001\rangle$ and $q \parallel \langle 111\rangle$ [30].

Maleyev [40, 29, 31] proposed that if q deviates from $\langle 111\rangle$ the correlation length is renormalized according to $\kappa^2 - \kappa^2_{(111)} \propto (Inv)^\lambda$ where $Inv = (\hat{q}^4 - 1/3)$ is the cubic

invariant and λ is the critical exponent for the cubic anisotropy. In Fig. 5.16 we plotted the anisotropic contribution to the inverse correlation length as function of $Inv = \hat{q}^4 - 1/3$. We obtain the value $\lambda = 0.22(5)$.

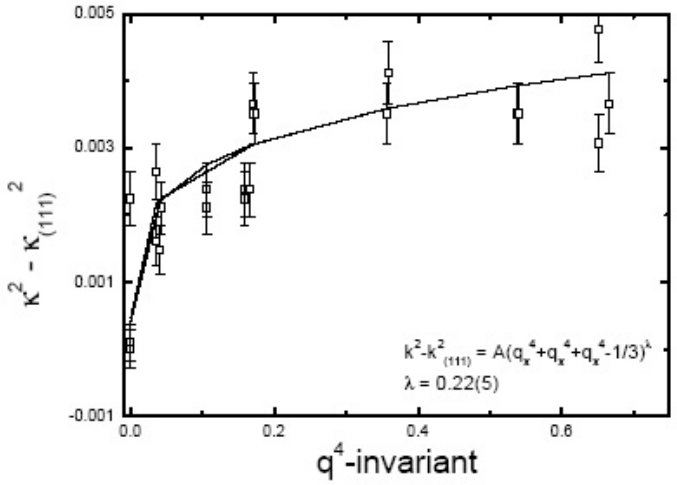

Figure 5.16: The difference of the square of the inverse correlation lengths $\kappa^2 - \kappa^2_{(111)}$ as function of $\hat{q}^4$.

We integrated the intensities along a ring of constant q for both polarizations independently (i.e. the integration is performed along the half moon of $180°$) and the intensity is plotted against q for different temperatures. The resulting structure at each temperature is fitted with a Lorentzian peak.

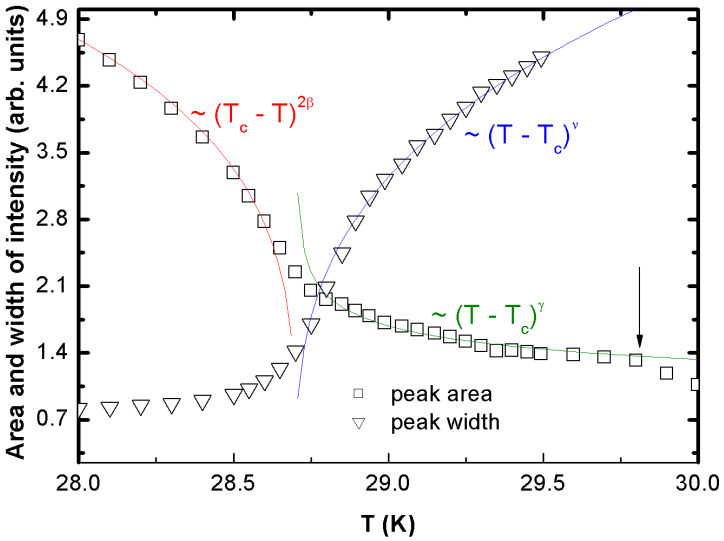

Figure 5.17: Area of the peak intensity as obtained by fitting the data with a Lorentzian. Solid lines are fits to the data using $A_0(T_c - T)^{2\beta}$ below T_c and $A_1(T - T_c)^{\gamma}$ above T_c.

As the intensity of scattering in the ordered phase is proportional to the square of the magnetization, we get the critical parameter 2β for $T \leq T_c$ by fitting the area of Bragg intensity (see Fig. 5.17) with $A = A_0(-\tau)^{2\beta}$. For MnSi we obtained $2\beta = \beta_c = 0.44(1)$. The value of β is surprisingly low for the 3D magnetic system but it is close to that found in the frustrated $CsMnBr_3$ ($\beta_c = 0.43(2)$) compound, which belongs to the chiral universality class [89, 90].
Above T_c the scattering intensity (see Fig. 5.17) is directly proportional to the staggered susceptibility ($\chi \propto \tau^{\gamma}$). Therefore we can derive the critical exponent γ for $T \geq T_c$ directly from the intensity plot in Fig. 5.17. We obtain a value of $\gamma = 0.61(1)$ which is smaller than the corresponding value of a 3D Heisenberg ferromagnet typically between $\gamma = 1.3$ and 1.4. For the chiral universality class the value of $\gamma_c = 0.77$ is predicted in [14].
It should be noted that beyond the mean field theory the critical behaviour must have two crossovers.

(i) At $q \gg k$ one can neglect the Dzyaloshinskii-Moriya interaction and the anisotropic exchange interactions as in itinerant ferromagnets.

(ii) For $k \sim q$ the Brasovskii theory [42], neglecting anisotropic exchange interaction, should be applicable. Furthermore, for small $(q-k)^2$ and very close to the transition one can neglect the $(q-k)^2$ terms in Eqs. 2.43 and 3.19 and we will get a behaviour determined by the singular properties of $1/Inv$, which goes to infinity as q approaches the cubic diagonals. So if $q \to k$, an additional renormalization group analysis must be done.

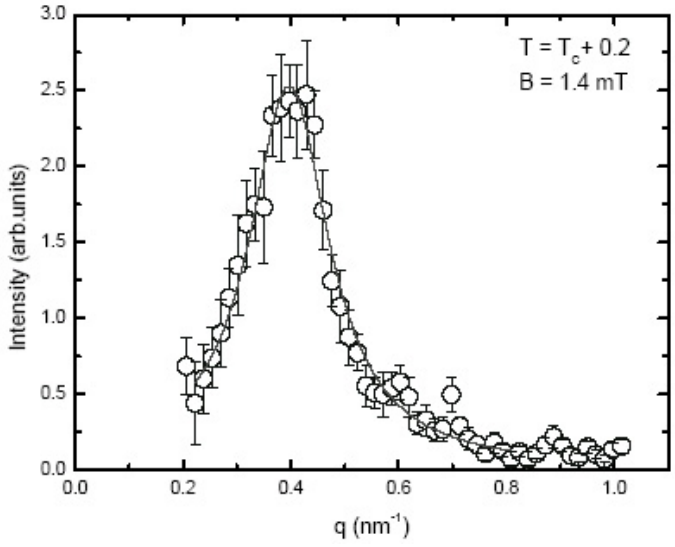

Figure 5.18: q scan of the intensity across the ring in easy direction at $T = T_c + 0.3$ K. The solid line is best fit result of Eq. 3.19 with $k = 0.39\,\mathrm{nm}^{-1}$ and $\kappa = 0.055\,\mathrm{nm}^{-1}$.

The q dependence of the intensity above T_c as depicted in Fig 5.18 is very well described by Eq. 3.19 (solid line). Therefore the parameters J, D_m and A_m of the theory are estimated. J may be given approximately as $a^2 T_c \approx 50\,\mathrm{meV\AA}^2$. This estimation is close to

the spin-wave stiffness $D \approx 52\,\text{meVÅ}^2$ obtained from inelastic neutron scattering [75]. Further the helix wave vector $k = D_m/J = 0.039\,\text{Å}^{-1}$ for the critical range and therefore $D_m = 1.9\,\text{meVÅ}$ and $D_m a \approx 8\,\text{meVÅ}^2$. Finally according to Eq. 2.43 the inverse correlation length in the hard direction is determined by $\kappa^2 = k^2|A_m|/(2J)$. From Fig. 5.15 we get $\kappa_{\langle 100\rangle} \approx 0.008\,\text{Å}^{-1}$ and $A_m = 4\,\text{meVÅ}^2$. Hence the inequality $J > D_m a > A_m$ as assumed by the theory [40, 29, 31] holds at least in rough approximation.

5.5.2 New Magnetic Phase Transitions in MnSi?

From the specific heat data (sample-J) at zero field we estimate the temperature dependence of the entropie associated with the magnetic ordering according to $S = \int_2^{T \gg T_c} \frac{C}{T} dT$. Shown on Fig. 5.19 is the entropie S versus temperature. A change of slope at $T = T_c$ and $T = T^\star$ one degree above T_c give indications that phase transitions may exist occuring at these temperatures. The value of $T^\star$ may be qualitatively related at to the temperature value where the scattering intensity of the ring is dissolved (see Fig. 5.14).

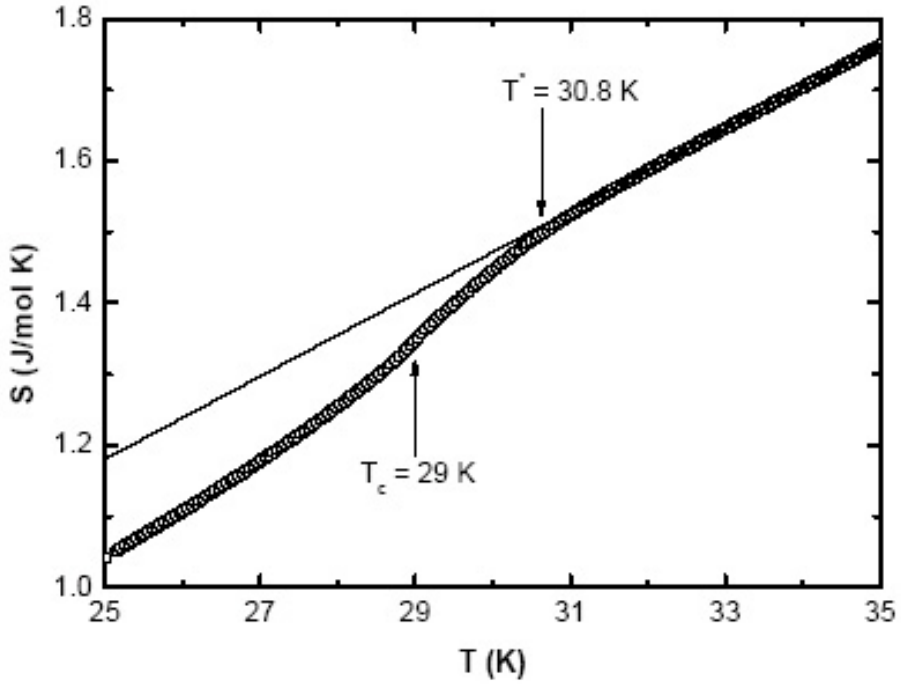

Figure 5.19: Temperature dependence of the entropie as estimate from specific heat data from sample-J. Arrows indicate temperatures where the slope of S changes. The solid line is a linear fit to data above $T = 30.9\,\text{K}$. A change of slope is observed at the temperatures ($T = 29\,\text{K}$ and $T = 30.9\,\text{K}$) marked by the arrows.

However to understand the nature of the shoulder in the specific heat and the kink in the staggered susceptibility both observed above T_c we compare in Fig. 5.20 data of specific heat with SANS both obtained from sample-A.
The temperature value where the shoulder appears in the specific heat coincide with the position of a kink in staggered susceptibility. Therefore the shoulder in the specific heat

is most likely connected with our small angle neutron scattering results. We conclude that the peak in the specific heat at T_c is not entirely due to the transition from the paramagnetic phase to the helical phase, but may correspond to an additional transition in MnSi.

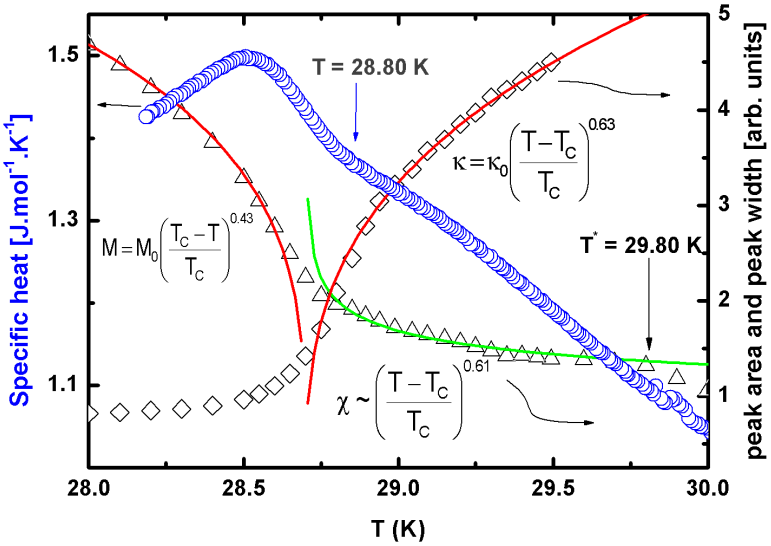

Figure 5.20: Comparison of magnetic specific heat data with the staggered susceptibility obtained from SANS measurements. Both experiments were performed on sample-A. Error bars are smaller than the symbol size.

5.6 Summary

Results of bulk measurements and those of polarized neutron small angle scattering in MnSi, a cubic itinerant magnet, are presented and analyzed. The diffuse scattering intensity looks like half-moons oriented along the incident neutron polarization. The intensities for two opposite polarizations form an anisotropic ring with weak spots, which below T_c transform into the Bragg peaks originating from the helical structure. These results are in semiquantitative agreement with the mean-field calculations based on the Bak-Jensen model [24] that takes into account the hierarchy of the interactions: the exchange interaction, the isotropic Dzyaloshinskii-Moriya (DM) interaction and the weak anisotropic exchange (AE) interaction. The DM interaction is responsible for the scattering intensity concentrated in the half moons. The AE interaction provides the anisotropy so that the correlation length diverges only along $\langle 111 \rangle$ with a corresponding critical exponent $\nu = 0.62(1)$. The chiral exponent of the intensity due to the helical structure at $T < T_c$ is $\beta_c = 0.44(1)$. This value is close to that found in $CsMnBr_3$ compound which belongs to the chiral universality class [89, 90].
Furthermore the specific heat at zero field shows a sharp peak at T_c and a broad shoulder with increasing temperatures. Combining bulk measurements with SANS data, we found an indication of an additional phase transition in MnSi. To conclude, we have a quali-

tative understanding of the critical fluctuations in MnSi but further investigations, both theoretical and experimental are demanding to answer the question whether an additional transition exists above T_c in MnSi.

Chapter 6

Effect of Magnetic Field on the Magnetic Structure of MnSi

In these matters the only certainty is that nothing is certain.
Pliny the Edler

6.1 Introduction

In an external magnetic field the wave vector $\vec{k}$ rotates towards the field direction (wave vector rotation effect) but the value of $\vec{k}$ remains unchanged [70]. This rotation takes place within a field range from 0 to 130 mT. Shown in Fig. 6.1 is the rotation of the modulation vector toward the direction of the field. The bahaviour looks like a second order phase transition with a critical field about 0.17 T [32]. Bak and Jensen [24] predicted within the renormalization group theory a first order transition. Kataoka and Nakinishi [27], Plumer and Walker [25, 28] include external magnetic field and magnetic anisotropy in the Landau type free energy and use it to model the wave vector and spin reorientation in a magnetic field. They use mean field theory and expand the free energy. Hereby, they could explain the rotation of the wave vector $\vec{k}$ with a magnetic field.
Recently Walker predicted two successive wave vector reorientation phase transitions in MnSi [28]. In this part of the thesis, we study the magnetic behavior of MnSi in the presence of an external magnetic field using SANS, AC susceptibility and specific heat measurements.
We measured the scattering intensity in the temperature range from $T = 10$ K to $T = 30$ K. The external magnetic field ($B < 800$ mT) was applied perpendicular to the incident beam. We study the magnetic structure of MnSi below T_c in the so called A-phase. We present results of bulk measurements and small angle polarized neutron scattering data of both critical fluctuations and the ordered magnetic structure in MnSi under applied magnetic field and at ambient pressure. The magnetic field applied along the $\langle 100 \rangle$, $\langle 110 \rangle$ and $\langle 111 \rangle$ direction produces an single domain sample with the spin oriented along the field direction. The observed field induced instability is especially pronounced near T_c in the presence of a magnetic field.

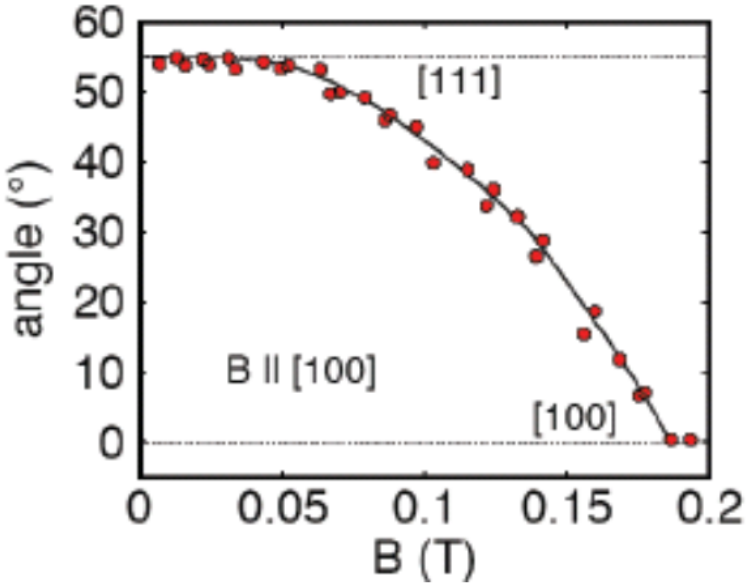

Figure 6.1: Angle θ between the modulation vector $\vec{k}$ and the direction of the applied field at $T = 4.2\,\mathrm{K}$ in MnSi as function of external magnetic field [32].

6.2 Experimental Details

For the bulk measurements as well as for the neutron scattering experiments we use both MnSi samples that have been described in chapter 5.
We measured the AC susceptibility of MnSi (sample-J) as function of temperature and magnetic field up to $1\,\mathrm{T}$. Measurements were carried out on the 9T Quantum Design Physical Properties Measurement System. The magnetic field was applied in the three main crystallographic direction of interest namely the $\langle 100\rangle$, $\langle 110\rangle$ and the $\langle 111\rangle$. Since the magnetic struture of MnSi has a very complicated irreversible type of behaviour in the presence of a magnetic field, each experiment (bulk experiments and neutron scattering) is performed according to the following sequence: (i) the sample was cooled down to $20\,\mathrm{K}$ from a temperature above $35\,\mathrm{K}$. (ii) field sweep from $B = 0$ to the field value of interest. (iii) The direction of the magnetic field is fixed with respect to the chosen crystallographic direction. The magnetic mosaic of both samples was measured at $T = 10\,\mathrm{K}$. A value of $\Delta\theta_{mag} \approx 4^\circ$ for the magnetic mosaic is obtained. First it should be noticed that the magnetic mosaic is larger than the mosaic of the crystallographic structure that is $\Delta\theta = 0.22^\circ$ for sample-A and $\Delta\theta = 0.21^\circ$ for sample-J as presented in chapter 5.
We choose the same instrumental configuration as for SANS experiments in zero field (see chapter 5).

6.3 Results of Experiments

6.3.1 Bulk Measurements

DC Magnetization

DC magnetization measurements were performed using sample-A of MnSi. Fig. 6.2 displays magnetization measurements in fields up to 1 T over a wide temperature range. A small spontaneous moment $\mu_S \approx 0.45\mu_B$ per manganese atom develops for temperatures $T < 29\,\mathrm{K}$. The magnetization is consistent in rough approximation with the well known magnetic equation of state $B = aM + bM^3$, where a and b are constants [91].

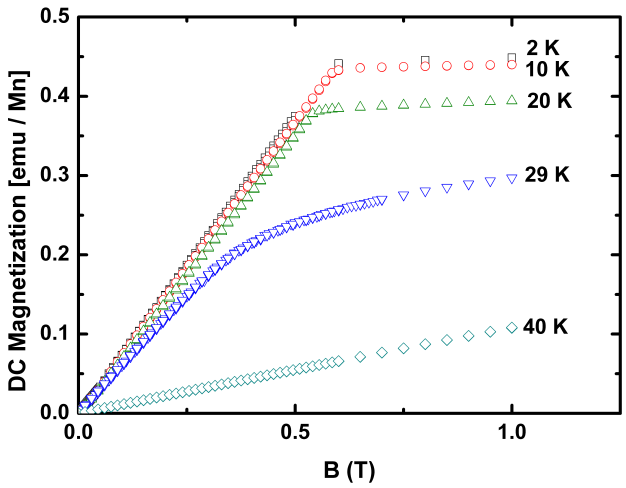

Figure 6.2: Magnetization of MnSi (sample-A) at various temperatures for a magnetic field applied along the $\langle 110 \rangle$ crystallographic direction. Error bars are smaller than the symbol size.

Shown in Fig. 6.3 are temperature and field dependence of the DC magnetization of MnSi in magnetic fields varying from $B = 0.1\,\mathrm{mT}$ to $B = 1\,\mathrm{T}$. A pronounced peak appears at $T = 28.80 \pm 0.02\,\mathrm{K}$ at low external magnetic fields $B \leq 10\,\mathrm{mT}$ corresponding to a transition from the paramagnetic phase into the helically ordered phase. For magnetic fields $B > 10\,\mathrm{mT}$ the peak magnitude decreases and finally disappears at fields $B \geq 0.1\,\mathrm{T}$. A ferromagnetic behavior of the susceptibility is observed with increasing magnetic fields. These results suggest that the field induces a transition to the ferromagnetic phase by causing the helix to collapse to a fully aligned ferromagnet. Between $B = 0.15\,\mathrm{T}$ and $B = 0.2\,\mathrm{T}$ a considerable increase of the susceptibility is noted below T_c.

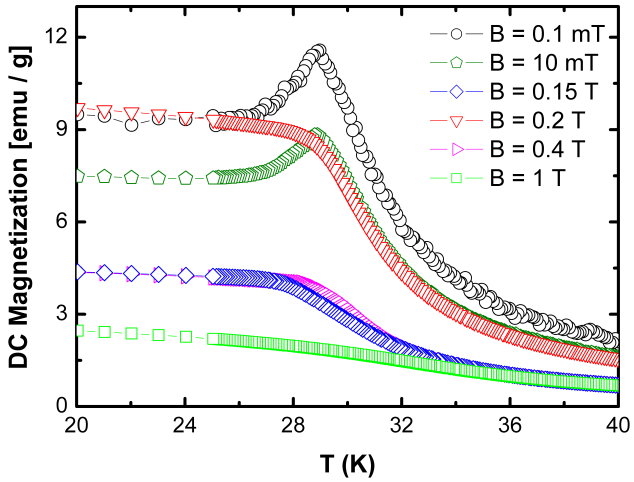

Figure 6.3: Temperature and field dependence of the DC magnetization of MnSi (sample-A) in fields applied along a $\langle 110 \rangle$ direction. Error bars are smaller than the symbol size.

AC Susceptibility

All the AC susceptibility data presented here were carried out on sample-J. The field dependence of the AC susceptibility at fixed temperatures up to $40\,\mathrm{K}$ is shown on Figs. 6.4, 6.5 and 6.6 for the magnetic field was applied along $\langle 100 \rangle$, $\langle 110 \rangle$ and $\langle 111 \rangle$, respectively. As the temperature approaches T_c from below, the AC susceptibility at $B = 0.2\,\mathrm{T}$ revealed an abrupt change of slope and a minimum in the field range $B_{A1} < B < B_{A2}$. Typical AC-susceptibility data in the A-phase are observed close to T_c at $T = 28.5\,\mathrm{K}$ for $B \parallel \langle 100 \rangle$, $B \parallel \langle 100 \rangle$ and $B \parallel \langle 111 \rangle$. These results are used to determine the field boundaries of the A-phase.

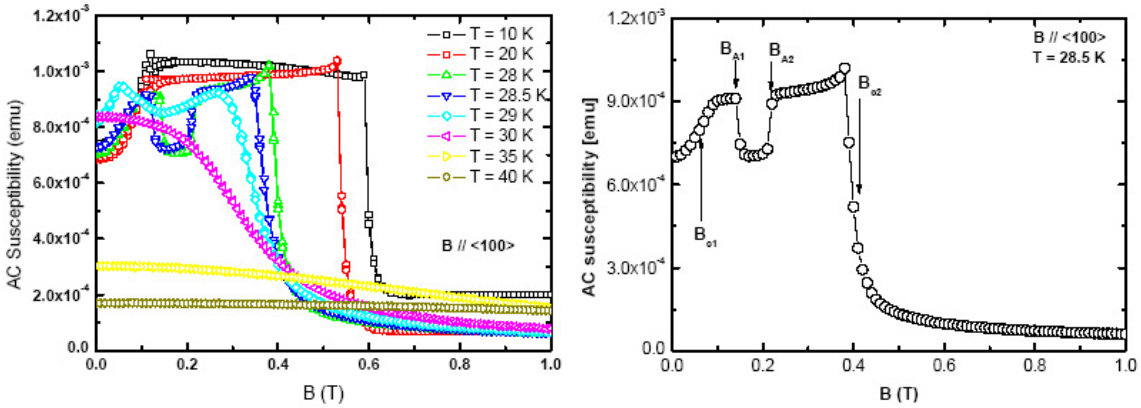

Figure 6.4: Field dependence of the AC susceptibility of MnSi (sample-J) when a magnetic field B is applied along $\langle 100 \rangle$ at various temperatures. Below T_c (at $T = 28.5\,\mathrm{K}$) an abrupt change of slope and a minimum is also observed that is characteristic in the A-phase.

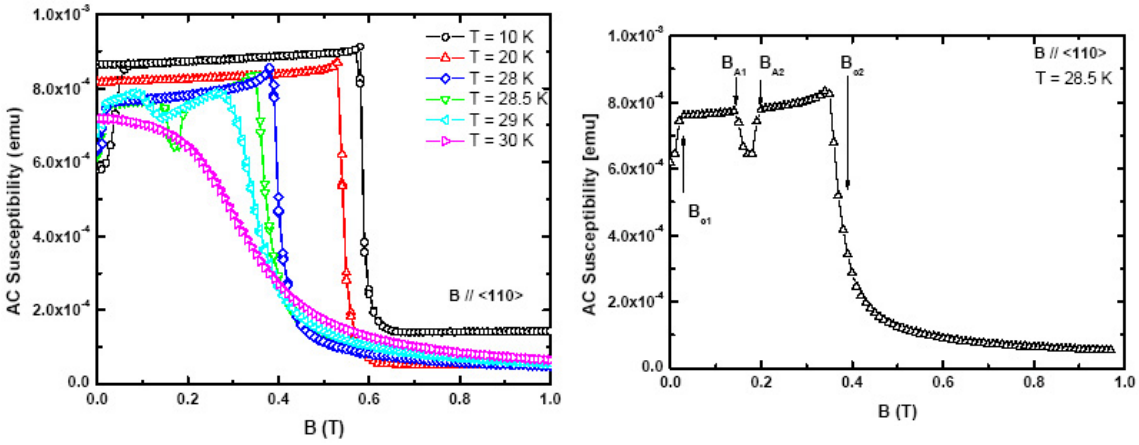

Figure 6.5: Field dependence of the AC susceptibility of MnSi (sample-J) when a magnetic field B is applied along $\langle 110 \rangle$ at various temperatures. In a magnetic field of $0.2\,\mathrm{T}$ at $T = 28.5\,\mathrm{K}$ an abrupt change of slope and a minimum is also observed that is characteristic in the A-phase

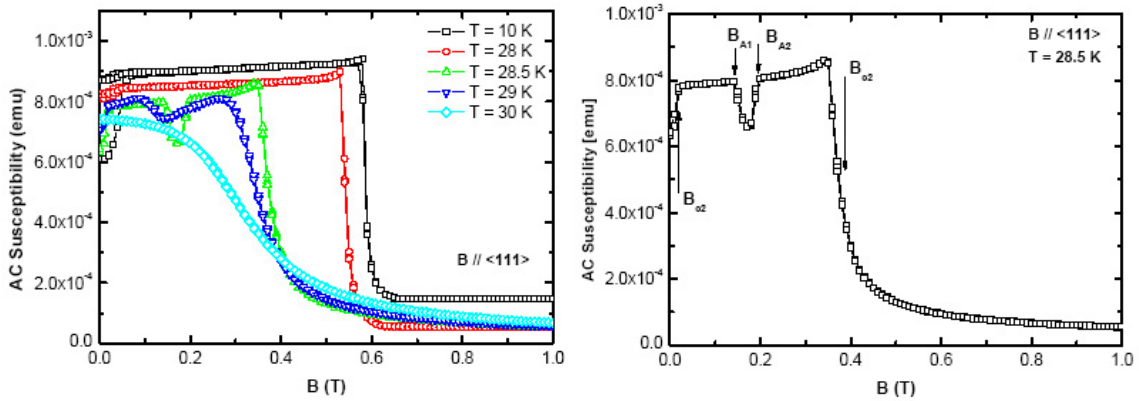

Figure 6.6: Field dependence of the AC susceptibility of MnSi (sample-J) when a magnetic field B is applied along $\langle 110 \rangle$ at various temperatures. In a magnetic field of $0.2\,\mathrm{T}$ at $T = 28.5\,\mathrm{K}$ an abrupt change of slope and a minimum is also observed that is characteristic in the A-phase

Fig. 6.7 displays the temperature dependence of the AC susceptibility at different magnetic field in the range $0 < B < 1\,\mathrm{T}$. An abrupt change of slope and a minimum is also observed that is characteristic in the A-phase. These discontinuities can be used to determine the temperature boundaries of the A-phase. At magnetic fields above $0.5\,\mathrm{T}$ a broad maximum appears at T_m and is shifted to higher temperatures as the field increases.

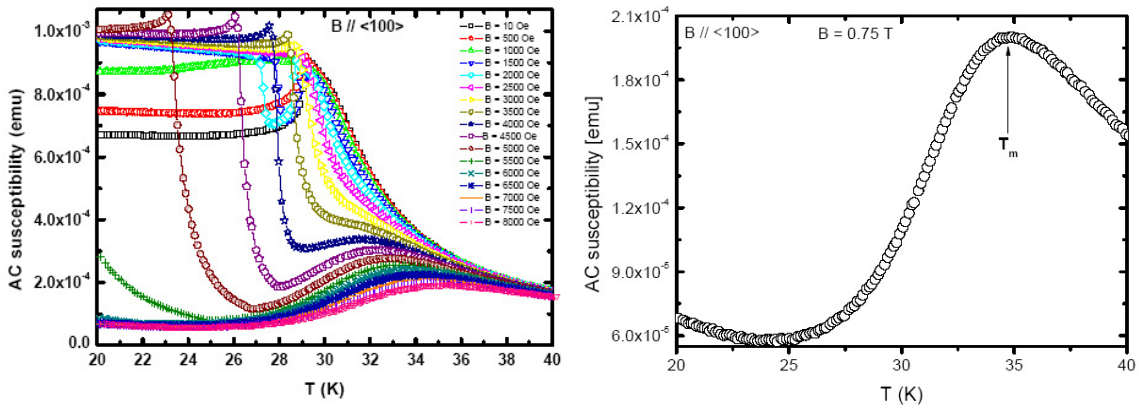

Figure 6.7: Temperature dependence of the AC susceptibility of MnSi (sample-J) using various magnetic field $B \parallel_s \langle 100 \rangle$. With increasing temperature, a broad maximum denoted T_m appears above the critical temperature. It is shifted to higher temperatures as the field increases. Below T_c an abrupt change of slope and a minimum is observed for $B = 0.2\,\mathrm{T}$.

The onset of the minimum measured in Figs. 6.4 and 6.5, 6.6 and 6.7 has been mapped out as function of temperature and is shown in the phase diagrams in Fig. 6.8. The temperature region of the A-phase is different for magnetic fields applied along the three crystallographic directions ($B \parallel \langle 100 \rangle$, $B \parallel \langle 110 \rangle$, and $B \parallel \langle 111 \rangle$). The A-Phase is observed in the temperature range $T = 27.3\,\mathrm{K} \leq T \leq T_c$ for $B \parallel \langle 100 \rangle$ while for $B \parallel \langle 110 \rangle$ and $B \parallel \langle 111 \rangle$ the A-phase appears for $T = 28.3\,\mathrm{K} \leq T \leq T_c$ and $T = 28.4\,\mathrm{K} \leq T \leq T_c$, respectively.
Our data agree with previous studies of the magnetization [88] and AC susceptibility [92].

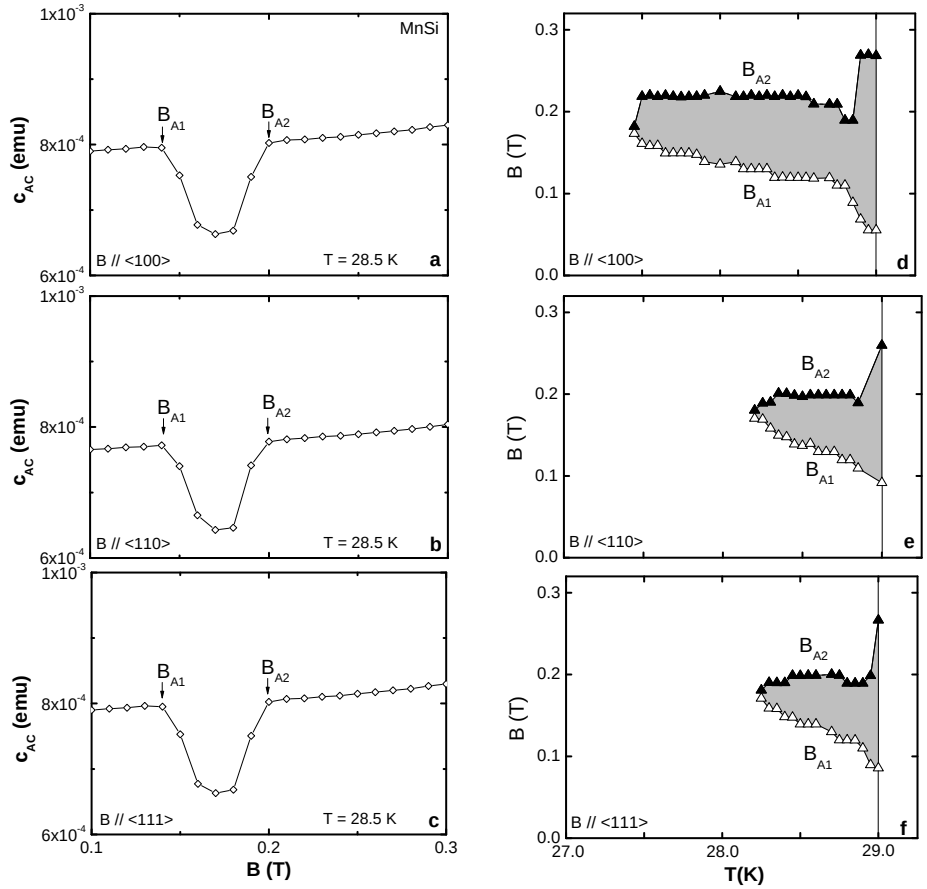

Figure 6.8: Phase boundaries of the so called A-phase in MnSi (sample-J) below T_c for $B \parallel \langle 100 \rangle$, $B \parallel \langle 110 \rangle$, and $B \parallel \langle 111 \rangle$. The onset values B_{A1} and B_{A2} (Left Panel) has been mapped out for different temperatures. The resulting phase diagrams are depicted in the Right Panel.

Magnetic Specific Heat

Fig. 6.9 shows the specific heat C of MnSi (sample-J) as function of temperature for various magnetic fields applied along the $\langle 100 \rangle$ direction. At zero field a sharp peak and a shoulder is seen. Remarkably, as the magnetic field increases to $0.15\,\mathrm{T}$ and $0.18\,\mathrm{T}$, an additional small maximum marked by an arrow emerges at the low temperature side of the major peak of C. These maxima indicate a well-defined transition at the border of the A-phase as well. At a field higher than $0.18\,\mathrm{T}$ the shoulder disappears.

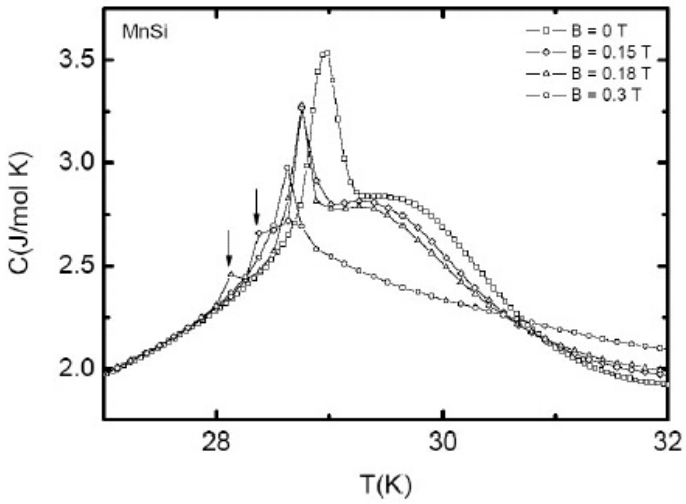

Figure 6.9: Specific heat C of MnSi (sample-J) as function of temperature for magnetic fields $B = 0$ and $B = 0.15, 0.18$ and 0.3 T. A small anomaly marked by arrows signals the onset of the A-phase and indicates a distinct thermodynamic transition.

6.3.2 Small Angle Polarized Neutron Scattering from MnSi

A typical behavior of the magnetic spirals is shown in Fig. 6.10 for the geometry when the field is applied along the $\langle 110 \rangle$ direction in sample-A. These data gives the maps of diffraction peaks in a logarithmic scale and how it changes with the magnetic field.

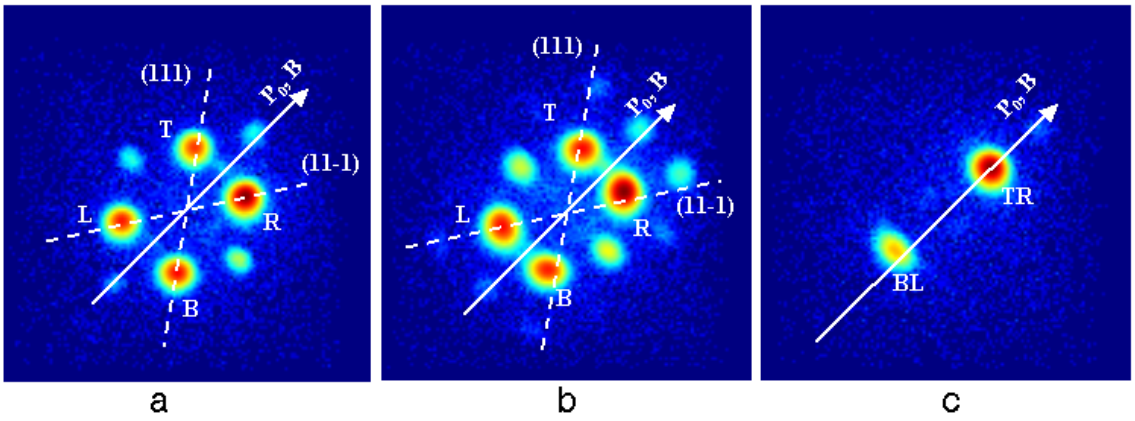

Figure 6.10: The two dimensional diffraction spectrum measured on SANS-2 (GKSS) in a logarithmic scale at $T = 10$ K for magnetic fields $B \parallel \langle 110 \rangle$ for $B = 1.4$ mT (a), $B = 50$ mT (b) and $B = 150$ mT (c).

The contour map at $B = 1.4$ mT and $T = 10$ K shows four major and four minor peaks. Four major peaks(closest to the center) are the Bragg reflections for those domains of spirals, which are collinear to the axes $\langle 111 \rangle$ and $\langle 11-1 \rangle$ visible in this geometry of the experiment. Observation of two peaks at $\pm q$ is explained by the mosaic of the magnetic structure which is larger than crystallographic one of MnSi. We denote these four peaks

as Left(L), Bottom (B), Right (R) and Top (T), respectively. Additional small peaks at $q = q_L + q_B$, $q = q_R + q_T$ and $q = q_R + q_B$ may be a result of a double scattering process. When a relatively small magnetic field is applied ($B \leq 130\,\mathrm{mT}$), new small peaks at $q = 2q_L$, $q = 2q_R$, $q = 2q_B$ and $q = 2q_T$ arise as a response to the magnetic field as shown in Fig. 6.10b. The peaks move also toward the direction of the magnetic field, so that the direction of the scattering vector $\vec{q}$ changes but its value $|q|$ remains constant. When the field exceeds the value $B = 130\,\mathrm{mT}$, the peaks collapse to the direction of the magnetic field $\vec{q} \parallel \vec{B}$, so that only two major peaks are left on the contour map as display in Fig. 6.10c. These results agree with those reported in [32].
Fig. 6.11 illustrates the rotation of the spiral toward the magnetic field direction by means of a polar representation.

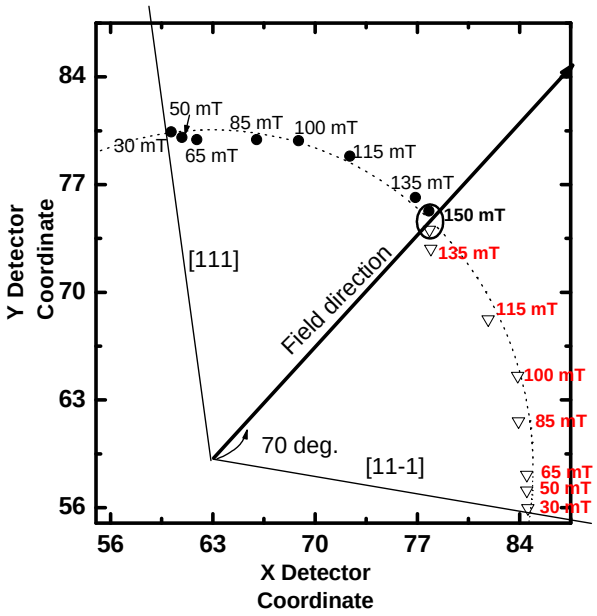

Figure 6.11: Schematic representation of the spin and wave vector rotation toward the field direction. The points are the positions of the peaks at pointed magnetic field.

Small-angle neutron scattering data at various temperatures and magnetic fields are shown in Figs. 6.12 6.13 and 6.14 as obtained from sample-J with magnetic fields applied along the $\langle 100 \rangle$, $\langle -121 \rangle$ and $\langle 111 \rangle$, respectively. At temperatures below T_c, we observe well defined spots of helical magnetic order as reported in numerous studies before.
With increasing magnetic field for example along $\langle 100 \rangle$, we observe as an additional feature a ring of scattered intensity for $T = 28.5\,\mathrm{K}$ with a radius corresponding to $|q| = 0.39\,\mathrm{nm}^{-1}$ that was not present at $B = 0$.
The appearance of this ring of intensity is only gradual when going from $B = 0$ into the A-phase. The distinct change of slope of the AC susceptibility as well as the sharp peaks in the specific heat indicate a well defined phase transition into the A-phase that shows up in the SANS-experiments as a ring of scattering intensity. Interestingly, we observe

the same qualitative behavior for the field applied in the three main directions of interest namely for $B \parallel \langle -121 \rangle$ as depicted in Fig. 6.13 and for $B \parallel \langle 111 \rangle$ as shown in Fig. 6.14. Therefore, the behavior is isotropic and not related to a particular initial direction of the helical order that is enforced at low T by anisotropies enforced by the lattice.

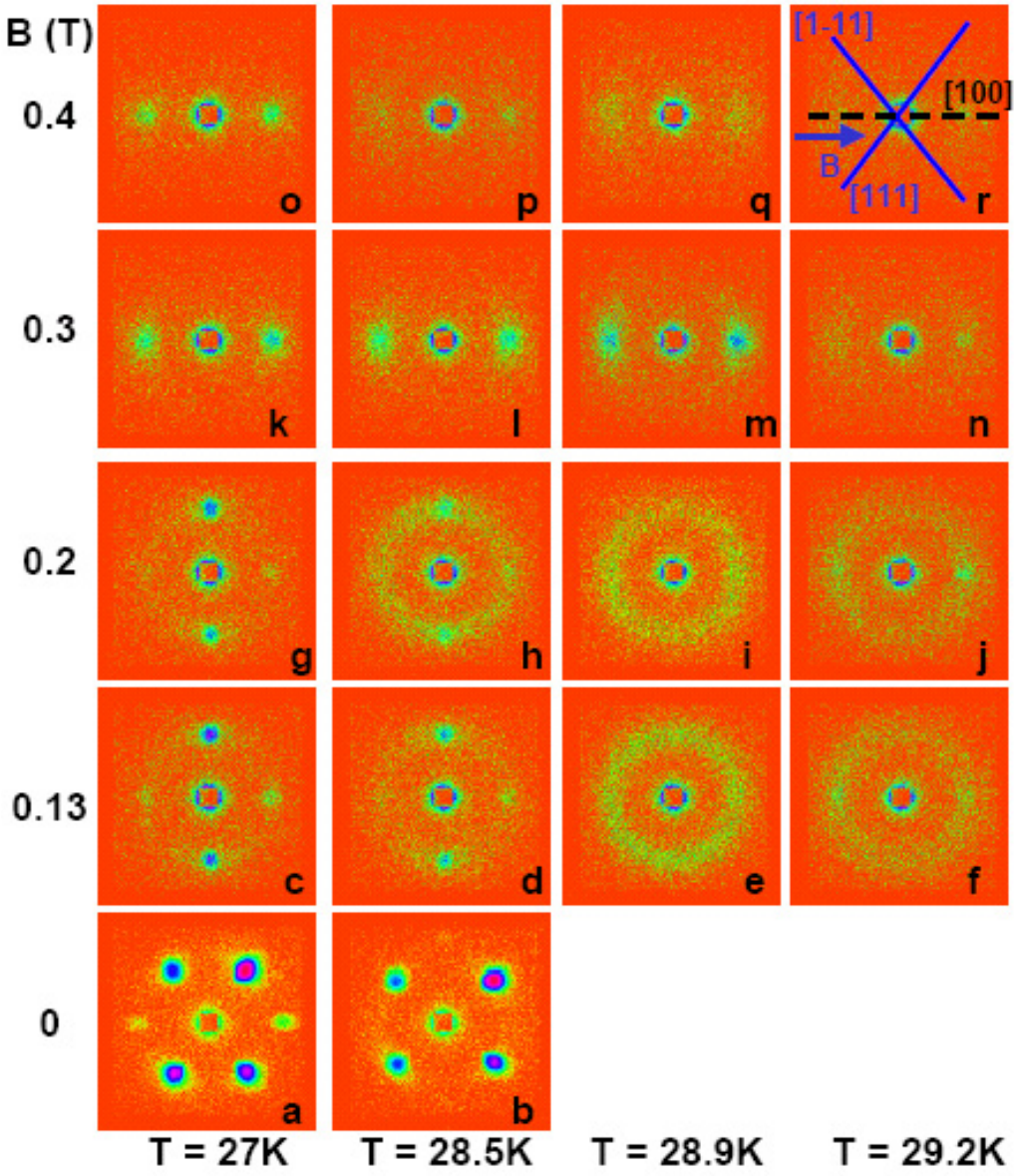

Figure 6.12: Neutron SANS intensity of MnSi (sample-J) as function of temperature and magnetic field as recorded at the diffractometer SANS-2 in Geesthacht. A ring of scattering intensity is visible in the A-phase. The field was applied along the $\langle 100 \rangle$. Data at zero field for $T = 28.9\,\mathrm{K}$ and $T = 29.2\,\mathrm{K}$ are missing.

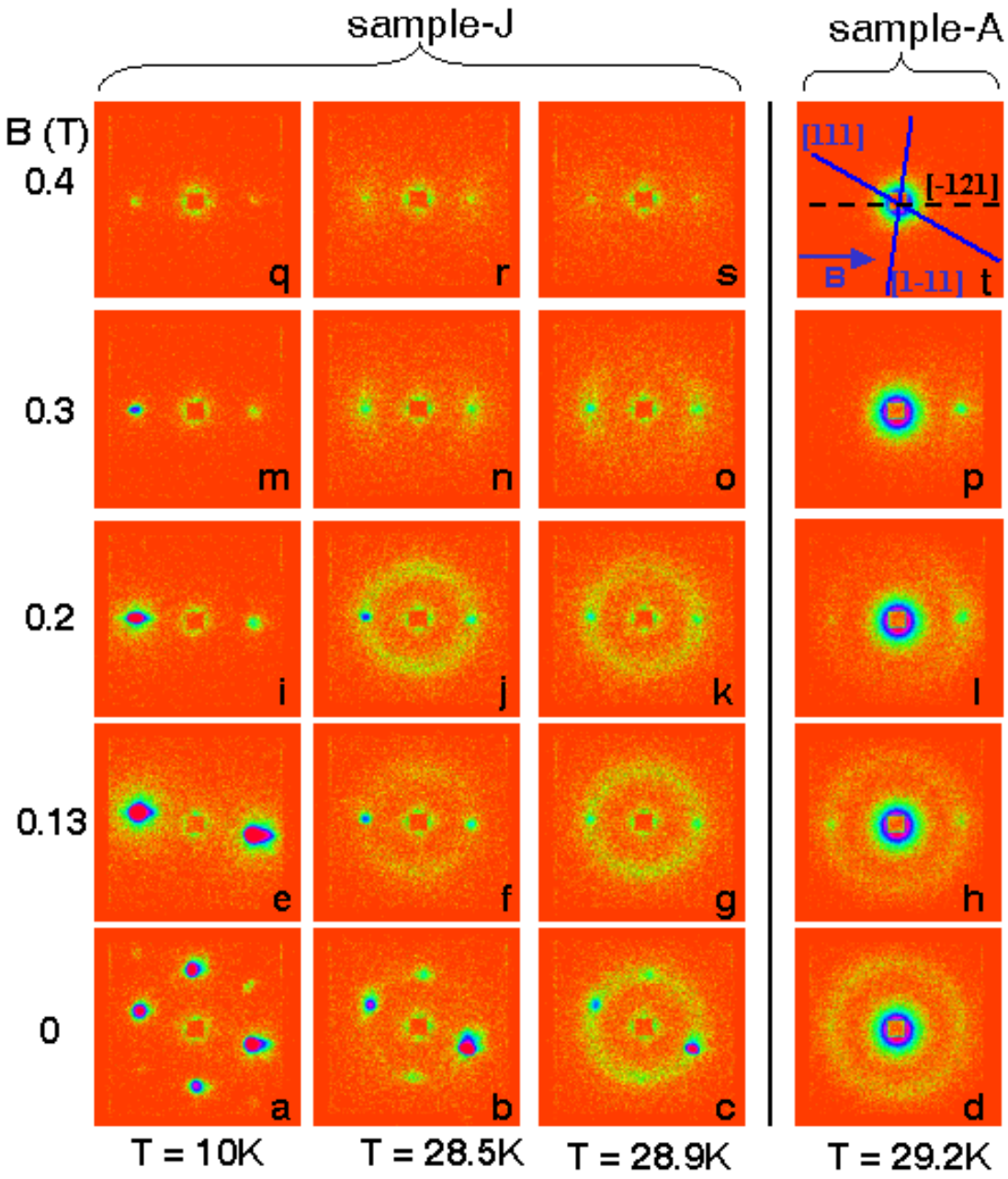

Figure 6.13: Neutron SANS intensity of MnSi as function of temperature and magnetic field as recorded at the diffractometer SANS-2 in Geesthacht. Sample-A was used for experiments below T_c. Four resolution-limited spots are characteristic of long-range helical order are seen at $T \ll T_c$, consistent with previous work. A ring of scattering intensity is visible in A-phase. The field was applied along the $\langle -121 \rangle$. The data for $T > T_c$ are separated with a black line from data below T_c because they are obtained from an experiment on the sample-A.

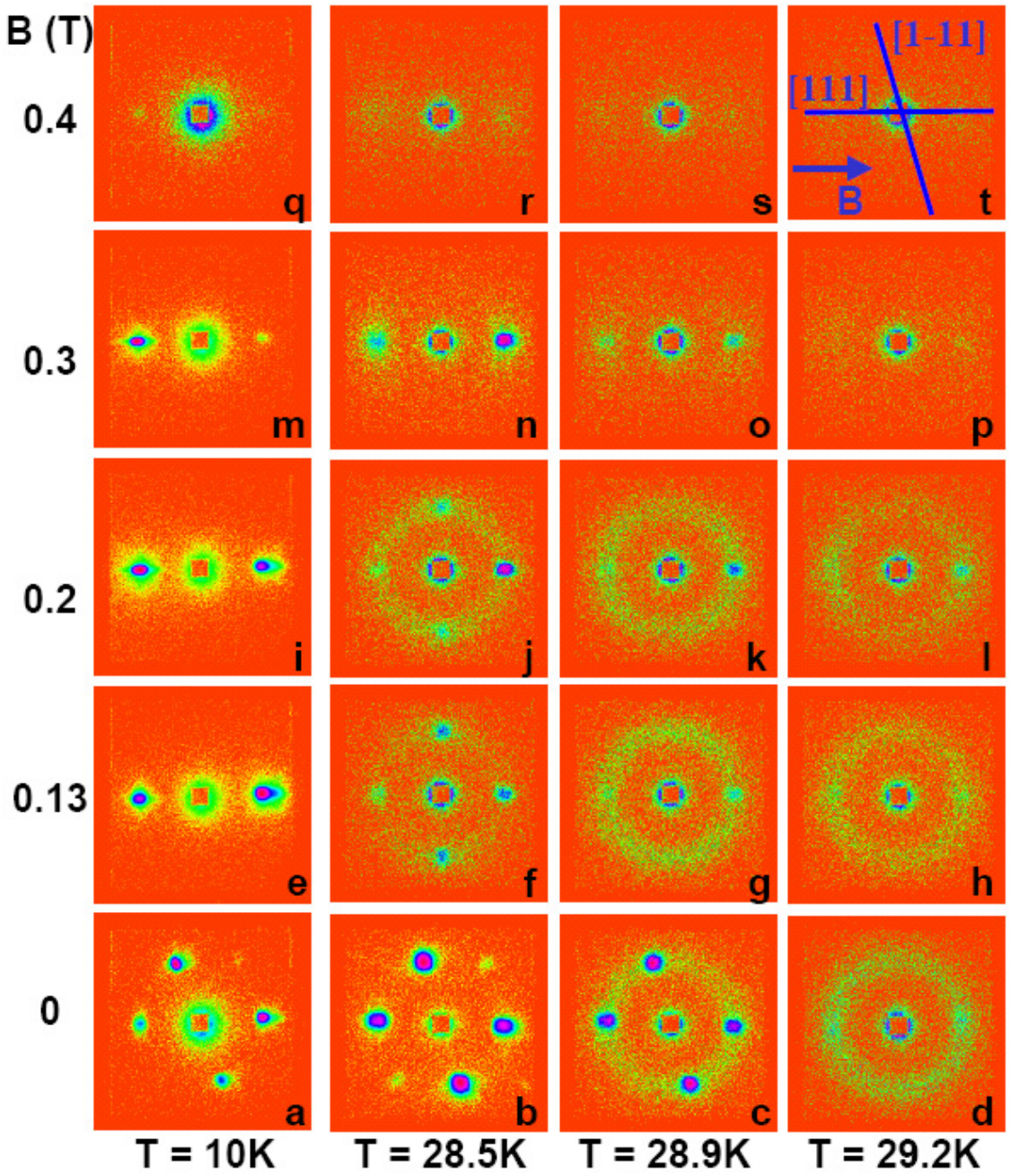

Figure 6.14: Neutron SANS intensity of MnSi(sample-J) at temperatures above and below T_c as recorded at the diffractometer SANS-2 in Geesthacht. Four resolution-limited spots are characteristic of long-range helical order are seen at $T \ll T_c$, consistent with previous works. A ring of scattering intensity is visible in the A-Phase. Out of the A-Phase the intensity is dissolved to the background. The field was applied along the $\langle 111 \rangle$ direction.

The integrated intensity as function of the azimuthal angle and the magnetic field at fixed $T = 28.85\,\mathrm{K}$ and in the A-phase for $B \parallel \langle 111 \rangle$ is displayed in Fig. 6.15.These measurements were carried out at the new diffractometer MIRA at FRM-II. At zero field four well defined magnetic Bragg peaks are observed at azimuthal angles $-160°$, $-99°$, $27°$ and $99°$. The helices are originally oriented by the crystallographic anisotropy along the $\langle 111 \rangle$ directions. With increasing field, $\vec{q}$ is aligned gradually along the external field $\vec{B}$. For $B = 98\,\mathrm{mT}$ the peaks collapse to the applied field direction and only two peaks are observed at $\pm 99°$. The peaks at $-160°$ and $27°$ disappear completly. In the field range $140\,\mathrm{mT} \leq B \leq 350\,\mathrm{mT}$ corresponding to the A-phase, the sharp peaks become broader and a ring of intensity is visible.

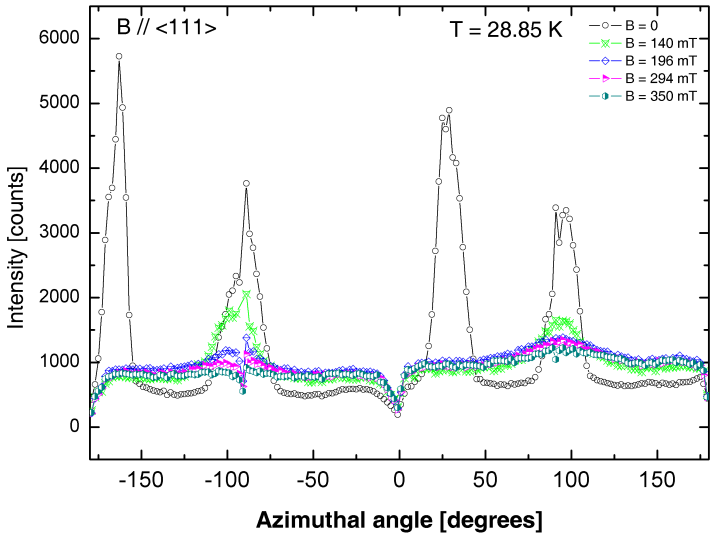

Figure 6.15: Integrated intensity as function of magnetic field and azimuthal angle of MnSi (sample-J) at $T = 28.85\,\mathrm{K}$ as measured on the diffractometer MIRA (FRM-II). The field is applied along the $\langle 111 \rangle$. The sharp peaks become broader due to the applied magnetic field and a ring of intensity is visible in the A-phase region. Going beyond $300\,\mathrm{mT}$ the peaks disappear in the field induced ferromagnetic phase. Due the artefact of the detector system the intensity is zero for the angles $0°$, $-180°$.

6.4 Discussion of the Results

6.4.1 Spin and Wave-vector Reorientation below T_c

We analyse the neutron scattering data shown in Fig. 6.10 for the polarization directed along $[I(q, P_0)]$ and opposite $[I(q, -P_0)]$ to the magnetic field. We parametrised the data using $P_A = \Delta I(q)/I(q)$, where $\Delta I(q) = [I(q, P_0) - I(q, -P_0]$ and $I(q) = [I(q, P_0) + I(q, -P_0]$.
The integral intensities for the top, right, bottom and left peaks are shown in Figs. 6.16a

and b respectively as function of the magnetic field. The field dependence of the polarization is presented in Fig. 6.16c. Th position of the peaks is determined by the angle Φ between the direction of the spiral and the applied magnetic field. This angle is shown in Fig. 6.16d for two spirals. The intensities of the peaks increases with field increasing up to $130\,\mathrm{mT}$. All peaks move toward the field direction and the polarization of the peaks increases to the saturation value. The change in polarization of the peaks is related to the movement of the peaks toward the field direction. Due to high degree of the cubic symmetry it is well described by $P_p = (q_p P_0)/q_p = P_0 cos\Phi$ [93].

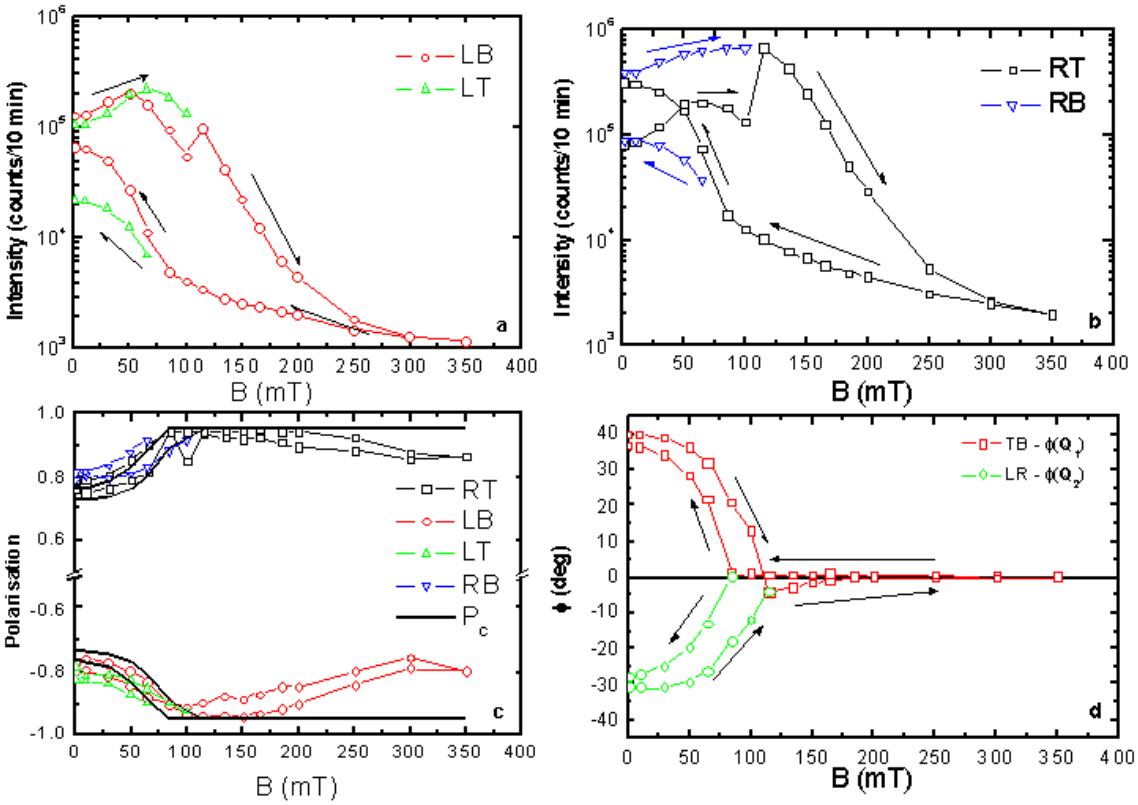

Figure 6.16: Magnetic field dependence of (a) the integral intensity of the top (T) and right (R) peaks, (b) the integral intensity of the bottom (B) and left (L) peaks, (c) the polarization of these peaks and (d) the angle Φ of their rotation at $T = 10\,\mathrm{K}$ [94].

At $B \sim 130\,\mathrm{mT}$ two peaks collapse to single one with q parallel to the direction of the magnetic field. The intensity of this united peak decreases strongly with further increase of the magnetic field and dissolves to the background value at $B_C \approx 350\,\mathrm{mT}$ as shown in Fig. 6.16a. The polarization of the peaks decreases slightly as the signal-to-noise ratio dramatically decreases in the range $130\,\mathrm{mT} < B < 350\,\mathrm{mT}$. The position of the united peaks remains unchanged. The consequent decrease of the magnetic field shows large hysteresis loop in the intensity. The peaks become separated again at $B = 80\,\mathrm{mT}$. The intensity of the peaks after applying a magnetic field differs from the intensity at zero field.

To show the properties of the magnetic transition at $B_C = 350\,\mathrm{mT}$, the field dependence of the angle Φ between the direction of the spiral and the magnetic field is shown on Fig. 6.17. The value of the angle Φ is scaled with the reduced field $b = (B - B_C)/B_C$ as $\Phi \sim b^{\epsilon}$ [28] with $\epsilon = 0.34 \pm 0.03$ for $B \parallel \langle 001 \rangle$ and $\epsilon = 0.39 \pm 0.04$ for $B \parallel \langle 110 \rangle$, what corresponds to the critical exponents of the second order phase transition.

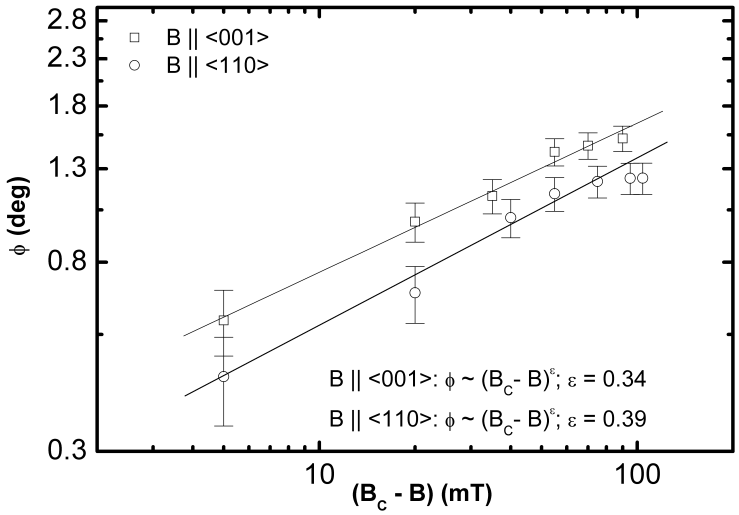

Figure 6.17: Magnetic field dependence (log-log scale) of the angle Φ between the spiral and the magnetic field that was aligned parallel to the $\langle 001 \rangle$ and to $\langle 110 \rangle$. The solid lines are fit to the data with the power law $[(B - B_C)/B_C]^{\epsilon}$.

6.4.2 Field Induced Disorder of the Helix in the A-Phase

In conventional thinking the ring may be interpreted as resulting from one of two extremes: (i) A random distribution of q-domains with well-defined helical order or (ii) a helically ordered state for which the direction of the magnetic moments changes gradually.

A possible explanation for the ring of intensity may be that random pinning potentials exist, e.g. defects, that inhibit this gradual change of orientation of long helices, causing gradual variations in orientation. However, on the basis of present day models of helical order it appears inconceivable why such pinning mechanism should only be active in a small temperature interval near T_c. This suggests, that models of reorientation transitions of helical order in a magnetic field, described for example in Ref. [28], need to be revised substantially.

We believe that an interpretation of a transition from a simple helical phase into a phase with a two- or even three-dimensional modulated texture seems to be more likely. Indeed, it is predicted that two-dimensional modulated textures (so called skyrmions) exist in a finite T-interval near T_c [95] in magnetic systems with a reduced longitudinal stiffness.

MnSi as a model system for a weak-itinerant ferromagnet that lacks inversion symmetry fits well into such a picture.

6.5 Summary

We conclude from our measurements at low temperatures and low fields that the magnetic structure of MnSi is strongly affected by the magnetic field. First, small Bragg peaks arise at $2q_L$ and $2q_B$ when the field $B \leq 130\,\mathrm{mT}$ has a component perpendicular to the helix scattering vector q_L and q_B. This demonstrates the deformation of the spiral structure and that the circular rotation of the spins is replaced by a square one. This ellipse has its longer axis along the applied magnetic field and its shorter axis perpendicular to the field. The two magnetic phase transitions at $B = 130\,\mathrm{mT}$ and $B_C = 350\,\mathrm{mT}$ were observed at low temperatures for $T = 10\,\mathrm{K}$. These transitions are related to the driving forces of the magnetic structure: (i) Anisotropic exchange energy fixing the spirals along the $\langle 111 \rangle$ directions. (ii) The isotropic DM interaction responsible for the spiral structure itself. The first transition is the orientational one when the helix axis is directed along the field. It is a first order transition with a rather strong hysteresis of the order of $40\,\mathrm{mT}$.
Our experiments show that combining SANS measurements with bulk measurements helps resolving the microscopic nature of the reorientation transition in MnSi. The results indicate the appearance of a new form of magnetic ordering that may be interpreted in terms of skyrmions [95]. Presently, a device for 3-dimensional polarization analysis, MuPAD, is being installed at the new diffractometer MIRA at FRM-II and will help in combination with extensive torque measurements to resolve the microscopic magnetic structure in the A-phase of MnSi and distinguish between the various models.

Chapter 7

Conclusions and Outlook

C' est tellement inutile que c' est rigoureusement indispensable.
Joe Simpson

In this thesis we investigated the critical spin fluctuations in localized and itinerant magnets by means of bulk methods and small-angle scattering with polarized neutrons. Using the inclined magnetic field geometry we studied the critical magnetic scattering from the Heisenberg ferromagnet EuS and it was possible to induced the chirality and thus determine the three-spin correlation functions. Two contributions to the critical scattering $I_{\sum}(q)$ and $\Delta I(q)$ were studied in the vicinity of $T_C = 16.5\,\mathrm{K}$. The symmetric contribution contribution, namely $I_{\sum}(q)$, comes from the pair correlation function. The scattering intensity is well described by Ornstein-Zernicke expression $I_{\sum} = A(q^2 + \kappa^2)^{-1}$ where κ represents the inverse correlation length of the critical fluctuations. κ obeys the scaling law $\kappa = \kappa_0 \tau^{\nu}$, where $\tau = (T - T_C)/T_C$ is the reduced temperature, $\kappa_0 = 5.88\,\mathrm{nm}^{-1}$, and $\nu = 0.68 \pm 0.01$.
The difference contribution $\Delta I(q)$ is caused by the three-spin correlation also called induced or dynamical chirality. It represents the asymmetric part of the polarization dependent scattering. $\Delta I(q)$ depends on the temperature as $\tau^{-\nu}$ with $\nu = 0.64 \pm 0.05$. The exponents ν as determined by means of static measurements (pair correlation function) and by dynamic measurements (induced chirality) are in good agreement with each other. Critical fluctuations near T_C are strongly influenced by the magnetic field.
The correlation length is suppressed by the field as $\xi(B) = a_0(gB\mu_B/T_C)^{1/z}$ with z the dynamical critical exponent $z = 2.1 \pm 0.1$, which is close to the value obtained by inelastic measurements using triple axis spectroscopy. Therefore we demonstrated that the inclined SANS geometry is a new approach for determining critical exponents. The dynamical chirality applied successfully to explore the model system EuS may contribute to investigate the critical behaviour of other magnetic systems where many spin correlations are important.
Furthermore the intrinsic chirality in itinerant weak ferromagnet MnSi has been studied by bulk methods and by small angle polarized neutron scattering. The specific heat at zero field shows an anomalous behavior around the critical temperature T_c. The scattering pattern at low temperatures shows four diffraction peaks along the $\langle 111 \rangle$ and $\langle \bar{1}\bar{1}1 \rangle$ cystallographic directions. These peaks are characteristic for the helical structure. Due to the lack of a center of symmetry, the magnetic moments are arranged along a left handed

spiral due to the Dzyaloshinskii-Moriya interaction. The experiments show that the incommensurate magnetic peaks evolve with increasing temperature into diffuse scattering that is mainly concentrated in a ring with a radius $q_c = 0.39\,\mathrm{nm}^{-1}$ centered at the position of the direct beam $q = 0$. The scattering is fully polarized for $\vec{q} \parallel \vec{P}_0$ and depolarized for $\vec{q} \perp \vec{P}_0$ proving the chiral nature of the scattering and the single handedness of the spiral. We determined the critical exponents of the magnetization, the susceptibility and the correlation lengths of the chiral fluctuations. The exponent $\beta_c = 0.44(1)$ of the magnetization is close to the value predicted for a chiral universality class. We compared bulk measurement with polarized neutron scattering data and found an indication of two transitions in MnSi. More experiments are needed to confirm this observation.
In the presence of a magnetic field we have determined the boundary of the magnetic A-phase of MnSi from distinct changes of slope in the AC-susceptibility for magnetic field B applied parallel to the crystallographic $\langle 100\rangle$, $\langle 110\rangle$ and $\langle 111\rangle$ directions. The specific heat displays an anomaly of a few $\%$ at the border of the A-phase characteristic of a well-defined phase transition. In addition to the previously reported change of orientation of the helical modulation in the A-phase, we observed a gradual appearance of a ring of neutron small-angle scattering intensity. These results may indicate the appearance of a new form of magnetic ordering that may be interpreted in terms of skyrmions. More theoretical and experimental studies are demanded to resolve the microscopic nature of the reorientation transition in MnSi. Presently a new device for 3-dimensional polarization analysis, MuPAD, is being installed at the diffractometer MIRA and will help in combination with torque magnetization measurements to resolve the microscopic magnetic structure in the A-phase of MnSi and distinguish between various models.

Bibliography

[1] T. Moriya. *Phys. Rev.*, 120:91, 1960.

[2] H.B. Braun, J. Kulda, B. Roessli, D. Visser, K.W. Krämer, H. Güdel, and P. Böni. *Nature Phys.*, 1:159–163, 2005.

[3] H.E. Stanley. Clarendon Press, Oxford, 1971.

[4] L.D. Landau and E.M. Lifshits. Pergamon Press, London, 1958.

[5] M.F. Collins. Oxford University Press, 1989.

[6] E. Brezin, J.C. Le Guillou, and J. Zinn-Justin. *Phys. Letters*, 47A:95, 1974.

[7] E. Frey and F. Schwabl. *Adv. Phys.*, 43:577, 1994.

[8] B.I. Halperin, P.C. Hohenberg, and S. Ma. *Phys. Rev. B*, 13:4119, 1976.

[9] H. Kawamura. *J. Appl. Phys.*, 63:3086, 1988.

[10] P. Azaria, B. Delamotte, and T. Jolicoeur. *J. Appl. Phys.*, 69:8, 1991.

[11] V.P. Plakhty, S.V. Maleyev, J. Wosnitza, B.K. Kremer, D. Visser, J. Kulda, O.P. Smirnov, A.G. Goukassov, I.A. Zobkalo, and E. Moskvin. *Physica B*, 267-268:259–262, 1999.

[12] T. Kato, K. Lio, T. Hoshino, T. Mitsui, and H. Tanaka. *J. Phys.Soc. Jpn.*, 61:275, 1992.

[13] B.D. Gaulin, M. Hagen, and H.R. Child. *J. Phys.C*, 8:327, 1988.

[14] H. Kawamura. *J. Phys. Soc. Jpn.*, 61:1299, 1992.

[15] V.P. Plakhty et al. *Phys. Rev. B*, 64:100402, 2001.

[16] T. Moriya. Springer, Berlin, 1985.

[17] L.P. Kadanoff. *Phys. Rev. Lett.*, 23:1430, 1969.

[18] M.E. Fischer. *Phys. Rev.*, 180:594, 1969.

[19] E.C. Stoner. *Proc. R. Soc.*, A 165:372, 1938.

[20] Y. Ishikawa and N. Miura. Springer Verlag, 1991.

[21] T. Moriya. *Solid State Commun.*, 20:291, 1976.

[22] K. Makoshi and T. Moriya. *J. Phys. Soc. Jpn.*, 44:80, 1978.

[23] O. Nakanishi, A. Yanase, A. Hsegawa, and M. Kataoka. *Solid State Commun.*, 35:995, 1980.

[24] P. Bak and M.H. Jensen. *J. Phys. C*, 13:L881, 1980.

[25] M.L. Plumer and M.B. Walker. *J. Phys. C: Solid State Phys.*, 14:4689 – 4699, 1981.

[26] B. Lebech, P. Harris, J.S. Pedersen, K. Mortensen, C.I. Gregory, N.R. Bernhoeft, M. Jermy, and S.A. Brown. *J. Magn. Magn. Mat.*, 140-144:119, 1995.

[27] M. Kataoka and O. Nakanishi. *J. Phys. Soc. Jpn.*, 50:3888–3896, 1981.

[28] M.B. Walker. *Phys. Rev. B*, 40:9315, 1989.

[29] S.V. Maleyev. *Usp. Fiz. Nauk*, 172:617, 2002.

[30] S.V. Grigoriev, S.V. Maleyev, A.I. Okorokov, Yu.O. Chetverikov, R. Georgii, P. Böni, D. Lamago, H. Eckerlebe, and K. Pranzas. *Phys. Rev. B*, 72:134420, 2005.

[31] S.V. Maleyev. *Physica B*, 345:119, 2004.

[32] B. Lebech. *Recent Advances in Magnetism of Transition Metal Compounds*, chapter 167. World Scientific, Singapore, 1993.

[33] G. Shirane, R. Cowley, C. Majkrzak, J.B. Sokoloff, P. Pagonis, C.H. Perry, and Y. Ishikawa. *Phys. Rev. B*, 28:6251, 1983.

[34] Brochure for Physical Property Measurement System. Technical report, Quantum Design, www.qdusa.com, 2003.

[35] J.S. Hwang, K.J. Lin, and Cheng Tien. *Rev. Sci. Instrum.*, 68:94, 1997.

[36] G.L. Squires. Dover Publications, Inc, Meneola, New York, 1997.

[37] R. M. White. Advanced Physics, McGraw-Hill Book Company, 1970.

[38] S.W. Lovesey. Clarendon Press Oxford, 1984.

[39] M. Blume. *Phys. Rev.*, 130:1670, 1963.

[40] S.V. Maleyev. *Physica B*, 297:67, 2001.

[41] S.V. Maleyev. *Phys. Rev. Lett.*, 75:4682, 1995.

[42] S.A. Brazovskii. *Sov. Phys. JETP*, 41:85, 1975.

[43] W. Schmatz, T. Springer, and J. Schelten. *J. Appl. Cryst.*, 7:96, 1974.

[44] A.I. Okorokov, V.V. Runov, B.P. Toperverg, A.D. Tretyakov, E.I. Latsev, I.M. Puzeii, and V.E. Mikhailova. *JETP Lett.*, 43:503, 1986.

[45] A.I. Okorokov. *Physica B*, 226-228:204, 2000.

[46] A.V. Lazuta, S.V. Maleyev, and B.P. Toperverg. *Sov. Phys. JETP*, 54:782, 1981.

[47] S.V. Maleyev. *Soc. Sci. Rev. A. Phys.*, 8:323–445, 1987.

[48] A.M. Polyakov. *Sov. Phys. JETP*, 30:151, 1970.

[49] J.A. Cuesta, Y. Martinez-Raton, and P. Tarazona. *J. Phys.: Condens. Matter*, 14:11965, 2002.

[50] B. Bildstein and G. Kahl. *Phys. Rev. E*, 47:1712, 1993.

[51] FRM-2 official webpages, http://www.frm2.tum.de/mira/index.shtml.

[52] G. Groll. *Z. Phys.*, 243:60, 1971.

[53] P. Böni, D. Görlitz, J. Kötzler, and J.L. Martinez. *Phys. Rev. B*, 43:8755, 1991.

[54] A.I. Okorokov, A.G. Gukasov, V.N. Slusar, B.P. Toperverg, O. Schärpf, and F. Fuzhura. *JETP Lett.*, 37:319, 1983.

[55] P. Böni, B. Roessli, D. Görlitz, and J. Kötzler. *Phys. Rev. B*, 65:144434, 2002.

[56] J.W. Cable and W.C. Koehler. *J. Magn. Magn. Mater.*, 5:258, 1982.

[57] J. Kötzler, G. Kamleiter, and G. Weber. *J. Phys. C*, 9:L361, 1976.

[58] J. Kötzler. *Phys. Rev. Lett.*, 51:833, 1983.

[59] P. Böni, G. Shirane, H.G. Bohn, and W. Zinn. *J. Appl. Phys.*, 63:3089, 1988.

[60] E. Frey and F. Schwabl. *Z. Phys. B: Conden. Matter*, 71:355, 1988.

[61] D. Görlitz and J. Kötzler. *Eur. Phys. J. B*, 5:37, 1998.

[62] M.A. Fischer and A. Aharony. *Phys. Rev. Lett.*, 30:559, 1973.

[63] J. Kötzler, F. Mezei, D. Görlitz, and B. Farago. *Europhys. Lett.*, 1:675, 1986.

[64] P. Böni. Private communication.

[65] G. Mazenko. *Phys. Rev. B*, 14:3933, 1976.

[66] B.I. Halperin and P.C. Hohenberg. *Phys. Rev.*, 177:952, 1969.

[67] P.C. Hohenberg and B.I. Halperin. *Rev. Mod. Phys.*, 49:435, 1977.

[68] F. Mezei. *Phys. Rev. Lett.*, 49:1096, 1982.

[69] J. Als-Nielsen, O.W. Dietrich, and L. Passel. *Phys. Rev. B*, 14:4908, 1976.

[70] Y. Ishikawa, K. Tajima, P. Bloch, and M. Roth. *Solid State Commun.*, 19:525, 1976.

[71] B. Roessli, P. Böni, W.E. Fischer, and Y. Endoh. *Phys. Rev. Lett.*, 88:237204, 2002.

[72] C. Pfleiderer, S.R. Julian, and G.G. Lonzarich. *Nature*, 414:427, 2001.

[73] C. Pfleiderer, D. Reznik, L. Pintschovius, H. von Löhneysen, M. Garst, and A. Rosch. *Nature*, 427:227, 2004.

[74] L.M. Sandratskii. *Adv. Phys.*, 47:91, 1998.

[75] Y. Ishikawa, G. Shirane, J.A. Tarvin, and M. Kohgi. *Phys. Rev. B*, 16(11):4956, 1977.

[76] N. Doiron-Leyraud, I.R. Walker, L. Taillefer, M.J. Steiner, S.R. Julian, and G.G. Lonzarich. *Nature*, 425:595–599, 2003.

[77] C. Thessieu, J. Flouquet, G. Lapertot, A.N. Stepanov, and D. Jaccard. *Solid State Commun.*, 95:707, 1995.

[78] K. Kadowaki, K. Okuda, and M. Date. *J. Phys. Soc. Jpn.*, 51:2433, 1982.

[79] Y. Ishikawa and M. Arai. *J. Phys. Soc. Jpn.*, 53:2726, 1984.

[80] C. Pfleiderer, G.J. McMullan, S.R. Julian, and G.G. Lonzarich. *Phys. Rev. B*, 55:8330, 1997.

[81] C. Pfleiderer. *J. Phys.: Condens. Matter*, 17:987–997, 2005.

[82] D. Bloch, J. Voiron, V. Jaccarino, and J.H. Wernick. *Phys. Lett.*, 51A:259, 1975.

[83] C. Pfleiderer, G.J. McMullan, and G.C. Lonzarich. *Physica B*, 199:634, 1995.

[84] S. Sachdev. *Rev. Mod. Phys.*, 75:913, 2003.

[85] V. Barzykin and L.P. Gorkov. *Phys. Rev. Lett.*, 70:2479, 1993.

[86] GKSS Forschungszentrum in Geesthacht, http://genf.gkss.de.

[87] Institut Laue-Langevin in Grenoble, http://www.ill.fr/lss/grasp.

[88] C. Gregory, D.B. Lambrick, and N.R. Bernhoeft. *J. Magn. Magn. Mat.*, 104-107:689, 1992.

[89] T.E. Mason, B.D. Gaulin, and M.F. Collins. *Phys. Rev. B*, 39:586, 1989.

[90] V.P. Plakhty, J. Kulda, D. Visser, E.V. Moskvin, and J. Wosnitza. *Phys. Rev. Lett.*, 85:3942, 2000.

[91] G.G. Lonzarich and L. Taillefer. *J. Phys. C: Solid State Phys.*, 18:4339–4371, 1985.

[92] C. Thessieu, C. Pfleiderer, A.N. Stepanov, and J. Flouquet. *J. Phys.: Condens. Matter*, 9:6677, 1997.

[93] S.V. Maleyev. *private communication*.

[94] A.I. Okorokov, S.V. Grigoriev, Yu. O. Chetverikov, S.V. Maleyev, R. Georgii, P. Böni, D. Lamago, H. Eckerlebe, and K. Pranzas. *Physica B*, 356:259, 2005.

[95] U. Rössler, A.N. Bogdanov, and C. Pfleiderer. *Physica B*, 359-361:1162, 2005.

Appendix A

List of Abbreviations and Symbols

SANS	Small Angle Neutron Scattering	$F(q)$	Magnetic form factor
TAS	Triple Axis Spectrometer	P_0	The initial polarization
PSD	Position Sensitive Detector	P_S	Parametrised polarization
RRR	Residual Resistivity Ratio	$S(Q,\omega)$	Scattering function
DM	Dzyaloshinskii-Moriya interaction	C	Specific heat
RPA	Random Phase Approximation	E_F	Fermi energy
SCR	Self Consistent Renormalization	$\hat{V}$	Scattering potential
C	Specific heat	μ_S	Spontaneous moment
S	Entropie	μ_{eff}	Effective magnetic moment
$\vec{q}$	Scattering vector	a	Lattice constant
$\vec{k_i}$	Incident wave vector	I_m	Pure magnetic scattering
$\vec{k_f}$	Scattered wave vector	Z_m	Amplitude of spin fluctuations
J	Exchange interaction term	$\vec{B}$	Magnetic field
θ	Scattering angle	B_C	Critical magnetic field
θ_x	Scattering angle in x-direction	$\vec{A}$	Vector potential
θ_y	Scattering angle in y-direction	M	Magnetization
$k = 2\pi/d$	Length of the spiral in reciprocal space	μ_B	Bohr magneton
d	Length of the spiral in real space	τ	Reduced temperature
q_d	Dipolar wave number	$\chi(q,\omega)$	Dynamic susceptibility
Q	Momentum transfer	χ_{AC}	AC susceptibility
D	Stiffness constant	F	Free energy
κ	Inverse correlation length	W	Free energy density
ξ	Correlation length	$\hat{q}$	Cubic invariant
$G(q)$	Correlation function	$A, \tilde{D}$	Anisotropy coefficients
A_m	Weak anisotropic interaction term	T_C	Curie temperature
D_m	Isotropic DM interaction term	T_c	Critical temperature

Appendix B

List of Publications

D. Lamago, M. Dameris, C. Schnadt, V. Eyring and C. Brhl: *Impact of large solar zenith angles on lower stratospheric dynamical and chemical processes in a coupled chemistry-climate model*, Atmos. Chem. Phys.,3 1981-1990 (2003).

R. Georgii, P. Böni, **D. Lamago**, S. Stüber, S.V. Grigoriev, S.V. Maleyev, H. Eckerlebe, P.K. Pranzas, B. Roessli and W.E. Fischer: *Critical Small-angle Scattering of Polarised Neutrons in MnSi*, Physica B 350: 45-47 (2004).

D. Lamago, R. Georgii, P. Böni: *Magnetic susceptibility and specific heat of the itinerant ferromagnet MnSi*, Physica B 359, 1171-1173 (2005).

I. Okorokov, S.V. Grigoriev, Yu.O. Chetverikov, S.V. Maleyev, R. Georgii, P. Böni, **D. Lamago**, H. Eckerlebe, K. Pranzas: *The Effect of the magnetic field on the spiral spin structure in MnSi studied by polarized SANS*, Physica B 356, 256-263 (2005).

S.V. Grigoriev, S.V. Maleyev, A.I. Okorokov, Yu.O. Chetverikov, R. Georgii, P. Böni, **D. Lamago**, H. Eckerlebe and K. Pranzas: *Critical fluctuations in MnSi near T_C: A polarized neutron scattering study*, Phys. Rev. B 72, 72:134420 (2005).

S.V. Grigoriev, S.V. Metelev, S.V. Maleyev, A.I. Okorokov, P. Böni, R. Georgii, **D. Lamago**, H. Eckerlebe and K. Pranzas: *Critical two- and three-spin correlations in EuS: An investigation with polarized neutrons*, Phys. Rev. B 72, 72:214423 (2005).

D. Lamago, R. Georgii, C. Pfleiderer, P. Böni: *Magnetic-field induced instability in the A-phase of MnSi: Bulk ans SANS measurements*, Physica B in press (2006).

D. Lamago, R. Georgii, C. Pfleiderer, P. Böni: *Field dependence of the magnetic structure of the itinerant magnet MnSi*, Phys. Rev. B to be submitted.

List of Figures

Acknowledgments

It is a great pleasure for me to express my sincere gratitude to Prof. Dr. Peter Böni, who supervised this work with discretion. During the last three years, I have been nourished with his broad knowledge of neutron scattering, inspired by his brilliant insights, and guided by his scientific rigorousness. At the same time, he endowed me with maximal freedom for developing my ideas. I am also indebted to him for the helps with various non-scientific matters, to which he has never been indifferent. Above all, I enjoyed a lot working with him.

I would like to thank Prof. Dr. Peter Böni and Prof. Christian Pfleiderer, for their careful reading of the manuscript.
I would like to thank to Prof. Christian Pfleiderer who had great interest in my work, for many fruitful discussions and personal involvement during the last year of my thesis. He teached me also scientific rigorousness and always stimulated and encouraged me for this research work. I am also indebted to him for the helps with various non-scientific matters. Many thanks to Dr. Robert Georgii for helping, assisting and counseling me as well in scientific as in daily life. It was a pleasure to work with him.

It is a pleasure to acknowledge the successful collaboration with my Russian colleagues Prof. Alexei Okorokov, Dr. Sergey Grigoriev, Yuri Chetverikov and Dr. Sergey Metelev for numerous scientific discussions during the last three years. We spend nice hours together during the experiments.

I am deeply grateful to emeritus Prof. Dr. Wolfgang Gläser and Prof. Dr. Winfried Petry at the Neutron Source FRM-II in Garching, who initiated me in the field of science with neutrons.
I thank Prof. Dr. Winfried Petry for his continuous encouragement and the opportunity to be involved in the FRM-2 scientific staff.

I would like to thank all colleagues in the Institute E21 of the Physics Department at the Technical University of Munich. Many thanks to Dr. Evgeny Klementiev and Dr. Shah Valloppilly for numerous discussions on both scientific and non-scientific matters and the friendly helps with various problems.
I thank to Dipl. Phys. Nicolas Arend at E21 and Charles Dewhurst at the Institue Laue

Langevin in Grenoble for their support with computer related matters and data reduction tools.

I am grateful to the colleagues at the Neutron facility in Geesthacht for their hospitality and the supports during the experiments. In particular, many thanks to Dipl. Phys. Helmut Eckerlebe and Dr. Klaus Pranzas.

The assistance of Dr. Werner Bieberacher during the magnetic torque measurements at the Walter-Meissner-Institute in Garching is kind fully acknowledged.

I thank my parents Marguerite Ningdoung and Etienne Kaffo who taught me how to read and write. I really appreciated what they did for me.

This work could not have been completed in such a peaceful way without encouragements of many friends whom I came to know in Europe. In particular, I am deeply indebted to those who sincerely shared with me authentic fellowship and brotherhood of Christian faith in Munich, Aachen and Braunschweig. In particular, many thanks to Dipl.-Ing. Ferdinand Georg for his faithful friendship.

Prayers and supports of my wife, H*é*l*è*ne, are cordially acknowledged. Many thanks for the joyful times we spent together for her prudence she showed whenever hard times of life needed to be encountered.

Finally, I dedicate this thesis to my lovely children Shirel Hodiya and Laurick Moriel, whose love is more than I can describe.

February 28, 2006, Munich *"By the grace of God, I am what I am...." (1Cor 15:10)*